Heavy Flavor Production in Z^0 Decays

by

Tie-Sheng Dai

B.S. (Physics), University of Science and Technology of China

(1986)

Submitted to the Department of Physics
in partial fulfillment of the requirements for the degree of

Doctor of Philosophy

at the

MASSACHUSETTS INSTITUTE OF TECHNOLOGY

November, 1991

Author Tieshang Dai
Department of Physics
November 12, 1991

Certified by Gregor Herten
Gregor Herten
Associate Professor
Thesis Supervisor

Accepted by L. F. Koster
George F. Koster
Chairman, Departmental Committee on Graduate Students
Department of Physics

Heavy Flavor Production in Z^0 Decays

by

Tie-Sheng Dai

Submitted to the Department of Physics
on November 12, 1991, in partial fulfillment of the
requirements for the degree of
Doctor of Philosophy

Abstract

In this thesis, the heavy quark decay modes of the Z^0 particle are studied with inclusive muon and electron events taken by the L3 detector at LEP. The data sample corresponds to $\sim$ 130,000 hadron events at c.m.s energies around the Z^0 pole. The weighted average center-of-mass energy is 91.28 GeV. The data are found to be consistent with the universality of the quark couplings. From the ratio of the number of dilepton events to the number of single lepton events, the average b quark semileptonic branching ratio has been found to be $Br(b \to l\nu X) = 0.111 \pm 0.010(stat) \pm 0.006(sys)$, without assumptions on $\Gamma_{b\bar{b}}$. The partial width of the Z^0 decay into $b\bar{b}$ pairs has been measured to be $\Gamma_{b\bar{b}} = 385 \pm 7(stat) \pm 15(sys)\ MeV$, with an additional 19 MeV error from the uncertainty in $Br(b \to l\nu X)$. By using inclusive muon data, the partial decay widths $\Gamma_{b\bar{b}}$ and $\Gamma_{c\bar{c}}$ have been determined simultaneously , $\Gamma_{b\bar{b}} = 396 \pm 10(stat) \pm 24(sys)$ and $\Gamma_{c\bar{c}} = 296 \pm 24(stat) \pm 36(sys)$. Assuming the Standard Model prediction of $\Gamma_{b\bar{b}} = 378 \pm 3\ MeV$, the average b quark semileptonic branching ratio (e and μ) and the average fractional energy carried by b hadrons from b quark have been determined to be $Br(b \to l\nu X) = 0.119 \pm 0.003(stat) \pm 0.006(sys)$, and $<x_E> = 0.686 \pm 0.006(stat) \pm 0.020(sys)$. From inclusive muon data, without assuming the b quark fragmentation function, the fitted x_E distribution is consistent with the Peterson *et al.* fragmentation function for b quarks. The CKM matrix element $|V_{cb}|$ has been determined to be $|V_{cb}| = 0.046 \pm 0.002\ ^{+0.004}_{-0.003}$ from the measured $Br(b \to l\nu X)$ combined with the L3 b hadron lifetime measurement.

The $b\bar{b}$ forward-backward asymmetry has been measured from the b quark angular distribution by fitting the inclusive lepton p and $p_\perp$ spectra, which gives the result $A_{b\bar{b}} = 0.127^{+0.042}_{-0.040}(stat) \pm 0.023(sys)$. This asymmetry corresponds to the value of the effective mixing angle $\sin^2\bar{\theta}_W = 0.226 \pm 0.008(stat) \pm 0.005(sys)$ at the Z^0 mass. The B^0-$\bar{B}^0$ oscillation has been observed and the measured value of the mixing parameter is $\chi_B = 0.178^{+0.049}_{-0.040}(stat) \pm 0.017(sys)$. This value is consistent with maximal mixing in the ${B_s}^0$-$\bar{B}^0_s$ system and gives $\chi_s > 0.13$, $\Delta M_s > 3.2 \times 10^{-4} eV$ at 90% CL.

Thesis Supervisor: Gregor Herten
Title: Associate Professor

Acknowledgments

My first thanks are given to my thesis advisor, Professor Gregor Herten, for his constant and patient support, for taking a personal interest in my work, for offering physics discussions, helpful suggestions and positive guidance, and for his caring in the last 4 years. Over this period, I learned a lot of physics and new ideas from him.

I thank Professor S.C.C. Ting for his support. Because of him, I have the opportunity to work at the L3 experiment in High Energy Physics. His clear view of physics, outstanding experimental ability and strong leadership led to the successful realization of the L3 experiment. I would like to express my highest respect for him.

I thank Professor U. Becker for his guidance and support. His deep understanding and broad knowledge of physics, and rich experience in the experiments resulted in the success of the L3 Muon Chamber.

I thank Dr. Masaki Fukushima for his patient guidance and kindness. From him I learned how to do a careful work on the electronic system. He played a central role in reconstruction of the L3 trigger and DAQ system. I have benefited greatly from the L3 trigger group as a graduate student. I thank all members of the L3 trigger and DAQ group and particularly Dr. T. Hebbeker, Dr. S.X. Wu, Dr. V. Koutsenko, Dr. J.J. Blaising, Dr. M. Capell, Dr. D. Linnhofer, Dr. A. Degre and C. Luci for their enjoyable and profitable collaboration.

It is my pleasure to work in the L3 group with so many experienced physicists. I wish to thank all the members of this outstanding group. I am indebted to Dr. B. Clare, I. Clare, Dr. V. Innocente and Dr. D. Stickland for their successful work and management of analysis software and data production. I have learned a lot from discussions with Prof. B. Wyslouch, Prof. J. Branson, Dr. J.F. Zhou, Dr. P. Mcbride, Dr. L. Salvatore, Prof. A. Böhm, Prof. H.F. Chen, Dr. G. Bobbink, Dr. H.S. Chen and Dr. F. Linde, and extend particular thanks to Prof. B. Wyslouch for his helpfulness and his readiness to answer questions. I would like to thank all the people in the heavy flavor analysis group for the fruitful collaboration and their help. Many thanks to Dr. J.M. Qian, Y.J. Pei, T. Foreman, J. Alcaraz, D.H. Zhang, K. Qureshi, M. Gruenewald, Dr. T. McMahon and M. Hebbert for their friendship and their work, which simplified a lot of things.

I thank the other members of my thesis committee, Prof. L.S. Osborne and Prof. L. Rosenson for reading and improving this thesis. Taking this opportunity, I thank N. Regnier for the comments about my English grammar.

I wish to thank Dr. F.J Eppling, Dr. S.M. Ting, and other members of MIT/LNS for their strong support of the L3 experiment. I also thank E. Bober, P. Harris, J. Hudson, R. Meisel, P. Slade, Dr. P. Lecomte, Dr. M. Steuer and the L3 A&C group for their effective administration. I would like to take this opportunity to thank J. Donahue, Dr. X. Wu and Prof. B. Zhou for their help during my first year at MIT.

I wish to thank CERN for its hospitality and help and to express my gratitude to the CERN accelerator divisions for the excellent performance of the LEP machine.

I appreciate the help and friendship of all my friends, which make life easier at

CERN and MIT. I would like to thank all the people who helped me during the last three years, without their help, life at CERN would have been more difficult. I want to take this chance to express my gratitude to my Chinese friends at CERN, Q. An, J.Z. Bao, X.D. Cai, Dr. Y.H. Chang, F. Dong, G.A. Hu, Q. Li, Y.B. Lui, D.N. Mao, X.L Shi, L.Z. Sun, Y.F. Wang and G.H. Wang etc. for their understanding, parties and Chinese food. I give my special thanks to Prof. Y.D. Zhang and Prof. H.F. Chen for their encouragement and my teachers at High School for inspiring my interest in physics. I thank Prof. H. Hofer for his support.

I thank my family and relatives for love, understanding, strong support and encouragement. Thanks to my mamma and papa for sending their son to study on another continent and to other members of my family who never lost their trust on me. This thesis would not have been done without their support along the way.

Table of Contents

List of Tables

Chapter 1

Introduction

The discovery of the intermediate vector bosons Z^0 and $W^{\pm}$ at CERN in 1983 by the CERN UA1 and UA2 experiments [1-1] was a remarkable achievement. It provided a confirmation of the key predictions of the electroweak theory, known as the "Standard Model". The electroweak theory, advanced by Glashow, Weinberg and Salam [1-2], unifies electromagnetic and weak interactions based on the symmetry group SU(2) × U(1) and spontaneous symmetry breaking through the Higgs mechanism [2-3]. It is the most comprehensive and consistent theory of the electroweak phenomena. LEP, which overcomes the problems of $p\bar{p}$ colliders (the large background and low Z^0 production rate) and provides an unbiased background-free data set of Z^0 produced via e^+e^- collisions, gives the unique ground for precision tests of theoretical predictions at the level of radiative corrections.

The Z^0 particle, one of the gauge bosons carrying the weak force, is one of the most important particles in the Standard Model. The Z^0 resonance provides an ideal environment for performing a stringent test of the Standard Model and searching for new phenomena with high statistics, due to the large cross section enhancement on resonance apparent in Figure 1-1. Also, a detailed investigation of the Z^0 particle and its decays can help to determine the parameters of the Standard Model. For example, the forward-backward charge asymmetry A_{FB} in $e^+e^- \rightarrow f^+f^-$ (where $f = \mu,\ \tau,\ q$) is one of the most important quantities since it is sensitive to the weak mixing angle and to the weak coupling constants. Precision measurements can give information about the top quark mass.

Many improvements in our understanding of the basic interaction of quarks and leptons can be obtained by a closer study of b quark physics. In the Standard Model the partial decay width $\Gamma_{q\bar{q}}$ in $Z^0 \rightarrow q\bar{q}$ depends on the weak isospin of the quark and is expected to be larger for down-type than for up-type quarks. For light quarks the predictions of $\Gamma_{q\bar{q}}$ have uncertainties of about 10 MeV because of the unknown mass of the top quark from 30 GeV to 250 GeV. This limits the accuracy of Standard Model tests in the light quark sector. In contrast, the partial width $\Gamma_{b\bar{b}}$ in $Z^0 \rightarrow b\bar{b}$ decays is expected to be insensitive to the top mass. Thus high statistics measurement of $\Gamma_{b\bar{b}}$ could be used to determine the weak neutral couplings of b quarks precisely, and to test the universality of the quark couplings. The electroweak mixing angle $\sin^2\theta_W$ which is one of the fundamental parameters

of the Standard Model can be precisely determined from the forward-backward asymmetry ($A_{b\bar{b}}$) of $b\bar{b}$ pairs. Knowledge of quark mixing angles can be obtained by measuring the semileptonic branching ratio and the lifetime of the b hadrons, and by studying flavor oscillation in the B^0-$\bar{B}^0$ system.

Even though the Standard Model has been tremendously successful so far, it leaves many fundamental problems unsolved. A detailed investigation of B physics gives a way to test the validity of the Standard Model. Certain processes, such as flavor oscillations in the neutral B system or rare decays of B mesons which are induced by loop diagrams, are sensitive to physics beyond the Standard Model with three generations. The CP violation, the strength of which could not be well explained by the Standard Model, was observed only in the K^0-$\bar{K}^0$ system. Clearly it is important to search for other systems in which the CP violation manifests itself and answers the question — "What is the origin of CP violation?". The B^0-$\bar{B}^0$ system is analogous to the K^0-$\bar{K}^0$ system, therefore the observation of B^0-$\bar{B}^0$ oscillation is an important experimental step towards the observation of the CP violation in a system other than the K^0-$\bar{K}^0$.

The fragmentation of quarks into hadrons can be deduced qualitatively from QCD, yet a detailed understanding is still lacking due to its complex nature. It is of both theoretical and experimental interest to study the fragmentation of heavy quark into hadrons and to explore the dynamical driving mechanism of jet formation. Because the production of heavy quarks is suppressed in the fragmentation process due to their large masses, heavy mesons carry either the primary quark or its decay product. Therefore heavy quarks are the best system to study the hadronization mechanism.

This work presents the measurement of the properties of the Z^0 decaying into heavy quark pairs through the semileptonic decay of heavy quarks. About 130,000 $e^+e^- \rightarrow hadrons$ events, recorded by the L3 detector at LEP in 1989 and 1990 are used in this study. The electroweak couplings of heavy quarks have been measured. The partial decay width ($\Gamma_{b\bar{b}}$ and $\Gamma_{c\bar{c}}$) and forward-backward charge asymmetry ($A_{b\bar{b}}$ of heavy quarks have been determined. From the measurement, the effective mixing angle $\sin^2\theta_W$ has been obtained. The average b quark semileptonic branching ratio $Br(b \rightarrow l\nu X)$ has been measured from the rate of inclusive lepton events and the ratio of the number of dilepton events to the number of single lepton events, separately. $Br(b \rightarrow l\nu X)$ from the double tagging method is independent of assumption of $\Gamma_{b\bar{b}}$. And combining the $Br(b \rightarrow l\nu X)$ measurement with the b hadron lifetime, the CKM matrix element V_{cb} has been determined. The average fractional energy of bottom quarks in $Z^0 \rightarrow b\bar{b}$ events has been obtained. Finally, the flavor oscillation in the B^0-$\bar{B}^0$ system has been measured.

Chapter 2

Theory

The production of Z^0s in e^+e^- annihilation and their subsequent decay into fermion pairs can be precisely calculated in the Standard Model. The photon radiation of fermions is rather well known through QED (Quantum Electrodynamics) [2-1], and the gluon radiation of quarks can be calculated by QCD (Quantum Chromodynamics) [2-2]. The hadrons which are observed in the detector come from the fragmentation of quarks. In this chapter, a brief description of the theory about the heavy flavor production, decay, forward-backward asymmetry, B^0-$\bar{B}^0$ system oscillation and quark fragmentation is presented.

2.1 Basic Concepts

The SU(2) $\times$ U(1) electroweak model is a gauge field theory, which has three types of elementary building blocks of matter.

- Fundamental fermions (quarks and leptons): Leptons and quarks are treated as pointlike particles which couple to the gauge bosons of SU(2) through their weak charge and to the photon of U(1) through their electric charge. Quarks also carry a color charge and there are three color states for each quark.
- The force carriers, i.e. four gauge bosons (γ, Z^0, $W^{\pm}$): Through the Higgs mechanism [2-3] three of these bosons become massive, and correspond to the mediators of the weak interaction. The fourth remains massless and corresponds to the photon, the mediator of electromagnetic interaction.
- The Higgs boson: The Higgs field is believed to be responsible for the masses of all the particles through the spontaneous symmetry breaking. The Higgs boson has not been found yet.

The left-handed fermions are assumed to transform as doublets under the weak isospin group (weak isospin 1/2) and the right-handed ones as singlets (weak isospin 0). So far, there is no evidence for the existence of right-handed neutrinos. There are only three fermion families with a neutrino mass below Z^0 mass as measured by LEP and SLC experiments [2-4], Table 2.1 lists the properties of three fermion

generations, where N_c is the number of colors. Each family consists of two quarks and two leptons. The first family contains the up and down quark, the electron and electron neutrino. The second family is made up of the charm and strange quark, the muon and muon neutrino. The third family is occupied by the top and bottom quark, tau and tau neutrino. The leptons carry integral electric charge, 0 or ± 1 $|e|$, and the quarks carry fractional electric charges. The top quark and τ neutrino of third family have not been experimentally observed yet.

Family	Flavor	Spin	Charge ($\|e\|$)	N_c	Mass (MeV)
1	u	1/2	2/3	3	$\simeq 350$
	d	1/2	$-1/3$	3	$\simeq 350$
	e	1/2	-1	1	0.511
	ν_e	1/2	0	1	$\simeq 0$
2	c	1/2	2/3	3	$\simeq 1800$
	s	1/2	$-1/3$	3	$\simeq 550$
	μ	1/2	-1	1	105.6
	ν_μ	1/2	0	1	$\simeq 0$
3	t	1/2	2/3	3	
	b	1/2	$-1/3$	3	$\simeq 4950$
	τ	1/2	-1	1	1870
	ν_τ	1/2	0	1	$\simeq 0$

Table 2.1: *The fermions and their properties*

There are three massive vector bosons Z^0 and $W^\pm$, which mediate the weak interaction. And nine massless vector bosons (the photon and eight gluons) are responsible for the electromagnetic and strong interactions, respectively. Table 2.2 shows these particles.

The interactions of the SU(2) × U(1) gauge field are specified by the electroweak theory and are determined by the electric charge (e), and the mixing angle $\sin^2\theta_W$. The coupling constants for the vector and axial vector currents are summarized as following:

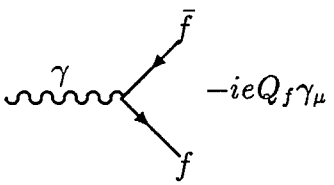

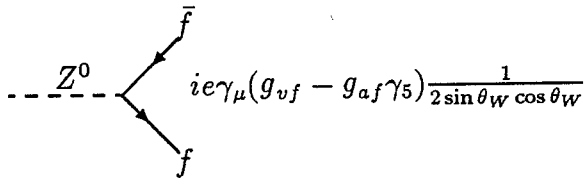

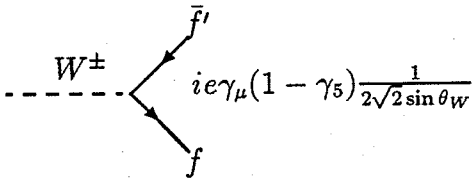

$$g_{af} = I_{3f} \qquad g_{vf} = I_{3f} - 2Q_f \sin^2\theta_W \tag{2.1}$$

where the f refers to the particular fermion, Q_f is the fermion charge, and I_{3f} is the third component of fermion weak isospin. The mixing angle $\sin^2\theta_W$ is given by the Z^0 and $W^\pm$ masses:

$$\sin^2\theta_W = 1 - \frac{M_W^2}{M_Z^2} \tag{2.2}$$

	Spin	Charge	Color	Mass (GeV)
γ	1	0	no	0
Z^0	1	0	no	91.181
$W^\pm$	1	± 1	no	$\simeq 80.6$
g_i $(i = 1, ..., 8)$	1	0	yes	0

Table 2.2: *The properties of interaction carriers, where the Z^0 mass is taken from the L3 measurement*

For pointlike spin-1/2 fermions in the center of mass frame, the differential cross section for $e^+e^- \to Z^0/\gamma \to f^+f^-$ can be written in the following way [2-5], where the color factor $N_{cf} = 1$ for leptons, $N_{cf} = 3$ for quarks:

$$\begin{aligned}
\frac{d\sigma}{d\Omega} &= \frac{\alpha^2}{4s}\beta N_{cf}\{Q_f^2[1+\cos^2\theta+(1-\beta^2)\sin^2\theta] \\
&- 4Q_f\chi 1\{g_{vf}V[1+\cos^2\theta+(1-\beta^2)\sin^2\theta] - 2g_{af}\beta\cos\theta\} \\
&+ 4\chi 2[g_{vf}^2(1+V^2)[1+\cos^2\theta+(1-\beta^2)\sin^2\theta] \\
&+ \beta^2 g_{af}^2(1+V^2)(1+\cos^2\theta) - 8\beta g_{vf}g_{af}V\cos\theta]\}
\end{aligned} \tag{2.3}$$

where

$$\begin{aligned}
\chi 1 &= \frac{1}{16\sin^2\theta_W\cos^2\theta_W}\cdot\frac{s(s-M_Z^2)}{(s-M_Z^2)^2+\Gamma_Z^2M_Z^2} \\
\chi 2 &= \frac{1}{256\sin^4\theta_W\cos^4\theta_W}\cdot\frac{s^2}{(s-M_Z^2)^2+\Gamma_Z^2M_Z^2} \\
V &= -1+4\sin^2\theta_W
\end{aligned} \tag{2.4}$$

Only the Z^0 and photon exchange diagrams of e^+e^- annihilation at lowest order are involved in these expressions. The Higgs exchange is negligible because of the small Yukawa coupling to the electrons.

2.2 Heavy Flavor Production

The improved Born approximation, which includes the final state fermion mass effect, the vacuum polarization and vertex corrections (see figure 2-1), gives the

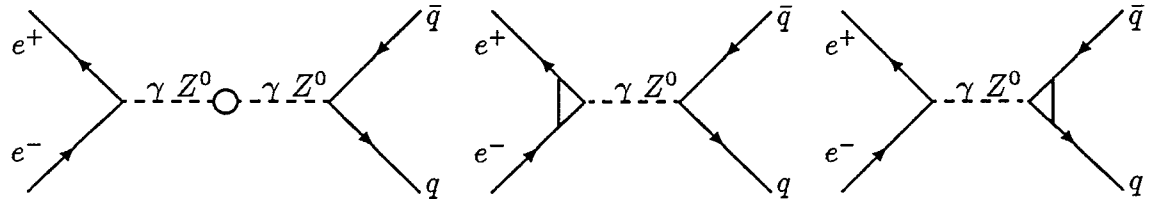

Figure 2-1: *The electroweak vacuum pol. and vertex corrections*

cross section [2-5] [2-6] of the heavy flavor as follows:

$$\sigma = \beta\frac{3-\beta^2}{2}\sigma^{VV} + \beta^3\sigma^{AA} = \sigma_B^V + \sigma_B^A \tag{2.5}$$

with

$$\begin{aligned}
\sigma^{VV} &= \frac{4\pi\alpha^2(M_Z^2)Q_q^2}{s} - \frac{4G_\mu\alpha(M_Z^2)}{\sqrt{2}}Q_q\bar{g}_{ve}\bar{g}_{vq}\frac{M_Z^2(s-M_Z^2)}{(s-M_Z^2)^2+(\frac{s}{M_Z}\Gamma_Z)^2} \\
&+ \frac{G_\mu^2}{2\pi}(\bar{g}_{ve}^2+\bar{g}_{ae}^2)\bar{g}_{vq}^2\frac{M_Z^4 s}{(s-M_Z^2)^2+(\frac{s}{M_Z}\Gamma_Z)^2} \\
\sigma^{AA} &= \frac{G_\mu^2}{2\pi}(\bar{g}_{ve}^2+\bar{g}_{ae}^2)\bar{g}_{aq}^2\frac{M_Z^4 s}{(s-M_Z^2)^2+(\frac{s}{M_Z}\Gamma_Z)^2}
\end{aligned} \tag{2.6}$$

and G_μ is muon decay constant. $\alpha(M_Z^2) \approx 1/128$ is the running QED coupling constant, which changes mainly due to the photon vacuum polarization. Effective electroweak vector, axial-vector couplings ($\bar{g}_{vf}$, $\bar{g}_{af}$) and effective mixing angle $\sin^2\bar{\theta}_{Wf}$ are expressed as:

$$\bar{g}_{af} = \sqrt{\rho_f}I_{3f} \qquad \bar{g}_{vf} = \sqrt{\rho_f}(I_{3f} - 2Q_f\sin^2\bar{\theta}_{Wf}) \tag{2.7}$$

$$\begin{aligned}
\sin^2\bar{\theta}_{Wf} &= (\sin^2\theta_W + \cos^2\theta_W\Delta\rho)(1+\frac{2}{3}\Delta\rho\,\delta_{fb}) \\
\rho_f &= \frac{1}{1-\Delta\rho}(1-\frac{4}{3}\Delta\rho\,\delta_{fb}) \\
\Delta\rho &= \frac{3\sqrt{2}G_\mu M_t^2}{16\pi^2}
\end{aligned} \tag{2.8}$$

ρ_f is the neutral current strength parameter and is defined as the ratio of the neutral current constant to the charged current constant. The parameter δ_{fb} is equal 1 for b quarks, and 0 otherwise. The extra factor in $\sin^2\bar{\theta}_{Wf}$ and ρ_f for b quarks results from the vertex diagrams in Figure 2-2 involving the heavy top quarks.

The QED corrections, which include initial and final state real/virtual photon radiations, are very important. The initial state photon emission reduces the peak cross section by $\sim$ 30%. The final state photon emission changes the cross section by a factor $1+\frac{3\alpha Q_f^2}{4\pi}$, and is small. The interference of virtual photon radiation contribution to the cross section is negligible.

The box diagrams in which the initial and final state fermions are linked by two massive gauge bosons (WW/ZZ) has negligible contribution to the cross section. Around the Z^0 pole, their influence is below $\mathcal{O}(10^{-4})$.

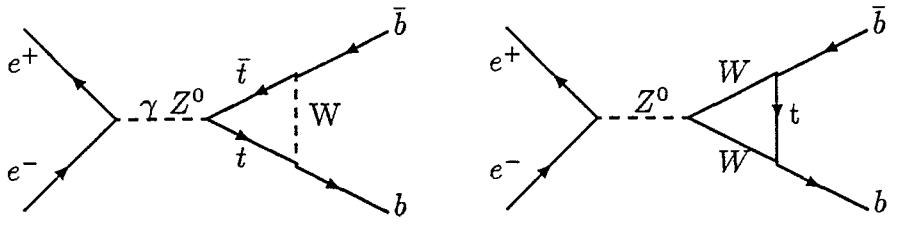

Figure 2-2: *Vertex Feynman diagrams involving top quarks*

Finally, the gluon radiation (QCD corrections) can be estimated to the order α_s^3 [2-6] in the limit $M_q = 0$. Approximately, it modifies the cross section by a multiplicative factor $[1 + c_1(\frac{\alpha_s}{\pi}) + c_2(\frac{\alpha_s}{\pi})^2 + c_3(\frac{\alpha_s}{\pi})^3]$, the coefficients c_i for the axial-vector and vector couplings are different. The differences arise because the masses break chiral invariance and because of the large mass splitting between bottom and top quarks. The coefficients are tabulated in Table 2.3, where $\mu^2 = 4M_q^2/s$. The $f(M_t)$ in Table 2.3 is well parametrized [2-7] [2-6] and $\pm$ for down/up quark. The calculation of the coefficient c_3 can be found in [2-8].

Coupling	c_1	c_2	c_3
vector	$1 + 3\mu^2$	1.41	12.8
axial-vector	$1 + 3\mu^2 \ln(4/\mu^2)$	$1.41 \pm f(M_t)$	12.8

Table 2.3: *The QCD correction coefficients*

The partial width of Z^0 decay to heavy quark pairs, obtained from the improved Born approximation including final state fermion mass effects is:

$$\Gamma_{qq} = \beta\frac{3-\beta^2}{2}\Gamma_{qq}^V + \beta^3\Gamma_{qq}^A = \Gamma_{Bqq}^V + \Gamma_{Bqq}^A \tag{2.9}$$

$$\Gamma_{qq}^V = \frac{G_\mu M_Z^3}{2\sqrt{2}\pi}\bar{g}_{vq}^2 \qquad \Gamma_{qq}^A = \frac{G_\mu M_Z^3}{2\sqrt{2}\pi}\bar{g}_{aq}^2 \tag{2.10}$$

The final state QED and QCD corrections are identical with those of the Z^0 cross section, where the initial photon radiation doesn't effect the Z^0 decay.

$$\begin{aligned} \Gamma_{qq}^V &\rightarrow \Gamma_{qq}^V(1+\delta_{QED})(1+\delta_{QCD}^V) \\ \Gamma_{qq}^A &\rightarrow \Gamma_{qq}^A(1+\delta_{QED})(1+\delta_{QCD}^A) \end{aligned} \tag{2.11}$$

with

$$\delta_{QED} = \frac{3\alpha Q_q^2}{4\pi} \qquad \delta_{QCD} = c_1(\frac{\alpha_s}{\pi}) + c_2(\frac{\alpha_s}{\pi})^2 + c_3(\frac{\alpha_s}{\pi})^3 \tag{2.12}$$

The QED correction is very small and the QCD correction is about 4% for $\alpha_s = 0.115$ [2-9]. From the ZFITER program [2-10], where the formulae given have the complete $\mathcal{O}((\alpha_s/\pi)^2)$ calculation within 1%, the electroweak theory predictions [1] of

[1]The Electroweak Theory predictions are obtained by using the parameters $\sin^2\theta_W = 0.224$, $M_Z = 91.181$ *GeV* [2-11], $M_t = 150$ *GeV*, $M_{Higgs} = 100$ *GeV and* $\alpha_s = 0.115$ unless otherwise specified.

the heavy flavor partial widths are:

$$\Gamma_{c\bar{c}} = 297\ MeV \qquad \Gamma_{b\bar{b}} = 378\ MeV \tag{2.13}$$

which correspond to 22 % *and* 15% of $Z^0 \rightarrow$ *hadrons* respectively.

2.3 Forward-Backward Asymmetry

For the full solid angle, the forward-backward asymmetry is defined as:

$$A_{FB} = \frac{\sigma_F - \sigma_B}{\sigma_F + \sigma_B} \tag{2.14}$$

$$\sigma_F = 2\pi \int_0^1 \frac{d\sigma}{d\Omega} d(\cos\theta) \qquad \sigma_B = 2\pi \int_{-1}^0 \frac{d\sigma}{d\Omega} d(\cos\theta) \tag{2.15}$$

where the θ is the opening angle between the quark and the electron direction. Using the improved Born approximation, the forward-backward asymmetry can be cast into the form:

$$A_{FB}(s) = \frac{3}{4} \cdot \frac{\beta^2 \sigma^{VA}(s)}{\sigma(s)} \tag{2.16}$$

with σ is the total cross section introduced earlier in equation 2.5, and:

$$\begin{aligned} \sigma^{VA}(s) = & - \frac{4G_\mu \alpha(M_Z^2)}{\sqrt{2}} Q_q \bar{g}_{ve} \bar{g}_{vq} \frac{M_Z^2(s - M_Z^2)}{(s - M_Z^2)^2 + (\frac{s}{M_Z}\Gamma_Z)^2} \\ & + \frac{2G_\mu^2}{\pi} \bar{g}_{ve} \bar{g}_{ae} \bar{g}_{vq} \bar{g}_{aq} \frac{M_Z^4 s}{(s - M_Z^2)^2 + (\frac{s}{M_Z}\Gamma_Z)^2} \end{aligned} \tag{2.17}$$

The energy dependent forward-backward asymmetries for c, b quarks are given in Figure 2-3. On the Z^0 pole ($s = M_Z^2$) the asymmetry is given by:

$$\begin{aligned} A_{qq} &= \frac{3}{4} \cdot \frac{2\bar{g}_{ve}\bar{g}_{ae}}{\bar{g}_{ve}^2 + \bar{g}_{ae}^2} \cdot \frac{2\bar{g}_{vq}\bar{g}_{aq}\beta}{\bar{g}_{vq}^2(3 - \beta^2)/2 + \bar{g}_{aq}^2\beta^2} \\ &\approx \frac{3}{4} \cdot \frac{2\bar{g}_{ve}\bar{g}_{ae}}{\bar{g}_{ve}^2 + \bar{g}_{ae}^2} \cdot \frac{2\bar{g}_{vq}\bar{g}_{aq}}{\bar{g}_{vq}^2 + \bar{g}_{aq}^2} \cdot (1 + \delta_q) \end{aligned} \tag{2.18}$$

where the mass correction δ_q is:

$$\delta_q = \frac{4M_q^2}{s} \cdot \frac{-\bar{g}_{vq}^2 + \bar{g}_{aq}^2/2}{\bar{g}_{vq}^2 + \bar{g}_{aq}^2} \tag{2.19}$$

For both c, b quarks, the mass correction δ_q is strongly suppressed to $\mathcal{O}(10^{-4})$. The strong suppression for b quark is due to an accidental cancellation among the couplings ($\bar{g}_{vb}^2 \simeq \bar{g}_{ab}^2/2$).

The final state gluon bremsstrahlung will cause an uncertainty of the direction of b quark and reduce the asymmetry by a factor $(1 - \alpha_s/\pi)$. The final state photon radiation, in complete analogy to gluon radiation, reduces the asymmetry by a factor

$(1+\frac{3Q_q\alpha}{4\pi})^{-1}$. It is a negligible effect. The influence of the interference between the initial and final state γ emissions is found to be negligible [2-6] [2-12]. For example, around the Z^0 pole the corrections are of relative order $< \frac{\alpha}{\pi}(\Gamma_Z/M_Z)$. Among the QED corrections, the most important contributions come from initial state photon radiation, which leads to a reduction in the asymmetry. Quantitatively, A_{FB} close to the peak is reduced by ~ -0.025. The forward-backward asymmetries of quarks are extracted by measuring the asymmetries of mesons and baryons endowed with this particular quark flavor. For b quarks this is not a one-to-one correspondence due to the mixing in the neutral B^0-$\bar{B}^0$ system. In case the B mesons and baryons are not identified explicitly, the mixing reduces the observed asymmetry by a factor $(1-2\chi)$, where χ is the mixing parameter.

The forward-backward asymmetry A_{FB} is sensitive to the weak mixing angle $\sin^2\theta_W$. The asymmetry measurement can be used to precisely determine the vector and axial vector coupling constants. Also, the b quark forward-backward asymmetry is sensitive to the top quark mass, Figure 2-4 shows asymmetry and partial decay width at Z^0 peak depending on the top quark mass.

2.4 Heavy Flavor Decay

For heavy flavor mesons, the simplest description of their weak decays is given by the spectator model, as shown in Figure 2-5. In this picture, the initial state meson

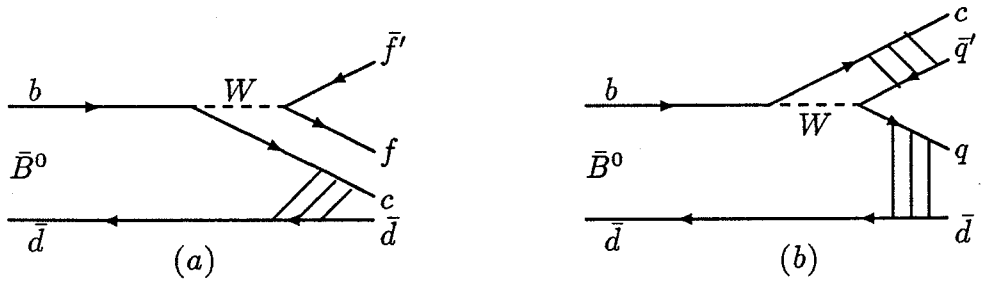

Figure 2-5: *Examples of heavy meson decay in spectator model*

is represented by its valence quark configuration. The heavy quark (c or b) moves and decays freely into light quark by emission of W boson, while another quark acts as spectator having no influence on the meson decay. The dominant weak charge-changing transition of the b quark is to the c quark and a virtual W boson, and less frequently, to u quark. In the decay of charmed mesons, the c quark decays mostly to s quark and a small part to d quark via W emission. Figure 2-5 (b) is the color suppressed spectator process because the quarks from W boson decay have to pick up the same color as the original quarks. Naively thinking, the suppressing factor is 1/3.

If the spectator diagrams were the only possible decay processes for heavy mesons, one would expect that the lifetimes of the heavy neutral and charged meson and their semileptonic branching ratio be the same. In the past, many experiments have been done on charmed hadrons, and one finds the neutral and charged

charmed meson's lifetime and semileptonic branching ratio are different [2-13]. The non-spectator effects can take place in heavy flavor decays:

- The weak annihilation, as illustrated in Figure 2-6. Because of the decay constant [2] and helicity suppression involved in the weak annihilation, it gives a suppression factor of about 10 in charm decays and about 100 in bottom decays in the weak annihilation.
- The interference effects in the decays of charged mesons (Figure 2-7).
- The absence of the "color suppression" expected in the spectator model due to soft gluon effects.

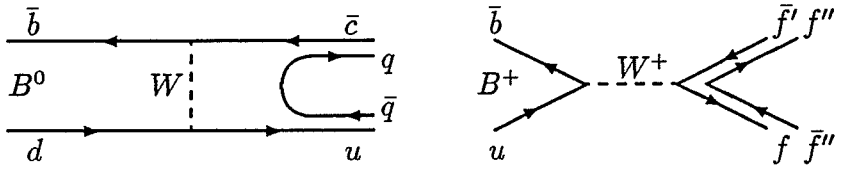

Figure 2-6: *Graphical representation of the heavy flavor weak annihilation*

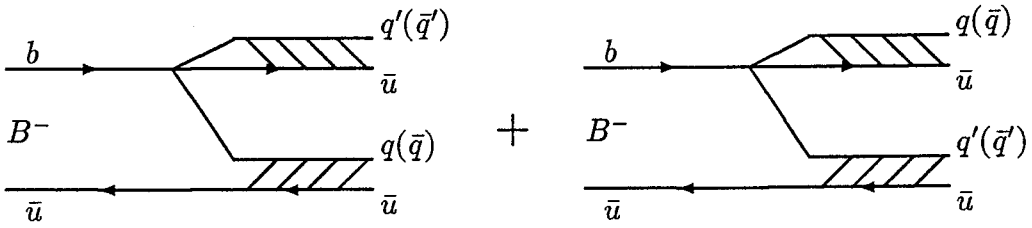

Figure 2-7: *Interference effects in the charged meson system*

Generally, one expects that all these non-spectator effects would decrease the heavy meson's lifetime and semileptonic branching ratio. However, the b quark is more massive than c quark, therefore, for B meson decays, the non-spectator effects are expected to be smaller as compared to D meson decays.

From the spectator model (Figure 2-5(a)), the semileptonic decay width of heavy flavors can be obtained when the W boson couples to a lepton l (e, μ, τ) and its antineutrino [2-14]. In the ACCMM model the semileptonic width of B mesons is given by:

$$\Gamma(B \to l\nu X) = \frac{G_F^2 M_b^5}{192\pi^3}(f_c|V_{cb}|^2 + f_u|V_{ub}|^2) \tag{2.20}$$

with

$$f_q(q = u, c) = S(b \to q)I(\frac{M_q}{M_b}, \frac{M_l}{M_b}, 0) \tag{2.21}$$

[2]Decay constant is proportional to the overlap of the wave functions for the heavy quark and the light quark inside the meson. It depends on the internal structure of the meson.

where parameters f_q account for the phase space corrections (I) due to fermion masses and the QCD corrections (S). Considering $M_l/M_b \approx 0$ for muon and electron and defining $\epsilon_q = M_q/M_b$, the corrections are:

$$\begin{aligned} I(\epsilon_q, 0, 0) &= 1 - 8\epsilon_q^2 - 24\epsilon_q^4 ln\epsilon_q + 8\epsilon_q^6 - \epsilon_q^8 \\ S(b \to q) &= 1 - \frac{2\alpha_s(M_b^2)}{3\pi}[(\pi^2 - \frac{31}{4})(1-\epsilon_q)^2 + \frac{3}{2}] \end{aligned} \tag{2.22}$$

2.5 Heavy Quark Fragmentation

In the studies of heavy quarks, the flavor dependent fragmentation of quarks into hadrons play an important role. The heavier the quark, the more energy is carried by its hadron, because the inertia carried by the heavy quark is retained in the hadron [2-15]. In the past decades, this hard fragmentation of b and c quarks has been observed in many experiments [2-16]. Figure 2-8 is a structure of typical Z^0 decay into multihadronic event in e^+e^- annihilation. The Z^0 decay can be separated into four stages, as shown in Figure 2-8.

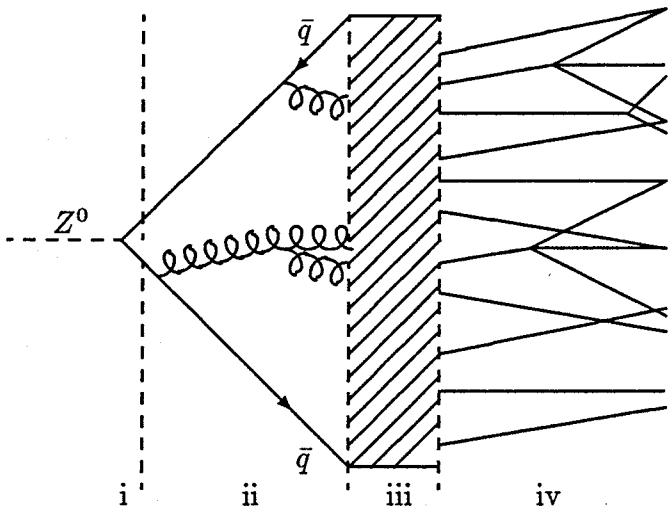

Figure 2-8: *Schematic illustration of a Z^0 decay into $q\bar{q}$*

In the first stage, a primary $q\bar{q}$ pair is produced. This is well understood by electroweak perturbation theory, as discussed before. The second stage is the parton shower process, where the partons (quarks and gluons) are produced. The gluon emission is described by the strong interaction (QCD). As the strong coupling constant α_s is decreased when the CM energy is increased, the perturbative QCD expansion (Matrix Elements) is a good approximation at the Z^0 pole.

In the third stage, the fragmentation process occurs, where the final set of hadrons is produced from an initial set of partons at large distance. This is the shaded area in Figure 2-8. Although we believe this process to be given by QCD, the perturbative QCD no longer applies, and therefore it is an area where phenomenological models have to be introduced to describe the hadronization process, such as string fragmentation (SF), cluster fragmentation (CF) and independent

fragmentation (IF) [2-17]. The last stage is the decay of unstable hadrons into experimentally visible particles. The knowledge of this part mainly comes from experiments.

The cluster fragmentation is a simple description of hadronization, where at the end of the parton shower, a quark is combined with a nearby antiquark to form a colorless cluster. These clusters, which can be regarded as superposition of resonances, subsequently decay into the final hadrons. There are no extra parameters needed for hadronization.

The development of the longitudinal fragmentation process in IF and SF models is parametrised by some probability distribution $f(z)$, where z is the fraction of available energy-momentum, (E+P), carried by the hadron. The variable z is defined by:

$$z = \frac{(E + P_{\parallel})_{hadron}}{(E + P)_{quark}} \tag{2.23}$$

In string fragmentation models, the fragmentation proceeds along the color-flux lines stretched between quarks and gluons. As the q *and* $\bar{q}$ move apart, the string is stretched and may break by producing a new $q'\bar{q}'$ pair. Then two colorless systems $q\bar{q}'$ and $q'\bar{q}$ are formed. The sharing of energy and momentum is given by a probability distribution $f(z)$. If the invariant mass of either of these string pieces is large enough, the string pieces may break again, until only the on-mass-shell hadrons remain. Here each hadron corresponds to a small piece of string. The advantage of this model is that energy and momentum are conserved locally at each step of the hadronization process. In the IF approach, it is assumed that any parton system fragments independently into hadrons and the fragmentation process is similar as the SF models. For light quarks (u, d, s), the fragmentation function [2-17] is taken as:

$$f(z) = 1 - a + 3a(1 - z)^2 \qquad with\ a = 0.77 \tag{2.24}$$

For heavy quarks (c, b), with harder fragmentation, the Peterson *et al.* fragmentation function [2-18] is widely adopted:

$$f(z) \propto [z(1 - \frac{1}{z} - \frac{\epsilon_q}{1 - z})^2]^{-1} \tag{2.25}$$

where the ϵ_q is a free parameter, on expects $\epsilon_q \propto 1/M_q^2$.

The Lund symmetric fragmentation function [2-6] [2-19] are also used in SF models, which gives the probability distribution as a function of the hadron transverse mass $M_\perp^2 = M^2 + P_\perp^2$

$$f(z) \propto \frac{1}{z}(1 - z)^a \exp[\frac{-bM_\perp^2}{z}] \tag{2.26}$$

where a and b are free parameters and are weakly flavor dependent.

2.6 B^0-$\bar{B}^0$ Mixing

Flavor changing weak interactions induce an oscillation between B^0 and $\bar{B}^0$, the box diagram contribution to B^0-$\bar{B}^0$ mixing from the exchange of two heavy top quarks

is illustrated in Figure 2-9. The B^0 and $\bar{B}^0$ mesons, which are flavor eigenstates,

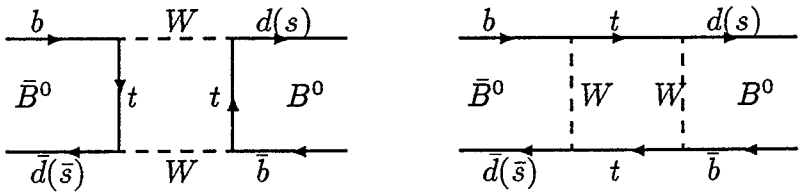

Figure 2-9: *Box diagrams for B^0-$\bar{B}^0$ oscillation*

are not mass eigenstates. The mass eigenstates B_1 and B_2 are linear combinations of B^0 and $\bar{B}^0$ mesons, neglecting CP violation one gets (a good approximation):

$$|B_{1,2}>=\frac{1}{\sqrt{2}}(\pm|B^0>+|\bar{B}^0>) \tag{2.27}$$

The strength of B^0-$\bar{B}^0$ oscillation is measured by determining the mixing parameter $\chi_d(\chi_s)$

$$\chi_d=\frac{Prob(B_d^0\rightarrow\bar{B}_d^0)}{Prob(B_d^0\rightarrow B_d^0)+Prob(B_d^0\rightarrow\bar{B}_d^0)}=\frac{x_d^2+y_d^2}{2(1+x_d^2)}\approx\frac{x_d^2}{2(1+x_d^2)} \tag{2.28}$$

where the quantity x_d and y_d are defined as $x_d=\Delta M_d/\Gamma_d$ and $y_d=\Delta\Gamma_d/(2\Gamma_d)$, Γ_d is the average decay width of B_1 and B_2, ΔM_d and $\Delta\Gamma_d$ are the mass and lifetime differences between two mass eigenstates, respectively. Because the b quark is heavy, the lifetimes of all b mesons are almost the same, i.e., $\Delta M_d \gg \Delta\Gamma_d$. From the box diagrams, where the top quark contributions are dominant for B^0-$\bar{B}^0$ mixing as shown in Figure 2-9, one can obtain x_d (x_s) [2-20]:

$$x_d=\frac{G_F^2}{6\pi^2}B_B f_B^2 M_b\tau_b|V_{tb}^*V_{td}|^2M_t^2\eta_{QCD}S(\frac{M_t^2}{M_W^2}) \tag{2.29}$$

with

$$S(x)=\frac{x}{4}[1+\frac{3-9x}{(x-1)^2}+\frac{6x^2lnx}{(x-1)^3}] \tag{2.30}$$

where B_B is the 'bag' factor, f_B is the B decay constant and τ_b is the lifetime of B hadrons. The values of B_B and f_B are the main sources of uncertainty, $B_B = 0.98\pm0.25$ and $f_B\sim 140\ MeV$ [2-20]. $\eta_{QCD}\approx 0.85$ is a correction factor [2-20].

The formulae of the B_s^0-$\bar{B}_s^0$ system are in complete analogy to the formulae of the B_d^0-$\bar{B}_d^0$ system, just replacing the subscript d by s. χ_d has been measured to be 0.16 ± 0.04 by ARGUS and CLEO [2-21]. From Equation 2.29 one can get:

$$\frac{x_s}{x_d}=\frac{|V_{tb}^*V_{ts}|^2}{|V_{tb}^*V_{td}|^2}=(\frac{|V_{ts}|}{|V_{td}|})^2 \tag{2.31}$$

by assuming that all other factors are the same. Using CKM matrix elements [2-6], one obtains $x_s/x_d\approx 10$ with large error. Together with χ_d measurement, this indicates $\chi_s\approx 0.5$ which means full mixing in the B_s^0-$\bar{B}_s^0$ system.

Chapter 3

LEP Machine

3.1 Introduction

In elementary particle physics one studies the ultimate constituents of matter and the fundamental interactions between them. Today most of the experimental work in this field is concentrated around large accelerators, where charged particles are accelerated to high energy and made to collide with target material or with each other and their reaction products are studied. High energy is desirable for two reasons: firstly, because one needs extremely short wavelengths to study the small scale of the elementary constituents of matter, and secondly due to many of the fundamental particles are massive and require correspondingly high energies for their creation and study. Because the initial state is well defined and the background is small, which can be calculated precisely, the e^+e^- storage ring is favored in studying the electromagnetic and weak interactions.

3.2 The LEP machine

The Large Electron Positron (LEP) [3-1] collider (see Figure 3-1), which has been operating since August 1989, is one of the largest colliders developed for the experimental high energy physics. The machine is in a tunnel with a circumference of 27 km, about 100 m deep under ground. It is located at the French Swiss border near Geneva. Bunches of electrons and positions with an energy $\approx 45\ GeV$ circulate in opposite directions through a beam pipe. More than 3000 bending magnets and almost 2000 focusing and correction magnets keep the beams in place. The main LEP ring's parameters are given in Table 3.1.

The positrons are created by directing an intense pulsed electron beam (100Hz), accelerated to 200 MeV by a linear accelerator, onto a tungsten target. The emitted positrons are accelerated to 600 MeV by a second linac and are injected into an Electron-Positron Accumulation ring (EPA). After a certain time, when a total of 2×10^{11} positrons have been collected, they are transferred into the PS (Proton Synchrotron) and are accelerated to 3.5 GeV, then injected to the SPS (Super Proton Synchrotron). The SPS boosts the positrons to 20 GeV and completes the

Circumference	26658.883 m
Dipole bending radius	3096.175 m
Phase advance/period	60°
Horizontal betatron wave number	70.44
Vertical betatron wave number	78.20
Number of bunches per beam	4
Number of interaction points	4
Number of RF cavities	128
RF frequency	352.20904 MHz
Injection energy	20 GeV
Maximum beam energy	$\sim$ 60 GeV
Peak luminosity (3 mA beam current)	$1.6 \times 10^{30} cm^{-2} s^{-1}$

Table 3.1: *Principal LEP parameters (Phase I)*

pre-accelerating chain. The same cycle is for electrons, but the electrons are directly injected into the 600 MeV linac by an electron gun. The LEP ring receives 20 GeV electrons and positions, four bunches each, circulating in opposite directions. They are simultaneously accelerated to the final energy. Then the electrons and the positrons are focused to collide at the four LEP experiments. The approximate bunch size is $\sigma_x \approx 250\mu m$, $\sigma_y \approx 15\mu m$ and $\sigma_z \approx 15mm$ for horizontal, vertical and the beam direction respectively.

Because of synchrotron radiation, the large size of the LEP ring is required to keep the radiative energy losses of the circulating beams low enough. The electrons and positrons radiate 117 MeV per turn at 45 GeV, which is compensated by a series of Radio-Frequency (RF) cavities [3-2]. During the 1990 period, the typical single beam currents were 1.5 mA, a peak luminosity of 6×10^{30} $cm^{-2}s^{-1}$ was recorded by LEP. The beam intensity decreases slowly with time after injection, mainly due to beam-beam bremsstrahlung losses. After about 7 hours a refill is needed.

The LEP beam energy is measured from a field measurement in a reference magnet which can be calibrated absolutely from the flux change in a loop embracing all LEP dipoles during magnetic cycling. By injecting a 20 GeV proton beam into the LEP ring and measuring the revolution frequency, the LEP absolute beam energy was calibrated to 20 MeV precision with an energy spread of $\sim$ 10 MeV. The relative energy error is 2×10^{-4} at 45 GeV. The detailed description can be found in Reference [3-3].

Chapter 4

The L3 detector

4.1 Introduction

Historically, most of the major discoveries at particle accelerators had been made with detectors designed to measure precisely both the lepton and the photon channels, because the photon and/or leptonic channels provide a clean signal with small background which is easy to understand and to control.

The L3 detector [4-1] (Figure 4-1) is one of the four large detectors [4-2] designed for the new generation of electron-positron accelerators and is strongly emphasising high precision lepton and photon measurements both in momentum and direction. Also the energy flow of hadronic jets and vertices are measured. The L3 detector is located in a cavern which is 50 meters underground at the LEP interaction point 2, in France. Going outward from the interaction point, the following major detector components are installed:

- A vertex chamber, which measures the charged particles track with a 58 μm average single wire accuracy in the bending plane and 640 μm double track resolution. In the non-bending plane, it provides 500 μm single track resolution and 7 mm double track resolution on the Z coordinates.

- An Electromagnetic CALorimeter (ECAL) with 22 radiation lengths is made of a new type of crystals BiGeO (BGO), which measures the energy of electrons and photons with an energy resolution of 1.5% for $E > 2\ GeV$ and 5% at $E = 100\ MeV$.

- A layer of 30 scintillation counters, which are located between the electromagnetic and hadron calorimeter, has a good time resolution $\sim 0.5ns$, as measured from $Z^0 \rightarrow \mu^+\mu^-(\gamma)$. It is used to reject cosmic muons. The scintillation counters cover the polar angle region of $30° \leq \theta \leq 150°$. In the azimuthal angle ϕ, 93% is covered by scintillators.

- A Hadron CALorimeter (HCAL) is made of depleted uranium absorber plates interspersed with proportional wire chambers. It measures hadron energies with a resolution of $(55/\sqrt{E}+5)\%$ and angular resolution of 2.1° for the jets.

It provides a clean muon sample by absorbing hadrons with $\sim$ 6 absorption length and could be used to track the muon.

- The MUon CHamber (MUCH) consists of three layers of large drift chambers, which measures the muon momentum with resolution of 2.5% at 45 GeV.

- The luminosity monitor at small angle, consists of a charged particle tracking chamber with good position resolution and a BGO crystal array with good energy resolution for electrons and photons.

The detector components are supported by a 32 m long, 4.45 m inner diameter Support Tube (ST), centered in the magnet parallel to the beam direction.

The entire detector resides inside a solenoid magnet which provides 0.5 T uniform magnetic field within the detector volume. It has a octagonal shape, 14 m in length, 16 m diameter and 8000 ton in weight. The main components of the L3 magnet are the coil, the yoke and the doors. The amount of magnetic material inside the coil was kept as small as possible to minimize local field inhomogeneities. The field is measured by Hall sensors within the support tube and about a thousand magnetoresistors installed on the muon chambers.

The L3 Detector covers 97% of 4π solid angle for electrons, photons and hadronic jets detection, and 70% for muons. It is complemented by the trigger (TRIG), the online Data acquisition electronics and the online computer system.

4.2 The Central Track Detector

The charged particles originating at or near the interaction point are precisely measured by the L3 central track detector [4-1,4-3] both in their direction and location. The vertex detector identifies the charged and neutral particles and determines the track multiplicity, the trajectories of charged particles, and their momenta. The sign of charged particles can be measured up to $P \approx 50\ GeV$ with 95% CL [4-1]. The L3 central track detector, as shown Figure 4-2, is about 1 meter long and extends from 9 cm to 49 cm in the radial direction from the interaction point and covers the polar angle $|cos\theta| \leq 0.8$. It consists of a Time Expansion Chamber (TEC), a Z-Chamber with cathode strip readout and a PSF (Plastic Scintillating Fiber) calibration system.

The TEC is split into two parts, the inner chamber and the outer chamber. The inner chamber is fitted with the beam pipe, it is subdivided into 12 sectors, each with 30° coverage in ϕ. The outer chamber, extends from 15 cm to 46 cm in radius, and is subdivided into 24 sectors, each with 15° coverage in ϕ. This layout resolves the left-right ambiguity to a large extend for the pattern recognization in the offline analysis. There are three types of signal wires with a sensitive length of 982 mm. Standard Sense wires (anode wires) measure precisely the R-ϕ coordinates. Charge division sense wires (CD) determine the Z coordinates by measuring the charge asymmetry at both ends of the wire. Groups of five grid wires on each side of the amplification region solve the left-right ambiguity (LR). The gas mixture of the

TEC is 80% CO_2 and 20% C_4H_{10}. Flash ADCs operating at 100 MHz are used for the data digitization.

A Z-Chamber, which consists of two layers of cylindrical proportional chambers with cathode readout, was built to enhance the precision of the Z-coordinate measurement in front of the electromagnetic calorimeter. The required spatial resolution is below 2 mm at the surface of the electromagnetic calorimeter. The Z-Chamber is located on the shell of the outer TEC chamber. The gas mixture is 80% Argon and 20% CO_2.

4.3 The Electromagnetic Calorimeter

The BGO (Bismuth Germanium Oxide, $Bi_4Ge_3O_{12}$) is an excellent material for a compact electromagnetic calorimeter because of its short radiation length for photons and electrons, high density, radiation hardness and stable chemical properties. Furthermore, BGO has very high intrinsic resolution ($0.5\%/\sqrt{E}$ for low energies, 1% for $E > 1$ GeV) and excellent linearity. The L3 Electromagnetic Calorimeter (ECAL) [4-1] consists of about 11,000 BGO crystals pointing to the interaction region, designed to measure the energy and the position of electrons and photons in an energy range from 100 MeV up to 100 GeV with high precision.

The ECAL surrounds the Central Tracking Chamber and is composed of a cylindrical barrel (EB), two endcaps (EC) with tracking chambers (FTC) in front, see Figure 4-3. The barrel is made of 7680 BGO crystals, arranged in 48 rings of 160 crystals each, which covers the polar angular region from 42° to 138°. The barrel is mechanically divided two half-barrels symmetrically around $\theta = 90°$. And two endcaps extend the polar angular coverage to 12° and 168°, which contain 1536 crystal each and were installed during the 1990 LEP shutdown. Each crystal is a truncated pyramid with a cross-section of $2 \times 2cm^2$ at the inner end and $3 \times 3cm^2$ at the outer end. The length is 24 cm, corresponding to 22 radiation lengths. The shape of the crystals varies slightly along θ due to variable distance to the interaction point.

Every crystal was calibrated at CERN in the SPS X3 beam, with two fully equipped half barrels at 2, 10 and 50 GeV momenta. The calibration constants are evaluate by using different methods, they agree well with each other. The energy resolution obtained from test beam, 4% at 180 MeV, 1.5% at 2 GeV and 0.6 at 50 GeV [4-4].

4.4 The Hadron Calorimeter

The Hadron Calorimeter [4-1] is located between BGO and the support tube, from 88 cm to 213 cm radius. It is designed to measure the total hadronic energy by the calorimetric technique to determine the energy flow and to act as muon filter in e^+e^- interactions, together with the BGO crystals. It contains three parts: the barrel, the endcaps and the Muon Filter. The barrel covers the polar range $35° \leq \theta \leq 145°$. The endcaps cover the polar angle region $5.5° \leq \theta \leq 35°$. and $145° \leq \theta \leq 174.5°$. Both barrel and endcaps are over the full azimuthal range. The coverage of the

hadron calorimeter is 99.5% of 4π solid angle. The energy resolution versus energy is obtained from test beam as well as from Z^0 events [4-5] and has the form:

$$\frac{\sigma}{E} = \frac{0.55}{\sqrt{E(GeV)}} + 0.05 \tag{4.1}$$

The barrel and endcaps are constructed with depleted uranium absorber plates sandwiched with proportional wire chambers. Due to the high density of uranium, the L3 calorimeter (ECAL and HCAL) has about 6−7 absorption length for particles produced at the interaction. The uranium radioactivity offers a gamma source for the calibration of the wire chamber [4-6]. The gas wire proportional chambers are made of planes of brass tubes. The barrel anode wires in adjacent chamber planes are oriented at right angle to each other for determining both z and ϕ coordinate. The endcap wires are stretched azimuthally to measure the polar angle θ directly. The signal wires are grouped into readout towers in order to get a better coordinate measurement. All the wires are read out by FASTBUS ADCs and the gas mixture is 80% Argon and 20% CO_2.

The barrel consists of 9 rings of 16 modules each (Figure 4-4), 6 outer rings of long modules and 3 inner rings of short modules. The innermost ring is centered at the interaction vertex and followed by four rings on either side. Each of the two HC endcaps is constructed of one outer and two inner rings (Figure 4-4), where each ring is split vertically into two half-rings. The Muon Filter is mounted on the inside wall of the support tube and adds 1.03 absorption length to the Hadron Calorimeter. It increases the muon detection efficiency by reducing punch-through. The spatial resolution of single hadron jet is 2.1° [4-5].

4.5 The Muon Chamber

The basis of the design of the L3 Muon Spectrometer (MUCH) [4-1,4-7] is to measure muon momenta with high precision, $\Delta P/P \approx 2\%$ at 45 GeV, corresponding to a mass resolution of about 1.4% on the Z^0 peak. This is achieved using three layers of high precision drift chambers which measure the curvature of the muon track in the region between the support tube and the magnet coil. The spectrometer covers the polar angle range of $44° \leq \theta \leq 136°$, 2.5 meter at the inner radius and 5.4 meter at the outer radius.

The Muon Chambers are supported by two Torque Tubes on rails attached to the exterior of the support tube. They are subdivided into 16 independent modules called Octant, and are mounted on two Ferris wheels, eight on one side and eight on the other side with respect to the interaction region. The arrangement of one octant is shown in Figure 4-5, each octant has a special mechanical structure to support five chambers: one inner chamber (MI), two middle chambers (MM) and two outer chambers (MO). They measure track coordinate in the bending plane, thus the muon momentum, and are called P chambers. The MI, MM and MO is physically divided into 19, 15 and 21 drift cells respectively. Each cell of MI and MO contains 16 sense wires, MM cell has 24 sense wires. In addition, the top

and bottom P-chambers (MI, MO), each is covered by 2 Z-chambers with wires perpendicular to the beam direction to measure the z coordinate along the beam. In order to reduce the effect of multiple scattering, there are no z-chambers for the middle chambers (MM) which are closed by thin aluminum honeycomb with 0.9% radiation length per 2 layers.

The sagitta s, as shown in Figure 4-5 which measures the curvature of the charged track, has the relation with the muon transverse momentum P_T (GeV),

$$P_T \simeq \frac{0.3BL^2}{8s} \tag{4.2}$$

where B is the magnetic field in Tesla, L is the distance between the inner and the outer chambers in meter and sagitta s is in mm. For a 45 GeV muon, the sagitta is 3.5 mm in the 0.5 T magnetic field and $L \approx 2.91$ m.

The P-chambers are filled with a gas mixture of 61.5% Argon and 38.5% Ethane. Z-chambers are composed of two layers of drift cells offset by one half cell with respect to each other to resolve the left-right ambiguity. Chamber gas mixture is 91.5% Argon and 8.5% Methane. All the wires (27,648 for P-chambers, 7,680 for Z-chambers) are connected via amplifiers to discriminators, then digitized by FASTBUS TDCs with a resolution of 2.2 nsec/bit. Parallel TDCs outputs without time information are used for the muon trigger based on a fast track finding algorithm.

A momentum resolution of 2.5% is reached at $P_\mu = 45$ GeV. In the angular region $35° \leq \theta \leq 44°$ and $136° \leq \theta \leq 145°$, muon are measured by two chambers, MI and MM, which covers about 12% solid angle. A resolution of 15% is achieved. The uncertainty of muon energy loss in the calorimeter is determined to be ~ 350 MeV, and the momentum resolution is

$$\frac{\Delta P_\mu}{P_\mu} = \frac{\sqrt{2.79 \times 10^{-7} P_\mu^4 + 0.1225}}{P_\mu} \qquad for \ \ |\cos\theta| \leq 0.719 \tag{4.3}$$

$$\frac{\Delta P_\mu}{P_\mu} = \frac{\sqrt{1.11 \times 10^{-5} P_\mu^4 + 0.1225}}{P_\mu} \qquad for \ \ 0.719 < |\cos\theta| \leq 0.819 \tag{4.4}$$

for the measured muon momentum more than 2.6 GeV.

4.6 The Luminosity Monitor

The luminosity monitor [4-1] is designed for luminosity measurements with 1% precision by using small angle Bhabha scattering events. It consists of two identical cylindrical BGO electromagnetic shower detectors and two identical charged particle tracking chambers with good position resolution. They are situated on either side of the interaction point, at $z = \pm 2765$ mm. As shown in Figure 4-6, the BGO crystals are arranged in eight rings, each 15 mm thick, parallel to the beam pipe. Azimuthally, they are divided into 16 sectors of 19 crystals each. The luminosity monitor covers the forward angular region, 24.7 $mrad \leq \theta \leq 69.3$ $mrad$ with full efficiency, corresponding to an effective Bhabha cross section of ≈ 100 nb.

4.7 Trigger and Data Acquisition System

The L3 Trigger System [4-1,4-8] is composed of three levels. After each beam crossing, which occurs at a frequency of 45 kHz, the trigger decides if an e^+e^- interaction took place and reduces the rate to a few Hz of tape writing speed. FASTBUS is chosen for Data Acquisition (DAQ) due to its high speed and flexibility. A VAX 8800, clustered with small VAXes for each of the main detector components and several VAXstation, are used to take data. The quality of the accepted data is monitored and the detector parameters are also monitored for detector calibration and safety (slow control). The typical DAQ live time is about 96%.

4.7.1 The Level-1 Trigger

The Level-1 Trigger is operated at 45 kHz, i.e. within 22 μs it decides either to start digitization and store the detector data or to clear the front end electronics. Due to the low background conditions in LEP, it is possible to reduce the rate to a few Hz without losing physics by using level 1 trigger only. A negative decision at level 1 clears the event immediately and does not contribute to the dead time. The digitization of the BGO detector takes about 4 ms, so 10 Hz of level 1 rate corresponds to a dead time of 4%. The Level-1 Trigger consists of the Calorimeter Trigger, Muon Trigger, Scintillator Trigger and TEC Trigger, its decision is the logical OR of above subtriggers. The Calorimeter Trigger, Muon Trigger and Scintillator Trigger are mainly built with CAMAC modules. The CAMAC bus is only used for initialization and testing purposes. The trigger data flow on front panel to make a fast decision. The Trigger Control BOX (TBOX) synchronizes the data acquisition and the level-1 trigger with the beam crossing.

Calorimeter Trigger

The Calorimeter Trigger processes the information given by the BGO, Hadron Calorimeter and Luminosity monitor (256, 384 and 32 channels respectively) and makes trigger decision. The threshold of every channel is 1 GeV. It has following different subtriggers:

- **Total energy trigger (~ 0.2 Hz):**
  The total amount of energy detected is above a predefined threshold, which is different for different region:

  1. The energy in all calorimeters must be larger than 20 GeV;
  2. The energy in EBAR and HBAR must be larger than 15 GeV;
  3. The energy in EBAR only is more than 10 GeV;
  4. The energy in ECAL is larger than 20 GeV.

- **Cluster trigger (~ 1.2 Hz):**
  At least one cluster with energy more than 7 GeV, where the cluster is defined

a localized deposit of energy observed in different detector layers at the same θ, ϕ coordinate.

- **Hit counting trigger ($\sim 0.2\ Hz$):**
  The energy in one of more trigger cells is above a certain value.

- **Single photon ($\sim 2.1\ Hz$):**
  The BGO detector energy is confined to a small region and the ratio of this energy over total BGO calorimeter energy is bigger than 80%.

- **Luminosity trigger ($\sim 0.6\ Hz$):**
  More than 15 GeV in both monitors or one monitor energy above 25 GeV and the other's more than 5 GeV.

- **Single tag trigger ($\sim 0.2\ Hz$, prescaled from 3.2 Hz):**
  The energy of one luminosity monitor is above 30 GeV. This trigger is used to check the main Luminosity trigger.

The Calorimeter Trigger rate is about 3.0 Hz.

Muon Trigger

The Muon Trigger uses the information of trigger cells from MUCH and searches for tracks pointing to the interaction region. It accepts events with $P_T > 2\ GeV$ in the MUCH. There are three subtriggers:

- **Single Muon trigger ($\sim 2.2\ Hz$):**
  A track with any 2 hits in the 3 layer P-chamber and any 3 hits in the 4 layer Z-chamber is found, this covers angular range of $44° \leq \theta \leq 136°$.

- **Dimuon trigger ($\sim 6.0\ Hz$):**
  A track, where hits are found in 2 out of 3 P-chamber and 1 II or IM Z-chamber in same octant. In addition, at least there is another track with 2 P-chamber hits in one of five opposite octants. The angular region $35° \leq \theta \leq 145°$ is covered.

- **Small Angle Muon trigger ($\sim 4.2\ Hz$):**
  One P-chamber hit in MI and One Z-chamber hit in II/IM together with the same conditions in one of opposite three octants. One track must be in forward region (+z), another in backward region (-z). The angular region $24° \leq \theta \leq 156°$ is covered.

The Muon Trigger rate is about 9.5 Hz. After requiring at least one scintillator counter, it is reduced to 1.5 Hz, mainly due to the rejection of the cosmic rays. Typically the scintillator counter rate is about 5.2 kHz with 2 counters in coincidence of $\Delta t \sim 30\ ns$.

Scintillator Trigger

The Scintillator Trigger, based on the signals of 30 barrel counters, serves as a backup for the energy trigger backup and is useful to monitor their efficiency. The multiplicity trigger asks for the coincidence of 6 out of the 30 barrel counters, the rate is 0.2 Hz. Meantime, the scintillator signals are also sent to the energy trigger for the cluster trigger.

TEC Trigger

The TEC Trigger requires two tracks in the TEC with an opening angle greater than 120° in the $R - \phi$ plane. It serves as a backup trigger for the dimuon and energy trigger. A typical TEC Trigger rate is about 1.5 Hz.

Trigger Control

The Trigger Control synchronizes the whole DAQ system and implements the final level-1 trigger decisions. If the event is accepted by the level-1 trigger, the trigger box sends an ACCEPT signal to all subdetectors to start the data conversion and buffering and to activate the high level trigger. Otherwise, a CLEAR signal is sent out.

4.7.2 High Level Triggers and DAQ System

The Level-2 Trigger is based on all level-1 trigger data, but performs complex calculations. The Level-3 Trigger is embedded in the main flow of the data acquisition. Unlike the level-1 and level-2 triggers, which only have coarse granularity and lower resolution trigger data, the level-3 trigger has access to the complete digitized data with finer granularity and higher resolution. A complicated algorithm is applied to reject background events. In case of a positive level-3 decision, the event is recorded on magnetic tape. During 1989 and 1990 running period, the level-2 and level-3 triggers were in transparent mode.

The DAQ system [4-1] is the combination of electronic readout of all subdetectors and the online VAX system. The system also includes ample buffering capacity to allow asynchronous operation without contributing to the dead time.

Chapter 5

Data Reconstruction

5.1 The Data Sample

The data used in this analysis was acquired from October 1989 to August 1990. In this period, several energy scans around the Z^0 resonance were made with center-of-mass energy ranging from 88.2 GeV to 94.3 GeV. About 70% of the data was accumulated on the Z^0 peak. The L3 detector ran smoothly during this period with an overall data taking efficiency of about 80%. About 130,000 $e^+e^- \rightarrow hadrons$ events were recorded, corresponding to an integrated luminosity of 6.3 pb^{-1}. The runs with detector, trigger and DAQ problems are excluded from this analysis. Small inefficiencies of the detector (for instance, MUCH broken wires etc.) have been simulated by Monte Carlo.

At the beginning of 1990, the endcap Veto Counters was installed in front of the Endcap Hadronic Calorimeter. Because it is in the forward-backward region, this has only a small effect for the inclusive lepton analysis. The TEC was improved at the same time and fully operating during the 1990 LEP running period. In order to reduce systematic uncertainties due to the detector modifications, the data from the 1989 runs was not used for Z^0 partial decay width, leptonic branching ratio and fragmentation function measurements. The data from 1989 runs was used only to measure the heavy flavor forward-backward asymmetry and the B^0-$\bar{B}^0$ oscillation in inclusive muon analysis. The integrated luminosity is 0.79 pb^{-1} and 5.5 pb^{-1} for the 1989 and 1990 running periods respectively.

Data used in this analysis covered the following ranges of polar angles:

* Central Tracking Chamber : $41° \leq \theta \leq 139°$;
* Electromagnetic Calorimeter (no BGO EndCap) : $42° \leq \theta \leq 138°$;
* Hadron Calorimeter : $5° \leq \theta \leq 175°$;
* Muon Chamber : $35° \leq \theta \leq 145°$;

5.2 The Luminosity Measurement

The time integrated luminosity L is measured by counting small angle Bhabha events in the luminosity monitor:

$$L = \int \mathcal{L} dt = \frac{N_{BB}}{\sigma_{BB}} \tag{5.1}$$

where N_{BB} is the number of accepted Bhabha events and σ_{BB} is the accepted Bhabha cross section. Uncertainty of the luminosity measurement comes from the statistical and systematic errors on N_{BB} and uncertainty of σ_{BB}. For 1990 data, the integrated luminosity reaches a precision of 0.9%, including 0.5% from theoretical uncertainties, 0.3% from Monte Carlo statistics, 0.4% from internal detector geometry and 0.5% from Bhabha event selection criteria. More details of the luminosity analysis can be found in [5-1].

5.3 Event Reconstruction

The event reconstruction proceeds in two steps. In the first step, the event is reconstructed in each subdetector separately. In second step it is reconstructed globally, using the results of the first step.

First, the hits of BGO crystal and HC's tower (channel), which are above a certain threshold (9 MeV in the HCAL, 2 MeV in BGO), are identified. The hit coordinate is defined as the geometrical center of the tower or BGO crystal. Then the hits in HC are grouped into geometrical clusters (HGCL) by finding two or more adjacent or contiguous hits, for more detail, see the reference [5-2]. A BGO bump (EBMP) is formed by grouping the most energetic BGO crystal with adjacent crystals. Typically an electromagnetic shower deposits $\sim$ 76% in one BGO crystal for central impact. Afterwards, the BGO bump and HGCL in the same direction are merged to form the cluster. The type (hadronic and electromagnetic) of clusters is determined from their transverse and longitudinal profile, and by the ratio of the energy deposited in the BGO and the HCAL. Different calibration constants are applied to calculate the energy. The cluster direction is defined as the vector sum of all the hits it contains (the vector origin is the interaction point). The hits in muon chamber are reconstructed to form local segments and the tracks are reconstructed from different chamber segments. The total average energy loss of muons in the calorimeter is about 2.6 GeV.

The global reconstruction algorithm starts from the most energetic cluster. A new axis is calculated by summing the energy-weighted vector of all the clusters within a 30° cone of this cluster axis, and a new 30° cone is defined from this new axis. From this new axis, the procedure is repeated again until there is no new cluster to be added. The clusters in a 30° cone of this axis form a jet, and the final axis is called jet-axis. The jet thrust is defined as:

$$T_{jet} = \sum_i \vec{E}_i / \sum_i |E_i| \tag{5.2}$$

where $\vec{E}_i$ is the cluster vector. The procedure is repeated to find all the jets. All charged and neutral hadrons are included to reconstruct jets, where jet energy is required to be larger than 2 GeV. In the end, the clusters not connected to any jet are included by the nearest jet. Finally, the jets are classified (hadronic, electromagnetic, single muon and single electron etc.) and their energies are determined. Typically, the jet energy is contained within a 10° cone with respect to the jet axis. The jet angular resolution is about 2° [5-2]. The event shape variables, such as Thrust, Major and Minor etc., are determined. The thrust axis, which is the direction maximizing the projected energy flow, is defined as:

$$T = max(\sum_i |\vec{E}_i \cdot \vec{n}_T| / \sum_i |E_i|) \tag{5.3}$$

$\vec{n}_T$ is the thrust direction. The thrust axis points approximately along the original quark direction.

Chapter 6

Event Selection

The semileptonic decay of heavy quarks, which is characterized by leptons of high momentum p and transverse momentum $p_\perp$, is expected to proceed via a charged current interaction. In the past, leptons have played an outstanding role in the tagging of heavy flavors. As an example, Figure 6-1 shows a semileptonic decay event recorded at L3 detector, where both quarks decay into lepton (one electron and one muon). This chapter outlines the tagging method for heavy flavor and gives a detailed description of lepton identification, acceptance and purity. Muons are identified with the Muon Chambers, and electrons are identified by using BGO and TEC. At the end, the different sources of background are estimated.

6.1 Method of Tagging Heavy Flavor

The L3 detector is designed to measure lepton with high precision, thus providing an easy and reliable way to separate leptons from hadrons. The study of leptons in hadronic decays of Z^0 allows to measure electroweak coupling to the heavy quark and understand the hadronization at this high energy.

The heavy quarks have hard fragmentation and high masses, therefore the leptons, which come from the semileptonic decay of heavy quarks, carry high average momentum p and transverse momentum $p_\perp$. Figure 6-2 demonstrates the sources of leptons and gives the average lepton momentum $<p>$ and transverse momentum $<p_\perp>$, where the $p_\perp$ is calculated with respect to the nearest jet axis. All those studies are done in the Monte Carlo without detector simulation. The average $<p>$ and $<p_\perp>$ of decay leptons are 1.77 GeV and 0.27 GeV, which is much lower than the $<p>$ and $<p_\perp>$ of leptons from b or c decays. Thus the momentum and transverse momentum enable to separate signal and background. By requiring a high lepton momentum (typically 3 GeV), the misidentified leptons, gamma conversions, π and K decays are strongly suppressed. Especially for b semileptonic decays, the average p and $p_\perp$ of prompt lepton are 8.34 GeV and 1.27 GeV respectively, which are much higher than those from other sources. By using lepton p and $p_\perp$ as selection variables, one can have data sample of $b\bar{b}$ event with high purity. However, the misidentification of leptons and the lack of precise knowledge of the heavy flavor

Prompt Leptons

(1) $b \to l^-$

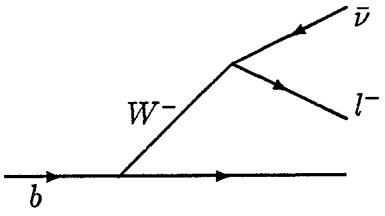

$<p> = 8.34\ GeV$
$<p_\perp> = 1.27\ GeV$

(2) $c \to l^+$

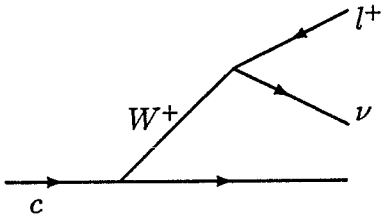

$<p> = 4.49\ GeV$
$<p_\perp> = 0.51\ GeV$

Cascade Leptons

(3) $b \to \tau^- \to l^-$

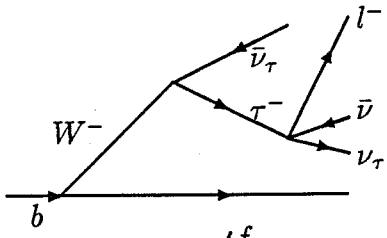

$<p> = 4.55\ GeV$
$<p_\perp> = 0.72\ GeV$

(4) $b \to c \to l^+$

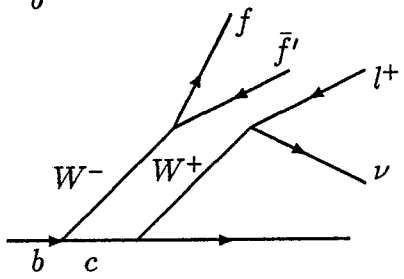

$<p> = 3.10\ GeV$
$<p_\perp> = 0.48\ GeV$

(5) $b \to \bar{c} \to l^-$

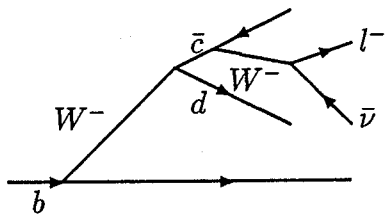

$<p> = 3.09\ GeV$
$<p_\perp> = 0.47\ GeV$

Background

(6) Decay Lepton: muon $\pi^\pm, K^\pm \to \mu^\pm \nu$ $<p> = 1.77\ GeV$

electron $\gamma \to e^+e^-$, $\pi^0 \to e^+e^-\gamma$ $<p_\perp> = 0.27\ GeV$

(7) Fake Lepton: muon hadronic punchthrough and sailthrough

electron $\pi^\pm$, $K^\pm$, *overlap of* $\pi^\pm + \gamma$, $\pi^\pm + \pi^0$

Figure 6-2: *Sources of inclusive leptons*

decay and hadronization remain the main sources of systematic uncertainty.

Due to the small inner tracking chamber (TEC) in L3, the and background from $\pi^{\pm}, K^{\pm}$ decays in flight is small. This is important in the inclusive muon analysis. The muons are measured after penetrating the BGO, hadron calorimeter and muon filter. Misidentification of muons, such as the punchthrough from the hadronic showers and minimum ionizing hadrons, is highly suppressed due to the thick calorimeter absorber. And only few simple selection criteria are needed to identify muons. The clean data sample and high selection efficiency give small systematic errors for inclusive muon analysis.

The observed average numbers of charged particles, $\pi^0 s$ and $K^0 s$ per event are 20.7, 6.4 and 2.0 respectively [6-1]. To identify electrons from the hadronic environment with more than 10 charged pions and kaons is a difficult task. The BGO has an energy resolution of 1.5% for $E > 2\ GeV$ and good angular resolution for electrons and photons. The angular resolution of BGO is at the order of $1 \sim 2\ mrad$ depending on the electron and photon energy. Together with hadron calorimeter and TEC, which has 50 μm average single wire accuracy and 640 μm double track resolution, the electrons can be separated from the hadronic environment.

6.2 Selection of Heavy Flavor Events

There are two steps in the offline event selection. First, the raw data is reconstructed by the L3 reconstruction program, and then pass 1 selections with very loose cuts are applied. The selected events are split into different data sets according to physics interests. After pass 1, a more specific selection (so called pass 2) is applied to extract clean data samples for particular physics processes which can be used for detailed physics study.

Heavy flavor events are identified by the observation of a hadronic event containing a lepton coming from the semileptonic decay of the heavy quark, Figure 6-1 is such an event. To select these events, hadronic events are first selected by using the following criteria:

(1) $0.42 < E_{vis}/\sqrt{s} < 1.5$ and $\mathrm{E_{cal}} > 30\ GeV$
The cut is shown in Figure 6-3, the events in the low energy region are mainly from the two photon process, beam gas and $Z^0 \rightarrow \tau^+\tau^-(\gamma)$, which are not simulated in the distributions. This cut removes events of the two photon process, beam gas, cosmic ray background and dimuon events. Part of the $\tau^+\tau^-(\gamma)$ events are also rejected.

(2) Transverse energy imbalance $E_{\perp}/E_{vis} < 0.5$
Longitudinal energy imbalance $|E_{\parallel}/E_{vis}| < 0.4$
The $\tau^+\tau^-(\gamma)$, beam gas and beam-pipe events are reduced further. Also the electrical noise in a few detector cells would be cutoff by requiring energy balance.

(3) $N_{cluster} > 15$
The clustering algorithm normally reconstructs only one cluster for each iso-

lated muon, each electron or photon shower. Since dimuon, di-electron and $\tau\tau$ events have low multiplicity, they are excluded by this cut. Figure 6-4 gives example, where the low multiplicity events come mainly from the dilepton events and no Monte Carlo simulation of those processes is in the plots. Also, the events from "two photon processes" and cosmic ray are rejected by requiring certain number of clusters.

where E_{cal} is the total energy observed in the calorimeter and E_{vis} is the sum of the calorimeter energy and energy of the muon as measured in the muon chambers. $E_\perp$ and $E_\parallel$ are the energy imbalances perpendicular and parallel to the beam direction, they are calculated according to the following formulae:

$$E_\perp = (\sum \vec{E}) \times \hat{z} \qquad\qquad E_\parallel = (\sum \vec{E}) \cdot \hat{z} \tag{6.1}$$

where $\hat{z}$ is the unit vector along the electron beam, and $\vec{E}$ is a vector of every reconstructed energy cluster in the calorimeter, the muon momentum is included in this vector sum.

Applying these cuts to a sample of simulated events, the resulting acceptance, including detector inefficiencies, is (97.08±0.04)% (statistical error only) for hadronic decays of the Z^0. The contribution to the event sample from the $\tau^+\tau^-(\gamma)$, $e^+e^-(\gamma)$, and "two-photon process" $e^+e^- \rightarrow e^+e^- + hadrons$ is less than 0.5%.

6.2.1 Muon Identification

The following cuts are required to select inclusive muon events.

(4.m) To avoid misidentification, it is required that a muon track consists of at least two P-segments in three layers of muon chambers. There must be 1 or more Z-segment in order to have a correct muon track direction and determine muon $p_\perp$ with respect to the nearest jet (without muon).

(5.m) The muon track is required to point to the interaction region to reject the punchthrough. Multiple scattering in the calorimeter and a poorly measured muon track (some doublets and tracks passing near chamber edges) can effect the vertex measurement. The multiple scattering contributes about 40 mm for 10 GeV muon, which is much larger than the uncertainty due to the LEP beam size (see Chapter 3). Reconstruction errors are negligible even though occasionally they can yield vertex measurements, which are several centimeters away. The muon's transverse distance of closest approach (DCA) to the interaction point is required to be less than 200 mm in the $R-\phi$ plane, and the DCA in the $R-Z$ plane is required to be less than 500 mm. In addition, the transverse DCA of the muon track should be smaller than $3\sigma_{x,y}$, and the longitudinal DCA should be less than $4\sigma_z$. The σ is defined as the associated error of DCA. The effects of multiple scattering of the muon in the calorimeters are included in the errors.
The hadronic punchthrough and decay muons produced at large distance from

vertex have large DCAs. They are rejected by requiring that the muon track point to the interaction points. Figure 6-5 illustrates the reconstructed DCA and σ distributions, both of the data and the Monte Carlo.

(6.m) At low momentum, one finds a large contributions from hadronic shower punchthrough, minimum ionizing hadrons (sailthrough) and decay muons. Therefore it is required that the muon momentum should be larger than 4 GeV. It is also required that $p < 30$ GeV to reject mismeasured muon tracks.

The muons are uniformly distributed in the $R-\phi$ (Figure 6-6(a)). The polar angle $\cos\theta$ distribution is shown in Figure 6-6(b), there are much less events around $\cos\theta = 0$ due to Muon Chamber geometrical acceptance.

Because the negative particles, such as π^-, K^- and $\bar{p}$, have stronger nuclear interaction with nucleus (larger inelastic cross section) compared with its counterpart and are absorbed by calorimeter, there are more positive hadronic sailthrough, punchthrough and decay muons which are passing through muon chamber. In the data, the number of observed positive muons is more than the number of negative muons in hadronic events around 3.5 GeV, the low momentum region.

6.2.2 Electron Identification

Electrons leave a track inside the TEC and are absorbed in the BGO. Photons have no track in the TEC. Candidate electrons are identified using the BGO, hadron calorimeters and the tracking chamber by a two-step process. First, electromagnetic clusters in the BGO calorimeter are found then are associated with a charged track. In a hadronic event, the electromagnetic cluster is identify by looking for an energetic cluster in the BGO calorimeter which contains at least 9 adjacent crystals each with more than 10 MeV. The following conditions must be satisfied:

(4.e) The ratio of the energy measured in the 3×3 array centered on the most energetic crystal and the energy measured in the 5×5 array, E_9/E_{25}, where both energy measurements have a position-dependent leakage correction applied. The E_9/E_{25} must be larger than 0.95.

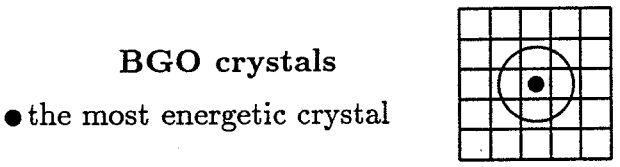

For an isolated electromagnetic shower, E_9/E_{25} has an approximately Gaussian distribution, centered at 1.01 with a width of 1%. The distribution shown in Figure 6-7(b) has been obtained from Bhabha events, it is well peaked at 1.01 with a width of $< 1\%$. For hadronic showers, or for electromagnetic showers that have been contaminated by a nearby shower, E_9/E_{25} will be smaller than 1. As shown in Figure 6-7(a), most hadronic background is removed by

applying a E_9/E_{25} cut. Monte Carlo does not simulate the electromagnetic shower perfectly, there is a shift of the peak position of about 0.004 in the Bhabha distribution as shown in Figure 6-7(a). Similar effect is seen for in inclusive electrons (Figure 6-7(b)). Therefore the different cuts are applied for data and for Monte Carlo. For the data, E_9/E_{25} is required to bc larger than 0.946 instead of 0.95.

(5.e) The BGO is about 1 nuclear interaction length for pions and kaons, this means only 2/3 of pions and kaons will deposit a large fraction of their energy in the BGO. To further reduce the background from the pions and kaons misidentified as electrons, any BGO cluster is excluded with more than 3 GeV of energy deposited in the hadron calorimeter behind the cluster inside a cone of half-angle 7° around its centroid. This distribution is not perfectly simulated by Monte Carlo, the fraction of accepted background events differs with different sets of Monte Carlo by a few percent.

Electromagnetic clusters are identified as electrons, if they fulfill the following requirements:

(6.e) There are TEC track quality requirements. A TEC track is regarded as a good track if the following conditions are met.

- The number of used hits for this TEC track must be more than 40.
- The track span must be larger than 50, where the span is the difference between first and last wire number. Typically this corresponds to a track length of 40 cm.
- The DCA of the TEC track in $R-\phi$ plane is within 5 mm.
- The measured transverse momentum of the track with respect to the beam direction is larger than 2 GeV and smaller than 35 GeV.

(7.e) The track in the central tracking chamber must match within $\Delta\phi$ 5 mrad in the azimuthal angle with the centroid of the electromagnetic shower. In order to avoid a wrong match because of two or more nearby TEC tracks, there should be no other track within 10 mrad of the previous track. Since the center of the BGO and the center of the TEC were slightly displaced, $\Delta\phi$ depended on the azimuthal angle ϕ (Figure 6-8(a)). Also, the BGO crystal does not exactly point to the interaction point, this has similar effects. The following correction has been applied for $\Delta\phi$ as function of the azimuthal angle,

$$\Delta\phi_{corr} = \Delta\phi + A\sin(\phi + B) + C$$

The parameters A, B and C are fitted from the data and are determined to be 2.71 mrad, -2.98 rad and -0.71 mrad with $\chi^2 = 1.40$ per degree of freedom. Figure 6-8(b) and Figure 6-8(c) show the $\Delta\phi$ distribution after the corrections.

(8.e) Tracks going through region with lower resolution adjacent to the anode and cathode planes are excluded to avoid charge confusion.

(9.e) In order to reject the background due to energetic photons and π^0's that have been accompanied by a nearby charge track, the ratio of the electromagnetic energy measured in the BGO calorimeter and the momentum measured in the tracking chamber (E/p) is required to be less than 1.5. Figure 6-9(a) shows the qE/p distribution for electron candidates which pass all other cuts, where the charge of the electron is determined by the tracking chamber. Figure 6-9(b) also shows the same plot by removing the cut (8.e). In Figure 6-9, two well-separated peaks are visible at ± 1, the small value of E/p are due to the charged pions and kaons where only certain fraction of their energy is deposited in the BGO. The upper limit of charge confusion is estimated to be 1% for $3\ GeV < E < 35\ GeV$. This is verified with $e^+e^- \rightarrow \tau^+\tau^-$events [6-2].

(10.e) The energy of the electron candidate should be greater than $3\ GeV$ and less than $30\ GeV$. The electron should be in the angular region $|\cos\theta| < 0.69$.

Because of the difference between Data and Monte Carlo in the cut (4.e) and cut (5.e), the electron selection efficiency has a large uncertainty (3.0% in total). The cut (8.e) was used for the forward-backward asymmetry and mixing measurements to avoid charge confusion, and was not applied for other measurements.

6.3 Monte Carlo Simulation

The Monte Carlo simulation is necessary to study the heavy quark sector and to determine the acceptance and purity for inclusive lepton events. The LUND parton shower program JETSET 7.2 [6-3] with $\Lambda_{\rm LL} = 290\ MeV$ ($\alpha_s(M_Z^2) = 0.115$) and string fragmentation is used to generate Monte Carlo distributions. For b and c quarks the Peterson *et al.* fragmentation function [6-4],

$$f(z) = \frac{N}{z}(1 - \frac{1}{z} - \frac{\epsilon_q^z}{1-z})^{-2} \tag{6.2}$$

was used to describe the hadronization of b and c quarks, where N is a normalization constant and $z = \frac{(E+P_\parallel)_{hadron}}{(E+P)_{quark}}$. For b quarks, the fragmentation function is adjusted to match L3 inclusive muon data [6-5]. The input fragmentation parameters used in the generator are $\epsilon_b^z = 0.008$ for bottom quarks and $\epsilon_c^z = 0.07$ for charm quarks. These values also agree with the extrapolations from the measurements at PETRA and PEP [6-7]. The generated events are passed through the L3 detector simulation [6-6], which includes the effects of energy loss, multiple scattering, interactions and decays in the detector materials and beam pipe. In the Monte Carlo, the b quark semileptonic decay branching ratio is 11.2% and average of branching ratio $Br(c \rightarrow l\nu + X)$ is 10.4%.

6.4 Lepton $p_\perp$ Determination

Because of the large mass of the b quark, lepton from the b semileptonic decay have a large transverse momentum with respect to the B meson direction. Therefore by cutting on this quantity the $Z^0 \rightarrow b\bar{b}$ events are preferentially selected. The $p_\perp$ can be calculated by using different methods, for example:

(i) Thrust Axis

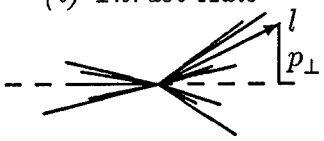

(ii) Nearest Jet Axis

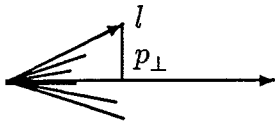

(iii) Nearest Jet Axis, lepton excluded from the Jet

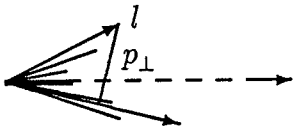

(i) The $p_\perp$ of lepton is defined with respect to the thrust axis. The thrust axis is the direction to maximize the projected energy flow, more or less, it points to the original quark direction.

(ii) The $p_\perp$ of lepton is calculated with respect to the nearest jet, where the lepton momentum is included in the jet axis calculation. Because of the harder fragmentation of heavy flavor (for example, B meson carrys about 70% of original b quark energy), the jet axis gives the flight direction of the heavy meson.

(iii) After the measured momentum of the lepton is excluded in the calculation of the jet axis, the $p_\perp$ of the lepton is calculated with respect to the nearest jet. This definition differs with the previous one (ii).

The following studies come from inclusive muon only. Figure 6-10 gives the angle between the muon and the nearest jet or thrust for different $p_\perp$ definitions. Figure 6-10(i, ii and iii) correspond to the definitions described above, where the Monte Carlo agrees very well with the data, Figure 6-10(iv) is the angle between the muon and original hadrons as defined by Monte Carlo. When the muon is included in the calculation of jet axis, the angular distribution is similar as the angular distribution in Figure 6-10(iv). It is also true for the angle with respect to the thrust, except in Figure 6-10(i) there are tails at large angles mainly due to hard gluon radiations. When the muon momentum is excluded in the jet direction calculation, the angular distribution becomes broad as shown in Figure 6-10(iii) and results in the larger $p_\perp$, especially for high momentum muons.

The muon $p_\perp$ with respect to the original hadrons has a cutoff at 2.2 GeV due to the kinematic limit. The $p_\perp$ calculated with respect to the nearest jet, where the muon momentum included in jet, has similar behavior, while for other definitions there are tails above 2.2 GeV. Figure 6-11 shows the $p_\perp$ difference between the

$p_\perp$ with respect to the nearest jet/thrust and the $p_\perp$ with respect to the original hadrons, the $\Delta p_\perp$ in Figure 6-11(b) is centered around zero for the muons from prompt b decay. The large value of $\Delta p_\perp$ in Figure 6-11(c) is dominated by the muons from the prompt b decay, where the measured muon momentum is taken out from the calculation of jet axis.

Table 6.1 compares the acceptance and purity of prompt and cascade muons with different $p_\perp$ calculations, where the purity of an event category is defined as the expected fraction of events of this category in the data sample. The purity of

jet	$p_\perp$ cut (GeV)	$b \to \mu$	$b \to c(\bar{c}) \to \mu$	$c \to \mu$	remark
Thrust (i)	1.00	30.2%	3.1%	5.7%	accep.
		60.7%	7.4%	11.0%	purity
	1.25	24.4%	2.0%	4.1%	$\Longleftarrow$
		63.9%	6.2%	10.5%	
with μ (ii)	1.00	26.7%	2.3%	2.2%	accep.
		71.6%	7.1%	5.8%	purity
	1.10	23.9%	1.6%	1.7%	$\Longleftarrow$
		74.8%	6.0%	5.1%	
w/o μ (iii)	1.00	33.8%	3.7%	4.9%	accep.
		64.2%	8.6%	8.4%	purity
	1.50	25.6%	1.3%	1.7%	$\Longleftarrow$
		78.1%	4.9%	4.6%	

Table 6.1: *The purity and acceptance for different $p_\perp$ definitions*

$b \to \mu$ is lower by using $p_\perp$ with respect to the thrust axis compared with other methods. For instance, for an acceptance of 25% (see lines marked by "$\Longleftarrow$" in Table 6.1), the purity of the prompt $b \to \mu$ is about 64%, while other methods give about 76%. Also, the $p_\perp$ with respect to the thrust depends on the details of fragmentation. Certainly it is better to use the $p_\perp$ with respect to the jet. Taking the lepton out of the jet reconstruction will give higher $p_\perp$ and enhances the $b\bar{b}$ sample by a few percent. In the following analysis, to determine $p_\perp$ of the lepton, the measured momentum of the lepton is excluded in the calculation of jet direction.

6.5 Acceptance and Purity

Figure 6-12 shows the measured momentum spectrum for inclusive muons and the measured energy spectrum for inclusive electrons after the above selection cuts, and Figure 6-13 shows the measured transverse momentum, $p_\perp$, of each inclusive lepton with respect to the nearest jet. In the calculation of the nearest jet axis, the measured momentum/energy of the lepton is excluded from the jet. If there is no jet with an energy greater than 6 GeV remaining in the same hemisphere as the lepton, then $p_\perp$ is calculated relative to the thrust axis of the event. The Monte Carlo distributions are also shown in these figures and the expected contributions

from different sources are indicated. The prompt $b \to \ell$ events dominate at higher p and $p_\perp$.

Without the $p_\perp$ cut, the acceptance for prompt $b \to \ell$ decays is 39.8% for muons and 18.4% for electrons. The lower acceptance for electrons is due to the identification criteria, which requires the electron to be isolated. The acceptance for prompt $b \to \ell$ decays is listed in Table 6.2. For electrons, the 1 GeV $p_\perp$ cut removes only a small fraction of $b\bar{b}$ events ($1 \sim 3\%$) with a prompt $b \to \ell$ decay, because of the implicit isolation requirements in the electron selection.

Lepton	$p_\perp$ cut	acceptance
μ $p > 4$ *GeV*	0.00	39.8
	1.00	33.8
	1.50	25.6
e $p > 3$ *GeV*	0.00	18.9
	1.00	17.3
	1.50	13.6

Table 6.2: *Monte Carlo estimates of the acceptance for a prompt $b \to \ell$ decay*

Monte Carlo events with leptons are classified into eight categories: prompt $b \to \ell$, the cascades $b \to c \to \ell$, $b \to \tau \to \ell$, and $b \to c + \bar{c} + s$ where $\bar{c} \to \ell$, $b \to$ background coming from b hadron decay, prompt $c \to \ell$, decay lepton and misidentified hadrons as lepton. As discussed before, decay leptons include muons from π and K decays, and electrons from the γ conversion and Dalitz decays. The sources of misidentified hadrons are, for example, $\pi^\pm - \gamma$ and $\pi^\pm - \pi^0$ overlap for electrons and punchthrough for muons. Table 6.3 shows the results of Monte Carlo studies giving the fraction of each lepton source and background for data samples with no cut on $p_\perp$, with 1.0 GeV cut and also with a cut at 1.5 GeV.

Category	μ $p > 4$ *GeV*			e $p > 3$ *GeV*		
	$p_\perp > 0$	$p_\perp > 1$	$p_\perp > 1.5$	$p_\perp > 0$	$p_\perp > 1$	$p_\perp > 1.5$
1: $b \to \ell$	38.4%	64.2%	78.1%	66.9%	77.3%	83.5%
2: $b \to \tau \to \ell$	2.1%	2.0%	1.5%	2.2%	2.1%	1.7%
3: $b \to c \to \ell$	10.7%	7.6%	4.4%	5.5%	4.0%	2.1%
4: $b \to \bar{c} \to \ell$	1.6%	1.0%	0.5%	0.4%	0.2%	0.2%
5: b background	4.1%	2.9%	1.9%	4.4%	3.0%	2.1%
6: $c \to \ell$	17.2%	8.4%	4.6%	3.5%	2.2%	1.5%
7: decay	8.4%	3.8%	2.1%	0.7%	0.4%	0.3%
8: fake leptons	17.5%	10.1%	6.9%	16.4%	10.8%	8.6%

Table 6.3: *Monte Carlo estimates of the fractions of each type of lepton in the data sample*

6.6 Background

Except for the background from decay muons and punchthrough, there are other background sources from e^+e^- interactions, cosmic ray and non e^+e^- interactions (beam gas, beam pipe etc.). The background from hadronic events ($e^+e^- \rightarrow Z^0/\gamma \rightarrow hadrons$) will be discussed later in the analysis. Here, the rate of none hadronic background is estimated.

Cosmic ray is a possible background source for inclusive muon. Most cosmic rays are in the top and bottom of muon chamber, i.e., in the angular region $3\pi/8 \leq \phi \leq 5\pi/8$ (Octant 2) and $11\pi/8 \leq \phi \leq 13\pi/8$ (Octant 6). Figure 6-6(a) is the ϕ distribution of the inclusive muon events, it is a uniform distribution. This is an indication that the background from cosmic ray is small. The cosmic contamination to the $\mu + hadrons$ data sample is estimated from visual scan. The so-called in-time scintillator counter is the measured scintillator times relative to the beam crossing after correcting for time-of-flight within 3.0 ns. Table 6.4 lists the number of events and its fraction with 0, 1 and 2 of in-time scintillator counters for both inclusive muon and electron events, after the events with scintillator DAQ problems, where only 1990 data is used. The number of $\mu + hadrons$ events with 0, 1 and 2 in-time

Type	# of in-time SCNT				remark
	0	1	2	all	
$\mu\nu + X$	2	0	6	5377	
	0.037%	0.0	0.112%	1.0	fraction
$e\nu + X$	1	0	1	1552	
	0.064%	0.0	0.064%	1.0	fraction

Table 6.4: *Fraction and number of inclusive lepton events with different hitted number of scintillator counters*

scintillator counters is 2, 0 and 6 respectively. The inclusive muon events, which has the number of in-time scintillator counters less than 4, are selected and scanned. 1 cosmic event out of 5377 selected events was found, so the cosmic contribution is:

$$\rho_{Bco}^{\mu X} = (0.02 \pm 0.02)\% \tag{6.3}$$

This cosmic event will be excluded from the inclusive muon analysis.

The beam gas and beam pipe backgrounds are estimated from visual scan. The events with low calorimeter energy ($E_{cal} < 50\ GeV$) are selected and scanned. No beam gas and beam pipe event was found out of 114 inclusive muon and 18 inclusive electron events with low calorimeter energy. Because the beam gas and beam pipe events are mainly low energy, we concluded there are no beam gas and beam pipe background in the data sample. In total, there are 1552 inclusive electron events and 5377 inclusive muon events, thus the rate of this type background is estimated less than 0.06% and 0.20% for inclusive muon and inclusive electron respectively. It is negligible.

The background which comes from e^+e^- collisions is studied by Monte Carlo simulation. In the studying, the following Monte Carlo event generate programs are

used to produce corresponding Monte Carlo samples: JETSET 7.2 [6-3] for e^+e^- to hadronic events; KORALZ [6-9] for $e^+e^- \rightarrow \mu^+\mu^-$and $e^+e^- \rightarrow \tau^+\tau^-$events; BABAMC [6-10] for $e^+e^- \rightarrow e^+e^-$ events; TWOGAMMA [6-11] for four-fermion final state. Assuming L_{had} and L_B are the integrated luminosities corresponding to data taking and background processes (Monte Carlo), respectively, and N_B^{acc} events are accepted by the selections from background process and N_l^{acc} events are accepted as inclusive lepton events from $e^+e^- \rightarrow hadrons$, the background rate is calculated:

$$\rho_B = \frac{N_B^{acc}}{N_{had}^{acc}} \cdot \frac{L_{had}}{L_B} \cdot \frac{\epsilon_B^t}{\epsilon_l^t} \tag{6.4}$$

where ϵ_B^t and ϵ_l^t are the trigger efficiencies for the background and the data respectively, and the detection inefficiency is ignored. The trigger efficiencies $\epsilon^t = 1.0$ [6-13] for all the processes.

The background rate is estimated by applying the inclusive lepton cuts to the Monte Carlo events for each process. The main background contribution comes from $\tau^+\tau^-$events, other contributions are are negligible ($< 0.01\%$). Adding all the contributions, the background from none hadronic events is:

$$\rho_B^{\mu X} = (0.04 \pm 0.03)\% \qquad \rho_B^{eX} = (0.38 \pm 0.16)\% \tag{6.5}$$

$\rho_B^{\mu X}$ and ρ_B^{eX} are background for inclusive muon and inclusive electron respectively. The background from none hadronic events is small and negligible.

Chapter 7

Efficiencies

7.1 Trigger Efficiency

There are several independent triggers to trigger the inclusive lepton events. The primary trigger for $e^+e^- \rightarrow l\nu X$ events is from the calorimeter trigger, including the energy trigger and cluster trigger. The energy trigger is designed to accept the events which deposit more than 20 GeV in whole calorimeter or 15 GeV in the barrel region. The cluster trigger requires at least one cluster with energy larger than 7 GeV in calorimeter. In addition, there are another independent triggers for the inclusive lepton events. The scintillator multiplicity trigger requires at least five of the thirty barrel scintillation counters to have been fired and the TEC charged track trigger requires two tracks with opening angle larger than 120° in the central track chamber $R-\phi$ plane. For the inclusive muon events, the muon trigger can be used, which requires one of the thirty barrel scintillation counters in coincidence with a track in the muon chambers. The individual trigger efficiency is determined by combining this trigger with another independent trigger and comparing the number of events triggered by both triggers to the number of events triggered by the independent trigger. For instance, among 5209 inclusive muon events, which are triggered by the TEC trigger, there are 5206 events triggered by the calorimeter trigger. This gives the efficiency of the calorimeter trigger of $(99.94 \pm 0.03)\%$. Table 7.1 shows the efficiency of each trigger for inclusive muon and inclusive electron events respectively. Each trigger can be treated as an independent trigger, hence

Trigger	efficiency of $\mu + X$	efficiency of $e + X$
Cal.	$(99.94 \pm 0.03)\%$	1.00
SCNT mult.	$(96.68 \pm 0.25)\%$	$(98.54 \pm 0.32)\%$
TEC	$(97.82 \pm 0.20)\%$	$(98.47 \pm 0.32)\%$
Muon	$(85.58 \pm 0.49)\%$	—

Table 7.1: *Trigger efficiencies of different triggers for inclusive lepton events*

the combined trigger efficiency is larger than 99.99% for both inclusive muon and inclusive electron events. For more details, see Appendix A.

7.2 Muon Chamber Efficiency

Since muons are identified by requiring at least two layers of P-chamber and one Z-segment, any chamber inefficiency (dead P and Z cells) and reconstruction inefficiency will result in lost tracks. There are three indcpendent ways [7-1] to estimate this inefficiency.

(1) Using the database and the luminosity

One removes the dead (P and Z) cells in the Monte Carlo simulation according to the database and luminosity information for each running period. In this way, a corrected Monte Carlo is obtained and represents the real data. Figure 7-1, Figure 7-2 and Figure 7-3 show the P-chamber segment distributions before and after removing broken cells separately. The data and corrected Monte Carlo agree fairly well with each other. For the Z-chambers, after removing the bad cells, there are still discrepancies between data and corrected Monte Carlo due to the reconstruction inefficiency, which is not included in this method.

(2) Estimating the individual chamber efficiencies

This method estimates the Muon Chamber efficiency by comparing the probabilities for a muon track to be reconstructed in each chamber between data and Monte Carlo for muons in the region $|\cos\theta| \leq 0.7$. The differences between data and Monte Carlo are minimized by randomly removing a certain fraction of cells during the reconstruction of Monte Carlo events. Figure 7-4 and Figure 7-5 show the average P and Z segments per track along the track direction before and after corrections. There is a good agreement between data and Monte Carlo, it enable us to estimate the Muon Chamber efficiencies.

(3) Fitting a global efficiency

By counting the fraction of events with different number of P segments (3 or 2) and Z segments (2, 1 or 0), the global efficiencies of P and Z chambers are fitted, then determining the Muon Chamber efficiencies.

Conclusion

For muon momenta larger than 3 GeV, the Muon Chamber efficiencies are determined and the results are listed in Table 7.2, where ϵ_{all} is overall Muon Chamber efficiency. The first method only includes the dead cells, the second and third methods include all inefficiency due to reconstruction, electronics and DAQ problems as well as dead cells. The results from three independent methods agree with each other. The difference of inefficiency from these three methods gives the systematic uncertainty. It is estimated that the systematic error is less than 0.5% from comparing the results of different methods. The obtained Muon Chamber efficiency is

efficiency	Method (1)	(2)	(3)
P_{eff}	96.3 ± 0.2 %	96.6 ± 0.2 %	96.4 ± 0.3 %
Z_{eff}	99.0 ± 0.2 %	97.5 ± 0.2 %	98.3 ± 0.2 %
ϵ_{all}	95.3 ± 0.3 %	94.1 ± 0.2 %	94.8 ± 0.3 %

Table 7.2: *Estimating the efficiency of Muon Chamber by three different methods, the error is statistical only.*

(96.3±0.5)% , (98.3±0.5)% and (94.5±0.5)% for P-chamber, Z-chamber and overall respectively. The momentum dependent Muon Chamber efficiency is determined to be:

$$\epsilon_{all} = (96.0 - e^{-0.22p+1.5})\% \tag{7.1}$$

where p is the muon momentum in GeV.

7.3 Electron Detection Efficiency

The electron detection efficiency depends on the performance of the BGO and the TEC. There are about 1.5% dead and noisy BGO crystals, therefore 98.5% detection efficiency for the BGO detector. The TEC efficiency is studied from hadronic and $\tau^+\tau^-(\gamma)$ events after removing the bad runs. From the hadronic events, the TEC global efficiency is determined. The TEC global inefficiency is defined as the fraction of the hadronic events without TEC tracks. Among 12 K hadronic events, there are about 1% events which do not have TEC tracks. For the Monte Carlo events, the fraction of no TEC tracks hadronic events is less the 0.1%. Therefore the TEC global efficiency is determined to be $(99.0 \pm 0.2)\%$. From the $\tau^+\tau^-(\gamma)$ data sample, there is about 1.5% tracks with unsolved left-right ambiguity (no used inner TEC hits) and the track finding efficiency is determined to be $(96.5 \pm 1.0)\%$. For more details, see Reference [7-2]. The overall electron detection efficiency of the most effective TEC sector is $(92.7 \pm 1.5)\%$. Because some TEC sectors didn't work perfectly, the efficiency of individual sector has to be determined. Figure 7-6 shows the number of tracks and efficiency of each TEC sector from the hadronic events. The sector 12 is out of order, due to the broken wire in this sector.

Chapter 8

Heavy Quark Decay Properties

The heavy flavor properties are measured by using the inclusive lepton events. This chapter gives the description of the fitting method and results on partial decay width for b and c quarks, semileptonic branching ratio, fragmentation function and forward-backward asymmetry of the b quark.

8.1 Data Sample

The selection criteria have been discussed in early Chapter. Only muons and electrons with momentum larger than 4 GeV and 3 GeV, respectively, are used in the following analysis. Also, the momentum must be less than 30 GeV. In addition, the transverse momentum, which is measured with respect to the nearest jet with the lepton momentum excluded, is no more than 6 GeV. Table 8.1 summaries the selected number of inclusive lepton events, where the muon sample includes the 1989 and 1990 runs and electron sample contains only the 1990 runs. For dilepton events, there is no requirement on the opening angle between two leptons.

Type	$0 < p_\perp < 6\ GeV$	$1 < p_\perp < 6\ GeV$
$\mu + hadrons$	5607	2979
$e + hadrons$	1367	1085
$\mu\mu + hadrons$	248	95
$ee + hadrons$	38	26
$\mu e + hadrons$	147	78

Table 8.1: *Number of selected inclusive muon and electron events in data sample with and without lower $p_\perp$ cut. No requirement has been made for the opening angle between two leptons in the dilepton sample.*

The inclusive lepton are classified into following categories (and their charge conjugate reactions):

(1) Prompt $b \to \ell$;

(2) Cascade $b \to \tau \to \ell$;

(3) Cascade $b \to c \to \ell$;

(4) Cascade $b \to \bar{c} \to \ell$;

(5) b background, $b \to b$-hadron $\to$ background;

(6) Prompt $c \to \ell$;

(7) Decay leptons from *udsc* quarks or fragmentation process.

(8) Fake leptons from *udsc* quarks or fragmentation process.

Figure 6-12 and Figure 6-13 show the measured momentum and transverse momentum spectra for muons and electrons after the cuts. The predicted contributions from the prompt heavy quark decays, b quark only and backgrounds are indicated. The high p or high $p_\perp$ region are dominated by prompt b decays due to the hard fragmentation and large mass of the b quark. Because of the implicit isolation requirement in electron selection, the $c\bar{c}$ contribution is very small in electron sample. In muon sample, more than 90% of the $c\bar{c}$ contribution is in the range $p_\perp < 1.5\ GeV$. A large contribution comes from $b\bar{b}$ in this region, but $\Gamma_{b\bar{b}}$ and $\Gamma_{c\bar{c}}$ can be measured simultaneously by fitting over the full range of $p_\perp$. Since most of background leptons also in the low $p_\perp$ range, it is necessary to have a good understanding of the background.

For the determination of $\Gamma_{b\bar{b}}$, $Br(b \to l\nu X)$ and ϵ_b, the transverse momentum of the lepton is required to be larger than 1 GeV in order to reduce the systematic uncertainties from the background processes. By requiring $1\ GeV < p_\perp < 6\ GeV$, the muon and the electron data sample consist of 64.2% and 77.3% prompt b decays, respectively. Table 8.2 gives number of selected dilepton and single lepton events from the 1990 data sample, where the measured transverse momentum $p_\perp > 1.0\ GeV$ and the opening angle between two leptons must be larger than 60° for inclusive dilepton events. Because the endcap of Veto Counters was installed in 1990 at the

Data type	Number of events dilepton	Number of events single lepton
μ only	65	2717
e only	18	1172
$\mu + e$	138	3711

Table 8.2: *Number of selected inclusive muon and electron events in the 1990 data sample with a $p_\perp$ cut of 1 GeV, where the opening angle between two leptons is required to be larger than 60° in dilepton data sample.*

L3 detector, the 1989 data are not used to measure the $\Gamma_{b\bar{b}}$, $Br(b \to l\nu X)$ and ϵ_b for the same reason.

8.2 Fitting Method

An event by event unbinned maximum likelihood fit is performed to determine the heavy quark properties and mixing parameter χ_B by fitting to the p and $p_\perp$ spectra for single lepton and dileptons events observed in hadronic decays of the Z^0. The value χ_B is extracted from a fit to the dilepton p and $p_\perp$ distributions in the data. To calculate the probability that data events contain two $b \to \ell$ decays, the following fully simulated Monte Carlo events are used: Lund $udscb$ events, b-flavor events and special b-flavor events, where one of the b quark is forced to semileptonicly decay into μ *or* e. Also, special b-flavor events without detector simulation are used, where the events are smeared to take into account detector effects. The Monte Carlo events have been normalized using the L3 measurement of the Z^0 hadronic partial width, $\Gamma_{had} = 1742 \pm 19\ MeV$ [8-1].

The likelihood function is defined as the joint probability density,

$$L = \prod_{i=1}^{N} f(i) \qquad f(i) = \frac{1}{N}\frac{dN}{dV}\Big|_i \tag{8.1}$$

where $f(i)$ is the probability density and dN is the number of events found in area or volume dV at the point i. For single lepton events, the likelihood function is determined from the number and type of Monte Carlo leptons found within a rectangular box centered on each data lepton in the $p - p_\perp$ plane. While for dilepton events, the likelihood function is determined from the number and type of Monte Carlo leptons found within a four dimension box centered on each data point in the $(p_1, p_{\perp 1}, p_2, p_{\perp 2})$ space. The size of the box is allowed to increase until a minimum number of Monte Carlo leptons are included inside the box. For measurement of heavy flavor partial width, b quark semileptonic decay branching ratio and fragmentation function, a minimum of 20 Monte Carlo leptons in the box is required. And to determine the $b\bar{b}$ forward-backward asymmetry and mixing parameter χ_B (dilepton only), a minimum number of Monte Carlo leptons is 40. Assuming that N_{D1} and N_{D2}, the observed number of single lepton and dilepton events respectively, are distributed according to Poisson statistic with mean values N_{M1} and N_{M2}. One finds the likelihood function (L) for single lepton events:

$$L = \frac{(N_{M1})^{N_{D1}} \cdot e^{-N_{M1}}}{N_{D1}!} \prod_{i=1}^{N_{D1}} \frac{1}{N_{M1} V_{box}(i)} \sum_k N_k(i) W_k(i) \tag{8.2}$$

The likelihood function (L) for dilepton events has the form:

$$L = \frac{(N_{M2})^{N_{D2}} \cdot e^{-N_{M2}}}{N_{D2}!} \prod_{i=1}^{N_{D2}} \frac{1}{N_{M2} V_{box}(i)} \sum_{k,l} N_{k,l}(i) W_{k,l}(i) \tag{8.3}$$

where $W_k(i)$ and $W_{k,l}(i)$ are the weighting function, which depend on the fitting variables, as will be discussed later in the analysis. The expected number of events N_{M1} and N_{M2} are determined by Monte Carlo calculation and indices k, l indicate the category of the lepton source type. $N_k(i)$ and $N_{k,l}(i)$ are the number of simulated

Monte Carlo lepton events of this category found in the box with data lepton i, and $V_{box}(i)$ is the area (volume) of the box.

MINUIT [8-2] is used to minimize the log likelihood function -log(L). When N_{D1} is large, $N_{D1} \gg 1$, the log likelihood function for single lepton can be expressed:

$$\log(L) \simeq \log[\prod_{i=1}^{N_{D1}} \frac{1}{N_{M1} V_{box}(i)} \sum_k N_k(i) W_k(i)] - 0.5 \cdot \frac{(N_{D1} - N_{M1})^2}{N_{D1}} + constant \quad (8.4)$$

This is a good approximation, it is also true for dilepton events. For detailed information about likelihood functions, see reference [8-3].

8.3 General Remarks

The expected partial Z^0 decay width into heavy quarks in the Standard Model is $\Gamma_{b\bar{b}} = 378\ MeV$ and $\Gamma_{c\bar{c}} = 297\ MeV$. These values are used in the analysis. In the fit, the Monte Carlo events are weighted such that the $x_E = 2E_{hadron}/\sqrt{s}$ distributions for b and c quark fragmentation follow a Peterson *et al.* function with a parameter ϵ_b *and* ϵ_c, where the E_{hadron} is the energy of the first-rank hadron. The measured ϵ_b ($\epsilon_b = 0.050 \pm 0.004$) is used in the determination of heavy quark properties. For the c quark fragmentation, $\epsilon_c = 0.5$ is used. This value agrees with extrapolations from PETRA and PEP [8-4].

The average c hadron semileptonic branching ratio, from measurements at PETRA and PEP [8-5], is used: $Br(c \rightarrow l\nu X) = 0.096 \pm 0.006$. This branching ratio is an average over the production and semileptonic decay of c hadrons in the c quark hadronization.

Evidence for the heavy charmed mesons D^{**} was presented by the CLEO experiment [8-6]. The standard Monte Carlo, JETSET 7.2, produces only D and D^* states of charmed mesons in its simulation of b semileptonic decays, while it does not incorporate the D^{**} which are the higher mass states. The semileptonic decay of b hadrons into a massive hadronic state obviously produces a softer leptonic spectrum. Also, any non-resonant $D\pi\pi$ or $D^*\pi$ production in the b semileptonic decay would have a similar effect, and is also not included in the standard Monte Carlo simulation. The actual D^{**} content has not been determined so far. Only widely varying estimates are available. A theoretical estimate in the IGSW model [8-7] has set the relative fraction of D^{**} in b quark semileptonic decay to approximately 10%. However, experimental results from the $\Upsilon(4S)$ [8-6] give values in the range 0.2 to 0.3, with large errors. Of course, the fraction could be different for b hadrons coming from Z^0 decays.

The additional higher mass D meson states in b semileptonic decays will change the predicted shape of the prompt-lepton momentum and transverse momentum spectrum and thus affects the result. To study the effect, events with the decay $b \rightarrow D_2^*(2460) + l\nu$ have been simulated and the distribution of $p - p_\perp$ is produced. By combining certain fractions of pure $b \rightarrow D_2^*(2460) + l\nu$ events with normal Monte Carlo events, a new p and $p_\perp$ distribution is obtained. Every normal Monte Carlo event is weighted according to its p and $p_\perp$, and the data is fitted to this new Monte

Carlo sample. In this analysis, a branching ratio of 15% for b decay into $D_2^*(2460)$ is used, in agreement with the IGSW model and the experimental results. Introducing 15% of higher mass D meson states in the b semileptonic decays increases the measured values of $\Gamma_{b\bar{b}}$ by 7 MeV, $Br(b \to l\nu X)$ by 0.002, ϵ_b by less than 0.001, $A_{b\bar{b}}$ by less than 0.001 and χ_B by -0.0004, respectively. A simple detector simulation has been done from the Monte Carlo generator. Adding 15% D^{**} in b semileptonic decays reduces the acceptance of $b \to \ell$ by 2.7%. This agrees with the previous estimation. The fitted values are corrected by these amounts. Therefor, all the results in this analysis correspond to 15% $D_2^*(2460)$ in b semileptonic decays. And the systematical uncertainty due to D^{**} is estimated by varying this branching ratio by $\pm 15\%$.

The effect of higher mass B meson production has been investigated using a similar method. Though the relative production of B^* and B mesons is not known very well, it has an insignificant effect on the analysis results because the measured mass difference between B^* and B mesons is small, $52 \pm 2 \pm 4$ MeV [8-8]. This is verified by changing the relative production of B^* and B mesons in Monte Carlo simulation. Varying the ratio of the number of B^* to B mesons from 2 to 4 changes results by less than 0.3% (In the standard Monte Carlo, this ratio is three). The standard Monte Carlo does not include the B^{**} production in the b hadronization. The events with B^{**} meson has been generated to investigate its effect on the analysis results, where $M_{B^{**}} - M_{B^*} = 500$ MeV. Adding 10% of B^{**} mesons in b quark fragmentation process changes the results by less than 0.5%. It is a negligible effect.

The muon energy loss in the calorimeter is investigated from the dimuon sample ($e^+e^- \to \mu^+\mu^-$). It has been observed that the Monte Carlo deposits on average 0.36 GeV too much energy along the muon direction. This systematically pulls the jet direction closer to the muon direction, thus it lowers the $p_\perp$ value in the Monte Carlo and changes the fit results. The effect was investigated by subtracting 0.36 GeV jet energy along the muon direction in the Monte Carlo. This changes $\Gamma_{b\bar{b}}$ by -7 MeV, $Br(b \to \mu\nu X)$ by -0.002, ϵ_b by -0.003, $A_{b\bar{b}}$ by 0.003 and χ_B by 0.004. These numbers will be quoted as the systematical uncertainties. From the $e^+e^- \to$ *hadrons* sample, the jet angular resolution has been studied by using the acollinearity ξ between two most energetic jets. The average ξ of the Monte Carlo is 1° higher than the value in the data. Thus the jet direction (θ, ϕ) is not perfectly simulated in the Monte Carlo. The acoplanarity $\Delta\phi = |\pi - (\phi_1 - \phi_2)|$, where $\phi_1 > \phi_2$, and $\Delta\theta = |\pi - (\theta_1 - \theta_2)|$ are compared between data and Monte Carlo. The average $\Delta\phi$ and $\Delta\theta$ in the Monte Carlo are 1.2° and 0.1° higher than the ones in the data. To correct for this difference, the θ and ϕ of jets are smeared in the Monte Carlo by 0.06° and 0.86° respectively with a normal Gaussian distribution. This changes the analysis results by 0.5%, for instance, $\Gamma_{b\bar{b}}$ decreases by 2 MeV. Thus the effect is small. The systematic error due to jet angular resolution is strongly correlated with the systematic uncertainly due to the lepton $p_\perp$ resolution. In this analysis, the uncertainty due to the $p_\perp$ resolution is quoted as a systematic error.

8.4 B Semileptonic Branching Ratio

The semileptonic branching ratio of b hadrons is determined using two methods. First, the double tag method is used to measure the b semileptonic branching ratio $Br(b \to l\nu X)$, where the statistical error is dominated by the number of dilepton events. For dilepton events, except for the standard cuts, there is an additional requirement that the opening angle between two leptons be larger than 60°. In the second method, a one-parameter fit is performed to determine the $Br(b \to l\nu X)$ with $\Gamma_{b\bar{b}}$ set to the Standard Model value of 378 MeV. This method uses mainly the rate of single lepton events and gives therefore a smaller statistical errors than the double tag method.

8.4.1 Double Tag Method

From the ratio R of the accepted number of dileptons events to single leptons events, the b semileptonic branching ratio can be measured. In the first order, this ratio is proportional to $Br(b \to l\nu X)$ and independent of $\Gamma_{b\bar{b}}$. Let's look at a simple example and suppose that all leptons are from b semileptonic decays, that means the number of single lepton events (N_{D1}) is proportional to $2B(1-B)$ and number of dilepton events (N_{D2}) is proportional to B^2, where B is the b semileptonic branching ratio $Br(b \to l\nu X)$. Therefore,

$$R = \frac{N_{D2}}{N_{D1}} = \frac{B}{2(1-B)} \tag{8.5}$$

Then the b semileptonic branching ratio and its relative error are given by:

$$B = \frac{2R}{1+2R} \tag{8.6}$$

$$\frac{\Delta B}{B} = \frac{1}{1+2R}\frac{\Delta R}{R} \approx \frac{1}{1+2R}\frac{\sqrt{N_{D2}}}{N_{D2}} \tag{8.7}$$

The relative error of the branching ratio is smaller than the relative statistical error of the number of dileptons by a factor $1+2R$.

In real life, the situation is not so simple and background processes exist. The events are divided into four categories.

(1) Events with $b \to \ell, b \to \ell$

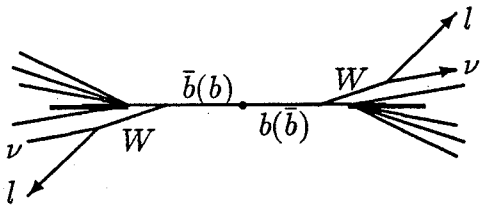

(2) Events with one $b \to \ell$

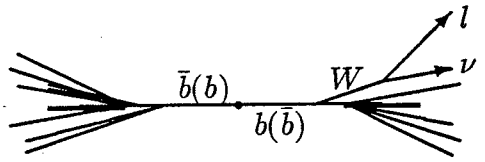

(3) Events with no $b \to \ell$

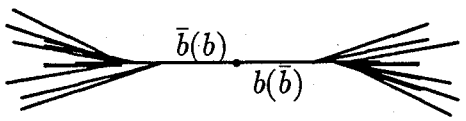

(4) Events from udsc

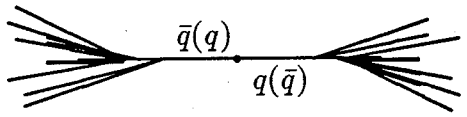

The first two categories are the signal, while the remaining two are backgrounds, where the leptons are not directly produced in b semileptonic decays. By requiring $p_\perp > 1.0\ GeV$, most of the background leptons are cut away. The ratio of the number dilepton events to the number of single lepton events is:

$$\frac{N_{D2}}{N_{D1}} = \frac{b_1 B^2 + 2b_2 B(1-B) + b_3(1-B)^2 + b_4(\Gamma_{had}/\Gamma_{b\bar{b}} - 1)}{a_1 B^2 + 2a_2 B(1-B) + a_3(1-B)^2 + a_4(\Gamma_{had}/\Gamma_{b\bar{b}} - 1)} \tag{8.8}$$

and the various terms represent events with leptons from $b \to \ell, b \to \ell$; one and only one from $b \to \ell$; no lepton from prompt b decay, and the last term gives the contribution from lighter quark production. The coefficients a_i and b_i are the acceptances, which are determined from Monte Carlo simulation. Typical acceptances are listed in Table 8.3, without the D^{**} contributions. This method for measuring

Acceptance	μ only	e only	$\mu + e$
a_1	0.36765	0.27033	0.33427
a_2	0.33740	0.17674	0.26041
a_3	0.01656	0.00554	0.02321
a_4	0.00643	0.00169	0.00809
b_1	0.13812	0.03861	0.08364
b_2	0.00384	0.00068	0.00364
b_3	0.00005	0.00002	0.00019
b_4	0.00003	0.00000	0.00004

Table 8.3: *Various acceptances for single and dilepton events, for* $p_\perp > 1\ GeV$. *The opening angle between two leptons must be larger than* 60°.

b semileptonic branching ratio has been cross-checked with the Monte Carlo events. Several input value has been used in the Monte Carlo, the determined values of $Br(b \to l\nu X)$ agree very well with the Monte Carlo input values of $Br(b \to l\nu X)$.

Using the measured ratio of the number of dilepton events to the number of single lepton events and Equation 8.8, one can solve for the b semileptonic branching ratio. The results are found to be:

$$Br(b \to \mu\nu X) = 0.112 \pm 0.012 \tag{8.9}$$

$$Br(b \to e\nu X) = 0.136 \pm 0.031 \tag{8.10}$$

where the errors are statistical only. In the standard Monte Carlo the $Br(b \to l\nu X)$ is 11.2%. By changing this value by 10.0%, i.e., $Br(b \to l\nu X)$ from 10.2% to 12.2%, the acceptances vary more than 20%, but the difference of the measured $Br(b \to l\nu X)$ is within 0.1%. Thus the measured $Br(b \to l\nu X)$ does not depend on the $Br(b \to l\nu X)$ assumed in the Monte Carlo. Also, if the $p_\perp$ cut is varied from 1 GeV to 2 GeV, all the results agree within the statistical error.

Systematic errors have been studied by varying different parameters. The variations correspond to at least one standard deviation changes using the known or estimated errors. The systematic error for each parameter is summaried as follows:

- The measured $Br(b \to l\nu X)$ has weak correlation with $\Gamma_{b\bar{b}}$. Varying $\Gamma_{b\bar{b}}$ by $\pm 40\ MeV$ around the Standard Model prediction ($\Gamma_{b\bar{b}} = 378\ MeV$) results in changes of $\pm 0.2\%$ in the b semileptonic branching ratio. Figure 8-1(a) shows the $Br(b \to l\nu X)$ by changing $\Gamma_{b\bar{b}}$ from 300 MeV to 460 MeV.

- The b quark fragmentation affects the lepton momentum, hence the acceptances. Varying the Peterson function around the measured ϵ_b by $\pm(0.010)$ gives a difference of $\pm 0.3\%$ in $Br(b \to l\nu X)$.

- $Br(b \to l\nu X)$ changes less than 0.05% by varying the ϵ_c parameter in the c quark Peterson function ϵ_c from 0.40 to 0.60. The effect of the c quark fragmentation is negligible.

- The world average c semileptonic branching ratio is 0.096 ± 0.006. Varying $Br(c \to l\nu X)$ by ± 0.006 results in a change of $Br(b \to l\nu X)$ by $\pm 0.2\%$ for muons and $\pm 0.1\%$ for electrons. Also, $\Gamma_{c\bar{c}}$ has been varied by $\pm 7\ MeV$ around the Standard Model prediction of 297 MeV, the effect is smaller than 0.1%.

- The uncertainty due to the background is estimated by varying the fraction of background by $\pm 10\%$, which gives $\pm 0.1\%$ change in branching ratio.

- The efficiencies in the selection of muons and electrons are determined with errors 0.5% and 3.0% respectively. These changes $Br(b \to \mu\nu X)$ by $\pm 0.1\%$ and $Br(b \to e\nu X)$ by $\pm 0.6\%$. The selection efficiency error is larger for electrons due to uncertainties in identifying electron in a hadronic event and in matching BGO clusters with tracks in the central tracking chamber.

- The lepton transverse momentum is calculated with respect to the nearest jet axis. Its resolution is not known very well. Smearing $\Delta p_\perp / p_\perp$ by 20% changes the branching ratio by 0.2% for muons and by 0.4% for electrons.

- By smearing the lepton momentum by 10% to see the effect on branching ratio, one finds that $Br(b \to l\nu X)$ changes less than 0.1%.

- The 0.36 GeV disagreement of the muon energy loss in the calorimeter between data and Monte Carlo decreases $Br(b \to \mu\nu X)$ by 0.2% for muon.

- The systematic effect of the production D^{**} in b semileptonic decays is estimated by varying the fraction of $B \to D^{**} + l\nu$ by $\pm 15\%$. The $Br(b \to l\nu X)$ changes by $\pm 0.2\%$.

Figure 8-1 shows four examples of how systematic errors have been determined. Added in quadrature, the combined systematic errors are $\pm 0.6\%$ for muons and $\pm 0.8\%$ for electrons.

The average b semileptonic branching ratio is determined by combing the muon and electron events. The statistics is higher because of additional μe events. The measured value is:

$$Br(b \to l\nu X) = 0.111 \pm 0.010(stat) \pm 0.006(sys) \tag{8.11}$$

The measurements agree with the average b semileptonic branching ratio measured at PETRA and PEP [8-5] [8-9]: $Br(b \to \mu\nu X) = 0.117 \pm 0.010$ and $Br(b \to e\nu X) = 0.121 \pm 0.010$. The PETRA and PEP values have been measured at lower center-of-mass energies where the electroweak effects contribution less than 3% to the $e^+e^- \to b\bar{b}$ cross section. The $Br(b \to l\nu X)$ from the double tagging method depends only weakly on $\Gamma_{b\bar{b}}$. Averaging our measured value with the measurements from PETRA and PEP, one gets:

$$Br(b \to l\nu X) = 0.117 \pm 0.006 \tag{8.12}$$

where the statistical and systematic errors have been added in quadrature. This average is nearly free from the assumptions about the neutral current couplings to b quark. This averaged b semileptonic branching ratio will be used to determine $\Gamma_{b\bar{b}}$, the b fragmentation function parameter, $A_{b\bar{b}}$ and χ_B in the following analysis.

8.4.2 Determination of $Br(b \to l\nu X)$ from the fit

Parameter	Variation	$\Delta Br(b \to e\nu X)$	$\Delta Br(b \to \mu\nu X)$
$\Gamma_{b\bar{b}} = 378\ MeV$	$\pm 3\ MeV$	± 0.001	± 0.001
ϵ_b=0.050	± 0.010	± 0.003	± 0.003
$Br(c \to l\nu X) = 0.096$	± 0.006	± 0.001	± 0.002
$\Gamma_{c\bar{c}} = 297\ MeV$	$\pm 7\ MeV$	< 0.001	< 0.001
ϵ_c=0.5	± 0.1	< 0.001	< 0.001
background	$\pm 10\%$	± 0.001	± 0.001
selection efficiencies (μ)	$\pm 0.5\%$	—	± 0.001
selection efficiencies (e)	$\pm 3\%$	± 0.006	—
$\Delta p_\perp/p_\perp$ smearing	20%	± 0.004	± 0.002
$\Delta p/p$ smearing	10%	—	< 0.001
D^{**} fraction = 0.15	± 0.15	± 0.002	± 0.002
muon dE/dX	$0.36\ GeV$	—	-0.002
systematic error	—	± 0.008	± 0.006

Table 8.4: *Contributions to the systematic error in the measurement of* $Br(b \to e\nu X)$ *and* $Br(b \to \mu\nu X)$ *from the fit*

In the second method, the branching ratio $Br(b \to l\nu X)$ is determined from a one-parameter unbinned maximum likelihood fit. Basically, this method is based on the number of inclusive lepton events. The Monte Carlo events are weighted according to their categories. If only one lepton is from the prompt b decay, the event is weighted by $B/0.112$ (where 11.2% is the b semileptonic branching ratio in the Monte Carlo), otherwise it is weighted by 1. If there are two leptons from prompt b decays, the event is weighted by $(B/0.112)^2$. Also, this event has a probability $2(B/0.112)(1 - B/0.112)$ to become a single lepton event.

The results of the fit are:

$$Br(b \to \mu\nu X) = 0.123 \pm 0.003(stat) \pm 0.006(sys) \tag{8.13}$$

$$Br(b \to e\nu X) = 0.112 \pm 0.004(stat) \pm 0.008(sys) \quad (8.14)$$

Similarly as in the first method, the systematic errors are determined by varying the parameters shown in Table 8.4, where $\Gamma_{b\bar{b}}$ is altered by $\pm 3\ MeV$ the estimated error on Standard Model prediction. It corresponds to a variation of M_Z and α_s within measured errors and of the top quark and the Higgs mass in the ranges, $90\ GeV < M_{top} < 250\ GeV$ and $50\ GeV < M_{Higgs} < 1000\ GeV$. The fit is also performed with different $p_\perp$ cut. All results agree well.

From the studies, the systematic uncertainties of the b semileptonic branching ratio are found to be 0.006 for muons and 0.008 for electrons. From a combined fit to the muon and electron data, the b semileptonic branching ratio is measured as:

$$Br(b \to l\nu X) = 0.119 \pm 0.003(stat) \pm 0.006(sys) \quad (8.15)$$

8.5 Partial Width of Z^0 Decays

Parameter	Variation	electrons $\Delta\Gamma_{b\bar{b}}\ (MeV)$	muons $\Delta\Gamma_{b\bar{b}}\ (MeV)$
$Br(b \to l\nu X) = 0.117$	± 0.006	± 19	± 19
$\epsilon_b = 0.050$	± 0.010	± 4	± 6
$Br(c \to l\nu X) = 0.096$	± 0.006	± 2	± 3
$\Gamma_{c\bar{c}} = 297\ MeV$	$\pm 7\ MeV$	± 1	± 1
ϵ_c=0.5	± 0.1	± 1	± 1
background	$\pm 10\%$	± 5	± 7
selection efficiencies (μ)	$\pm 0.5\%$	—	± 2
selection efficiencies (e)	$\pm 3\%$	± 11	—
$\Delta p_\perp/p_\perp$ smearing	20%	± 9	± 8
$\Delta p/p$ smearing	10%	—	± 2
D^{**} fraction = 0.15	± 0.15	± 7	± 7
muon dE/dX	$0.36\ GeV$	—	-7

Table 8.5: *Contributions to the systematic error in the measurement of* $\Gamma_{b\bar{b}}$.

In the fitting method, $\Gamma_{b\bar{b}}$ is determined by fitting the observed $p - p_\perp$ spectrum for leptons to a combination of the $p - p_\perp$ distributions for each of sources of lepton, with $\Gamma_{b\bar{b}}$ as free parameter and all other parameters fixed to their nominal values. The b events are weight by $\Gamma_{b\bar{b}}/\Gamma^0_{b\bar{b}}$, others by 1. The obtained values are:

$$\Gamma_{b\bar{b}} = 396 \pm 9\ \ MeV\ (\mu\nu + X) \quad (8.16)$$

$$\Gamma_{b\bar{b}} = 370 \pm 12\ MeV\ (e\nu + X) \quad (8.17)$$

for muons and electrons, respectively. The errors are statistical only. The systematic errors are estimated by varying parameters by at least one standard deviation of their known or estimated uncertainties. The various systematic errors are shown

in Table 8.5. The fit is performed by using different $p_\perp$ cut, from 0 GeV up to 1.25 GeV, all results agree well within the statistical error.

The systematic errors of $\Gamma_{b\bar{b}}$ are 19 MeV both for muons and electrons from the uncertainty of b semileptonic branching ratio, $Br(b \to l\nu X)$, and $\Delta\Gamma_{b\bar{b}} = 16\ MeV$ for muons and $\Delta\Gamma_{b\bar{b}} = 17\ MeV$ for electrons from other sources. A combined fit using the inclusive muon and electron samples has been performed. The result is:

$$\Gamma_{b\bar{b}} = 385 \pm 7(stat) \pm 15(sys) \pm 19(Br)\ MeV \tag{8.18}$$

As an additional check, $\Gamma_{b\bar{b}}$ is extracted by counting the number of accepted inclusive events. Similar as in Equation 8.8, the number of accepted inclusive lepton events $N_{D1} + N_{D2}$ is:

$$N_{D1} + N_{D2} = N_{had}\frac{\Gamma_{b\bar{b}}}{\Gamma_{had}}[c_1 B^2 + 2c_2 B(1-B) + c_3(1-B)^2 + c_4(\Gamma_{had}/\Gamma_{b\bar{b}} - 1)] \tag{8.19}$$

with $c_i = a_i + b_i$. One can solve for $\Gamma_{b\bar{b}}$ by using the b semileptonic branching ratio $Br(b \to l\nu X) = 0.117$ and finds:

$$\Gamma_{b\bar{b}} = 378 \pm 10\ MeV \tag{8.20}$$

where the error is statistical only, including Monte Carlo statistics. The result is in good agreement with the value from fit.

Adding all the errors (see equation 8.18) in quadrature one get:

$$\Gamma_{b\bar{b}} = 385 \pm 25\ MeV \tag{8.21}$$

The measurement is in good agreement with the Standard Model prediction of $\Gamma_{b\bar{b}} = 378 \pm 3\ MeV$.

The partial decay width $\Gamma_{c\bar{c}}$ is extracted from a two-parameter fit to the data, where $\Gamma_{b\bar{b}}$ and $\Gamma_{c\bar{c}}$ are simultaneously determined. Since the $c\bar{c}$ contribution is small in the electron sample due to the implicit $p_\perp$ cut, only muon data is used. The correlation coefficient between the parameters is -55%. The results of the fit are:

$$\Gamma_{b\bar{b}} = 396 \pm 10\ MeV \tag{8.22}$$

$$\Gamma_{c\bar{c}} = 296 \pm 24\ MeV \tag{8.23}$$

where the errors are statistical only. The systematic error of $\Gamma_{c\bar{c}}$ is about 36 MeV. The measured $\Gamma_{c\bar{c}}$ agrees with the Standard Model prediction ($297 \pm 7\ MeV$).

8.6 b Quark Fragmentation

It is necessary to study the fragmentation function for b quarks in order to measure b quark properties accurately, since the momentum distribution of the observed lepton is directly related to the b hadron spectrum prior to decay. In the Monte Carlo, the b quarks were fragmented according to the Peterson *et al.* functional form, where the shape of the fragmentation function depends on the single parameter ϵ_b.

The fragmentation function of b quark is characterized in term of the scaled energy $x_E = 2E_{hadron}/\sqrt{s}$, and E_{hadron} is the energy of the first-rank hadron.

As before, the fitting method is used to determine the fragmentation function of b quarks from Z^0 decays with two different assumptions about the x_E distribution. In the first method, the b quark fragmentation function is determined from data without assumptions on a functional form of the x_E distribution. Instead of using a functional form, the x_E distribution is approximated by a histogram with 7 bins, and the value for each bin is allowed to vary freely in the fit. The fit is performed in the allowed range $x_E \geq \frac{2M_B}{\sqrt{s}}$, and is constrained to enforce a overall normalization of the fragmentation function. With all other parameters fixed to their nominal values, a six-parameter fit (the value of the seventh bin is constrained by normalization) is performed to determine the x_E distribution and average x_E. Only the inclusive muon sample is used in this analysis. Figure 8-2 shows the result of the fit. The points with error bars (statistical only) give the result of the fit. The data points give an average $<x_E> = 0.680 \pm 0.011$, where the error is statistical only and includes correlations between all points. This method also checks whether the Peterson *et al.* function gives a proper and suitable description of the x_E distribution. For comparison, the Peterson *et al.* function for $\epsilon_b = 0.50$ (the measured value given later) is shown in Figure 8-2 too. Within errors the measured x_E distribution is well described by a Peterson *et al.* function. The fits have been repeated using 5 and 6 bins for the fragmentation function. The distributions agree with the 7 bin result. The average energy fractions, $<x_E>$, agree within the statistical errors.

Parameter	Variation	$\Delta\epsilon_b$	$\Delta<x_E>$
$\Gamma_{b\bar{b}} = 378\ MeV$	$\pm 10\ MeV$	± 0.002	± 0.003
$Br(b \to l\nu X) = 0.117$	± 0.010	± 0.006	± 0.010
$Br(c \to l\nu X) = 0.096$	± 0.006	± 0.002	± 0.003
$\Gamma_{c\bar{c}} = 297\ MeV$	$\pm 7\ MeV$	< 0.001	< 0.001
$\epsilon_c = 0.5$	± 0.1	< 0.001	< 0.001
background	$\pm 10\%$	± 0.001	± 0.0015
selection efficiencies (μ)	$\pm 0.5\%$	< 0.001	< 0.001
selection efficiencies (e)	$\pm 3\%$	± 0.002	± 0.003
$\Delta p_\perp/p_\perp$ smearing	20%	± 0.009	± 0.015
$\Delta p/p$ smearing	10%	± 0.002	± 0.003
D^{**} fraction = 0.15	± 0.15	< 0.001	< 0.001
muon dE/dX	$0.36\ GeV$	-0.003	$+0.005$
systematic error	—	± 0.012	± 0.020

Table 8.6: *Contributions to the systematic error in the measurement of* ϵ_b *and* x_E.

The agreement of the measured fragmentation function with the Peterson *et al.* function justifies to express the x_E distribution by a Peterson *et al.* function. Therefore, in the second method, the fragmentation properties of b quarks are measured by fitting ϵ_b. The parameter ϵ_b is fitted to the measured lepton p and $p_\perp$ spectra, with all other parameters fixed to their nominal values. In the fit, the ϵ_b is varied

and the Monte Carlo events are weighted accordingly by using a Peterson *et al.* function based on its x_E. The following results are obtained:

$$\epsilon_b = 0.047 \pm 0.005 \quad for\ (\mu\nu + X) \tag{8.24}$$

$$\epsilon_b = 0.056 \pm 0.008 \quad for\ (e\nu + X) \tag{8.25}$$

where the errors are statistical only. Also, if the fit is performed in a different $p_\perp$ range, all the differences are within the statistical error. The results are verified by changing various parameters with at least one standard deviation of their known or estimated uncertainties (see Table 8.6). The systematic error is estimated from this studies.

The systematic errors are estimated to be 0.012 in ϵ_b and 0.020 in x_E, both for the muon and the electron measurement. The systematic uncertainty due to the different fragmentation models has not been considered. The fit, which is performed by using muon and electron data, gives the result:

$$\epsilon_b = 0.050 \pm 0.004(stat) \pm 0.012(sys) \tag{8.26}$$

and a precise determination of the $<x_E>$, the average fractional energy of b hadron from the b quark fragmentation.

$$<x_E> = 0.686 \pm 0.006(stat) \pm 0.020(sys) \tag{8.27}$$

8.7 $b\bar{b}$ Forward-Backward Asymmetry

In a semileptonic decay of b (or $\bar{b}$) quark, the charge of the detected leptons directly correlated with the charge of the original b (or $\bar{b}$) quark. The direction of the thrust axis of the event is used to define the direction of the original b quarks, Monte Carlo studies show that this axis best represents the direction of the primary b quark at production. And the sign of the quark charge is given according to the sign of the lepton charge ($b \to l^-$, $\bar{b} \to l^+$). In this way, the $b\bar{b}$ forward-backward asymmetry ($A_{b\bar{b}}$) can be measured. The same fitting method is used to measure this asymmetry. Rather than using only the data with a high $p_\perp$ cut, the full data sample (without $p_\perp$ cut) is used to determine $A_{b\bar{b}}$ in order to increase the statistics and sensitivity to $b \to \ell$ events. A high p and high $p_\perp$ event is given a relative high weight because an event with a prompt b decay lepton is sensitive to the $A_{b\bar{b}}$. The data obtained in 1989 is used in the analysis too. Electron tracks are excluded in the lower resolution regions adjacent to the anode and cathode planes to avoid wrong charge measurement. In addition, E_9/E_{25} is required to be larger than 0.95 for the data to reject misidentified hadrons. The number of selected events is 6002, 1269 and 7141 for inclusive muon, inclusive electron and for the combined data sample respectively.

For single lepton events, the likelihood function is the same as in Equation 8.2, which is:

$$L = \frac{(N_{M1})^{N_{D1}} \cdot e^{-N_{M1}}}{N_{D1}!} \prod_{i=1}^{N_{D1}} \frac{1}{N_{M1} V_{box}(i)} \sum_k N_k(i) W_k(i) \tag{8.28}$$

where $W_k(i)$ is the weighting function and has to be determined. The angular distribution for $e^+e^- \to Z^0 \to q\bar{q}$ is:

$$\frac{d\sigma}{d\Omega} \propto \frac{3}{8}(1+\cos^2\theta) + A_k \cos\theta \tag{8.29}$$

where θ is the polar angle of the primary quark production with respect to the outgoing electron beam direction. In reality, the thrust axis of data event is chosen to point along the primary b quark production direction, as indicated by the lepton charge (Q_i).

$$\cos\theta_i = -Q_i \cos(\theta_{thrust}) \tag{8.30}$$

where the thrust axis (two possibilities) is chosen to be closer in angle to the lepton direction, i.e, the opening angle between the thrust direction and the lepton direction is less than 90°. Because the lepton p and $p_\perp$ do not depend on the primary quark direction and only the relative weight is important in the fit, the weighting function $W_k(i)$ is chosen as:

$$W_k(i) = \frac{3}{8}(1+\cos^2\theta_i) + A_k \cos\theta_i \tag{8.31}$$

where the A_k is the asymmetry for different sources. The various asymmetries are

(1) $A_1 = A_{b\bar{b}}$ for $b \to \ell$

(2) $A_2 = A_{b\bar{b}}$ for $b \to \tau \to \ell$

(3) $A_3 = -A_{b\bar{b}}$ for $b \to c \to \ell$

(4) $A_4 = A_{b\bar{b}}$ for $b \to \bar{c} \to \ell$

(5) $A_5 = 0.70A_{b\bar{b}}$ for $b \to b$-hadron $\to$ background

(6) $A_6 = -A_{c\bar{c}}$ for $c \to \ell$

(7) $A_7 = A_{back}$ for decay leptons from $udsc$ quarks and $b\bar{b}$ fragmentation

(8) $A_8 = A_{back}$ for fake leptons from $udsc$ quarks and $b\bar{b}$ fragmentation

For the background arises from b hadron decays, it is observed that 85% of the lepton candidates have the same charge sign as the primary b quark, so the effective asymmetry is $(1 - 2 \cdot 0.15)A_{b\bar{b}} = 0.7A_{b\bar{b}}$. The forward-backward asymmetry for primary charm quarks is related to the b quark asymmetry in the Standard Model through the neutral coupling constants. In this fit, the $A_{c\bar{c}}$ is fixed as a fraction of the $A_{b\bar{b}}$, $A_{c\bar{c}} = 0.7A_{b\bar{b}}$. The background asymmetry is set to be zero ($A_{back} = 0$).

For the dilepton events, the fitting procedure is similar, except that the fit is done in four dimensional space. The likelihood function is shown in Equation 8.3. The weighting function is the average weight (see Equation 8.31) of two leptons. For more discussion on the dilepton weighting function including mixing parameters, see the analysis about the B^0-$\bar{B}^0$ mixing.

A one-parameter fit is performed to fit the p and $p_\perp$ distributions for inclusive muon and electron data separately, with $A_{b\bar{b}}$ as a free parameter and all others fixed to their nominal values. Without assuming mixing, the observed $b\bar{b}$ forward-backward asymmetry is:

$$A_{b\bar{b}}^{obs} = 0.101 \pm 0.028 \quad for\ (\mu\nu + X) \tag{8.32}$$

$$A_{b\bar{b}}^{obs} = 0.026 \pm 0.044 \quad for\ (e\nu + X) \tag{8.33}$$

where the error is statistical only. A fit on combined muon and electron data gives the result:

$$A_{b\bar{b}}^{obs} = 0.082 \pm 0.024 \tag{8.34}$$

where the error is statistical only. The fits have been performed at different $p_\perp$ cut, from 0 GeV up to 1.5 GeV, all the results agree within the statistical error.

The forward-backward asymmetry varies as a function of center-of-mass energy. In this measurement, the entire data sample is used to determine $A_{b\bar{b}}^{obs}$. By considering the effects of initial state radiative corrections [8-10], the weighted average center-of-mass energy corresponding to the data sample is 91.28 GeV. The $b\bar{b}$ forward-backward asymmetry has been analyzed separately at each of the three energy points, below, on, and above the Z^0 peak. The results of the fits are displayed in Table 8.7 for the muon and for the combined channel (muon + electron), where the errors are statistical only and mixing parameter is set to zero. The off-peak

Mean Energy (GeV)	μ only $A_{b\bar{b}}^{obs}$	$\mu + e$ $A_{b\bar{b}}^{obs}$
89.63	0.109 ± 0.057	0.26 ± 0.13
91.28	0.058 ± 0.028	0.081 ± 0.031
93.03	0.066 ± 0.047	0.159 ± 0.071

Table 8.7: *Measured asymmetries for different center-of-mass*

electron data sample is still too small to yield a statistically worthwhile measurement.

Table 8.8 lists the major contributions to the systematic error in the measurement of $A_{b\bar{b}}^{obs}$. The systematic uncertainty has been estimated by changing various parameters by at least one standard deviation of their known or estimated uncertainties. The systematic error is dominated by the uncertainties in the measured B^0-$\bar{B}^0$ mixing parameter, knowledge about the background (including b background), the probability assignment in the fit and $A_{c\bar{c}}$ (with large change). The error due to the uncertainty in χ_B measurement is $\Delta A_{b\bar{b}}^{obs} = 2A_{b\bar{b}}\Delta\chi_B$. Because the charge sign of the background from b hadron decays is correlated with the original b quark and is not well known, it is one of the major systematic errors. The error coming from the uncertainty in assigning probabilities to events has been estimated by changing the number of leptons required in the fit box, as well as by using different samples of Monte Carlo. The systematic errors from heavy quark partial decay width and semileptonic branching ratio are relative small due to the fact that the

Parameter	Variation	$\Delta A_{b\bar{b}}^{obs}$
$\Gamma_{b\bar{b}} = 378\ MeV$	$\pm 10\ MeV$	± 0.001
$Br(b \to l\nu X) = 0.117$	± 0.010	± 0.004
ϵ_b=0.05	± 0.25	± 0.003
$A_5 = 0.70 A_{b\bar{b}}$	0 to $A_{b\bar{b}}$	± 0.004
$A_{c\bar{c}}$	$\pm 5\%$	± 0.006
$Br(c \to l\nu X) = 0.096$	± 0.010	± 0.003
$\Gamma_{c\bar{c}} = 297\ MeV$	$\pm 7\ MeV$	± 0.0003
background	$\pm 15\%$	± 0.005
$A_{back} = 0.0$	$\pm 5\%$	± 0.004
muon dE/dX	$0.36\ GeV$	$+0.003$
$\Delta p_\perp / p_\perp$ smearing	20%	± 0.004
$\Delta p/p$ smearing	10%	± 0.001
D^{**} fraction = 0.15	± 0.15	< 0.001
0.5% charge confusion	—	-0.001
probability assignment	—	± 0.007
systematic error in χ_B	± 0.02	± 0.005

Table 8.8: *Contributions to systematic errors in the $A_{b\bar{b}}^{obs}$ measurement*

asymmetry is measured by the ratio of the number of forward events (N_F) to the number of backward events (N_B), which cancels the effect. For instance, if all the events in the data sample were from b quark, the asymmetry would be free from $\Gamma_{b\bar{b}}$. The effect of the reconstruction errors and the jet reconstruction uncertainty is estimated by smearing the lepton momentum and the transverse momentum, and by the studying systematic effects due to muon energy loss in the calorimeter. From these studies, the systematic error of $A_{b\bar{b}}^{obs}$ is determined to be ± 0.015.

$$A_{b\bar{b}}^{obs} = 0.082 \pm 0.024(stat) \pm 0.015(sys) \tag{8.35}$$

Table 8.9 lists the number of forward and backward single inclusive lepton events with $p_\perp > 1.5\ GeV$ and $p_\perp > 1\ GeV$ for muon and electron respectively. With this

Type	N_F	N_B	$(N_F - N_B)/(N_F + N_B)$	$p_\perp$ *cut* (GeV)
$\mu + hadrons$	1055	896	0.082 ± 0.023	$p_{\mu\perp} > 1.5$
$e + hadrons$	486	475	0.011 ± 0.032	$p_{e\perp} > 1.0$
$\mu e + hadrons$	1497	1336	0.057 ± 0.019	$p_{\mu\perp} > 1.5; p_{e\perp} > 1.0$

Table 8.9: *Number of selected forward and backward single inclusive lepton events in the data sample with $p_\perp$ cut.*

cut the data sample consist of approximately 80% $b \to \ell$ events. Clearly there is forward-backward asymmetry in the data sample. A fit is performed, which is based on the number of forward and backward accepted events, with a weighting function:

- $W_k(i) = 0.5(1 + A_k)$ for forward events

- $W_k(i) = 0.5(1 - A_k)$ for backward events

The result is similar to the previous fitting result (there is about 1% difference in the fitting result). Figure 8-3 shows the acceptance corrected angular distribution of the measured b quark direction, for events with muon and electron candidates in the high $p_\perp$ region, after subtracting the background contributions from the cascade $b \to c \to \ell$, $c\bar{c}$ and lighter quarks. The smooth curve is the expected distribution for $A_{b\bar{b}}^{obs} = 0.082$. It agrees with the data points.

The value of the observed $b\bar{b}$ asymmetry must be corrected for the presence of B^0-$\bar{B}^0$ mixing, which reduces the asymmetry by a factor of $(1 - 2\chi_B)$. Using the measured value of χ_B (see chapter B^0-$\bar{B}^0$ Mixing), $\chi_B = 0.178^{+0.049}_{-0.040} \pm 0.017$, the true $b\bar{b}$ forward-backward asymmetry is:

$$A_{b\bar{b}} = \frac{A_{b\bar{b}}^{obs}}{1 - 2\chi_B} = 0.127^{+0.042}_{-0.040}(stat) \pm 0.023(sys) \tag{8.36}$$

The result is compatible with the Standard Model prediction, $A_{b\bar{b}}^0 = 0.104$, for the Higgs mass of 100 GeV, the top quark mass of 193 GeV [8-1] and $\sqrt{s} = 91.28\ GeV$. A fit is performed to simultaneously determine $A_{b\bar{b}}$ and χ_B taking into account the correlations between $A_{b\bar{b}}$ and χ_B. The yielded results are identical to above $b\bar{b}$ asymmetry value and the B^0-$\bar{B}^0$ mixing parameter χ_B, both for central values and errors.

8.8 Systematic Studies

The measured momentum and transverse momentum are the most important variables in the determination of heavy quark properties from heavy quark semileptonic decays. In order to understanding the effects, similar analyses have been done by using different lepton $p_\perp$ definitions and lepton data samples, where the lepton momentum is measured with high resolution. This studies are performed on the inclusive muon data sample.

The $p_\perp$ used in this analysis is calculated with respective to the nearest jet, where the measured lepton momentum is first excluded from the jet. Also the measured lepton momentum can be included in the calculation of the jet axis. Figure 8-4 and Figure 8-5 show the energy of the nearest jet and $p_\perp$ distributions compared with same distributions of Monte Carlo simulation in both cases. Data and Monte Carlo are in good agreement. The b quark properties are measured using these two different $p_\perp$ definitions by fitting the data lepton $p - p_\perp$ distribution. Table 8.10 gives the results, where no $p_\perp$ cut has been applied. All the results agree with each other within the statistical errors.

The muons measured by three layers of P-chamber have high momentum resolution. By only taking events with muons which are reconstructed in three P-chamber layers, one can understand the resolution effects in the measurements. Without $p_\perp$ cut, the fitted results are summaried in Table 8.11 from the inclusive muon data, where the muon track is required to have 3 reconstructed P-chamber segments. The

Measured parameter	μ excl. from jet	μ incl. in jet
$\Gamma_{b\bar{b}}\ (MeV)$	395 ± 8	391 ± 8
$Br(b \to \mu\nu X)$	0.122 ± 0.003	0.119 ± 0.003
ϵ_b	0.050 ± 0.005	0.047 ± 0.005
$A_{b\bar{b}}^{obs}$	0.101 ± 0.028	0.108 ± 0.029

Table 8.10: *Measured b quark properties with two different $p_\perp$ definitions from the inclusive muon sample.*

Measured parameter	Fitting result
$\Gamma_{b\bar{b}}\ (MeV)$	396 ± 10
$Br(b \to \mu\nu X)$	0.124 ± 0.004
ϵ_b	0.049 ± 0.005
$A_{b\bar{b}}^{obs}$	0.105 ± 0.034

Table 8.11: *Measured b quark properties from the inclusive muon sample, where the muon track is required to have 3 P segments.*

results are in good agreement as comparing to the results from the whole inclusive muon data sample (see Table 8.10).

8.9 Determination of V_{cb}

The measurement of the average b quark semileptonic branching ratio, combined with the L3 measurement of the average b hadron lifetime [8-11], $\tau_B = 1.32 \pm 0.08 \pm 0.09$, can be used to determine the magnitude of the CKM matrix element $|V_{cb}|$ together with the ratio $|V_{ub}/V_{cb}|$. In the free-quark model, the CKM matrix elements V_{ub} and V_{cb} are related to the b semileptonic branching ratio and lifetime through:

$$\Gamma(B \to l\nu X) = \frac{Br(b \to l\nu X)}{\tau_B} = \frac{G_F^2 M_b^5}{192\pi^3}(f_c|V_{cb}|^2 + f_u|V_{ub}|^2) \qquad (8.37)$$

where parameters f_q $(q = u, c)$ account for the phase space corrections due to fermions masses and the QCD corrections, and can be formulated as:

$$f_q = (1 - 8\epsilon_q^2 - 24\epsilon_q^4 ln\epsilon_q + 8\epsilon_q^6 - \epsilon_q^8)\{1 - \frac{2\alpha_s(M_b^2)}{3\pi}[(\pi^2 - \frac{31}{4})(1 - \epsilon_q)^2 + \frac{3}{2}]\} \quad (8.38)$$

where $\epsilon_q^2 = M_q/M_b$. According to the spectator model, the light B mesons produced at the $\Upsilon(4S)$ have the same semileptonic widthes as the heavier b hadrons from Z^0 decays.

Estimates of f_b and f_u depend on the assumptions for quark masses. The u quark mass is taken as $M_u = 0.2 \pm 0.2\ GeV$. The heavy quark masses are $M_b = 4.95 \pm 0.07\ GeV$ and $M_b - M_c = 3.30 \pm 0.02\ GeV$, which were measured by the ARGUS Collaboration [8-12] in the framework of the ACCMM model [8-13] from

a fit to the lepton momentum distribution in b semileptonic decays. In order to account for the uncertainties in the model, the error on M_b is increased to $\pm 0.3\ GeV$, keeping the error on $M_b - M_c$ as above value. The strong coupling constant has been obtained from extrapolating the L3 measurement $\alpha_s = 0.115 \pm 0.009$ [8-14] at $\sqrt{s} \approx M_Z$ to $Q^2 = M_b^2$ by using the formula:

$$\alpha_s(Q^2) = \frac{\alpha_s(M_Z^2)}{1 + \frac{\alpha_s(M_Z^2)}{12\pi}(33 - 2n_f)\ln(Q^2/M_Z^2)} \tag{8.39}$$

where the n_f is the number of flavors, which gives $\alpha_s(M_b)^2 = 0.20 \pm 0.03$.

From Equation 8.37, the measured values of τ_B and $Br(b \to l\nu X)$ give a band of allowed $|V_{ub}|$ and $|V_{cb}|$ shown in Figure 8-6. The solid curve represents the central values, and the dashed curves describe the limits of one standard deviation errors, where the statistical and systematic errors are added in quadrature. The error comes from the measurement uncertainties of τ_B, $Br(b \to l\nu X)$ and α_s, also our knowledge of quark masses. If the error of $\pm 0.02\ GeV$ on $M_b - M_c$ is kept intact, varying M_b by $\pm 0.30\ GeV$ results in the change of the factor $M_b^5 f_c$ in Equation 8.37 by only 12% compared with the $\pm 30\%$ change in M_b^5 alone, this is because of the anti-correlation between M_b and f_c. The errors becomes wider when going from the V_{cb} axis to the V_{ub} axis in Figure 8-6 due to the fact that there is less anti-correlation between M_b and f_u.

The experimental measurements [8-15] indicate that V_{ub} is rather small,

$$\frac{|V_{ub}|}{|V_{cb}|} < 0.12 \tag{8.40}$$

however, this limit varying in the range from 0.1 to 0.2 for different models. The value of $|V_{ub}/V_{cb}| = 0.15 \pm 0.10$ is used to extract $|V_{cb}|$, which produces the straight solid line shown in Figure 8-6. The dashed lines are the bounds of $|V_{ub}/V_{cb}|$ with its estimated error. From Figure 8-6 one can see that $|V_{cb}|$ is relatively insensitive to the ratio $|V_{ub}/V_{cb}|$, for instance, $|V_{cb}|$ changes by only 0.003 when $|V_{ub}/V_{cb}|$ varies from 0.05 to 0.25. The measured value of $|V_{cb}|$ is:

$$|V_{cb}| = 0.046 \pm 0.002\ ^{+0.004}_{-0.003} \tag{8.41}$$

where the first error is from the uncertainties of $Br(b \to l\nu X)$ and τ_B, and the second one comes from the knowledge on the quark masses [1] $|V_{ub}/V_{cb}|$ and α_s. This measurement improves the previous measurements from other experiments [8-16].

8.10 Determination of $\sin^2\bar{\Theta}_W$

In the framework of the improved Born approximation, the forward-backward asymmetry for $Z^0 \to b\bar{b}$ may be interpreted in terms of the ratio of the the effective vector

[1] Using the error of $\pm 0.1\ GeV$ on $M_b - M_c$ instead of $\pm 0.02\ GeV$, it increases the second error on $|V_{cb}|$ to $^{+0.005}_{-0.004}$.

and axial-vector coupling constants as shown in following Equation 8.42,

$$\begin{aligned} A_{bb} &= \frac{3}{4} \cdot A_e \cdot A_b \\ &= \frac{3}{4} \cdot \frac{2\bar{g}_{ve}\bar{g}_{ae}}{\bar{g}_{ve}^2 + \bar{g}_{ae}^2} \cdot \frac{2\bar{g}_{vb}\bar{g}_{ab}\beta}{\bar{g}_{vb}^2(3-\beta^2)/2 + \bar{g}_{ab}^2\beta^2} \\ &\approx \frac{3}{4} \cdot \frac{2\bar{g}_{ve}\bar{g}_{ae}}{\bar{g}_{ve}^2 + \bar{g}_{ae}^2} \cdot \frac{2\bar{g}_{vb}\bar{g}_{ab}}{\bar{g}_{vb}^2 + \bar{g}_{ab}^2} \cdot (1+\delta_b) \end{aligned} \tag{8.42}$$

with

$$\delta_b = \frac{4M_b^2}{s} \cdot \frac{-\bar{g}_{vb}^2 + \bar{g}_{ab}^2/2}{\bar{g}_{vb}^2 + \bar{g}_{ab}^2} \tag{8.43}$$

where the mass correction is included. The mass correction δ_b is strongly suppressed to $\mathcal{O}(10^{-4})$ because of the accidental cancellation among the couplings ($\bar{g}_{vb}^2 \simeq \bar{g}_{ab}^2/2$).

The effective vector and axial-vector couplings are:

$$\bar{g}_{af} = \sqrt{\rho_f} \cdot I_{3f} \qquad \bar{g}_{vf} = \sqrt{\rho_f} \cdot [I_{3f} - 2Q_f \sin^2\bar{\theta}_W(1 + \frac{2}{3}\Delta\rho\,\delta_{fb})] \tag{8.44}$$

the term $\frac{2}{3}\Delta\rho\,\delta_{fb}$ comes from the vertex correction involving the heavy top quarks and modifies $\sin^2\bar{\theta}_W$ by $+0.0007$ for the top mass of 193 GeV. Since the b quark term A_b (see Equation 8.42) is nearly independent of $\sin^2\bar{\theta}_W$, most of the sensitivity to $\sin^2\bar{\theta}_W$ comes from the electron term A_e in Equation 8.42. In deriving $\sin^2\bar{\theta}_W$, the difference between the Z^0 mass ($M_Z = 91.181\ GeV$) and the effective center-of-mass energy ($\sqrt{s} = 91.28\ GeV$), initial-state radiation and photon-exchange diagram are taken into account. A second order QCD correction is made to account for the effect of the gluon bremsstrahlung, which changes the $b\bar{b}$ asymmetry by $+0.003$. The formulation given in Reference [8-17] is used to including all these correction. From the $b\bar{b}$ asymmetry the following value of effective mixing angle has been obtained:

$$\sin^2\bar{\theta}_W = 0.226 \pm 0.008(stat) \pm 0.005(sys) \tag{8.45}$$

where the systematic error includes the effects from the following sources: the systematic uncertainty of the $b\bar{b}$ asymmetry measurement; the variation of the top mass by $\pm 100\ GeV$; the variation of Higgs mass from 40 GeV to 1 TeV; and the uncertainties of the Z^0 mass and strong coupling constant α_s. The value of this measurement agrees with the Standard Model prediction of $\sin^2\bar{\theta}_W = 0.231$ for a Higgs mass of 100 GeV, a top quark mass of 193 GeV and $\sqrt{s} = 91.28\ GeV$.

Chapter 9

B^0-$\bar{B}^0$ Mixing

9.1 Introduction

Flavor-changing weak interaction are able to transform a neutral meson into its antiparticle, leading to the possibility of flavor oscillations or mixing. The level of B^0-$\bar{B}^0$ mixing is sensitive to some parameters of the Standard Model, such as the top quark mass and CKM matrix elements involving the coupling of the top quark [9-1]. Previous observations of B^0-$\bar{B}^0$ mixing [9-2] indicated that the top quark is heavy and gave limits on the CKM matrix elements. In this chapter, the measurement of B^0-$\bar{B}^0$ mixing performed at $\sqrt{s} \approx M_Z$ is presented.

The B^0-$\bar{B}^0$ mixing parameter χ_B, which gives the probability that a hadron containing a b quark oscillates into a hadron containing a $\bar{b}$ at the time of its decay, is defined as following:

$$\chi_B = \frac{Prob(b\ hadron \rightarrow l^+X)}{Prob(b\ hadron \rightarrow l^+X) + Prob(b\ hadron \rightarrow l^-X)} \tag{9.1}$$

This definition includes all produced neutral and charged b mesons and b baryons. In e^+e^- annihilation, b hadrons are always produced in pairs, such that initially there is one hadron containing a b quark and one hadron containing a $\bar{b}$ quark. Events of the type $Z^0 \rightarrow b\bar{b}$ are identified by the observation of leptons (muon and electron) coming from the semileptonic decay of the b or $\bar{b}$ quark. In order to identify both b hadrons, both b hadrons are required to decay semileptonically, in which case a negative lepton indicates the b hadron while a positive lepton indicates the $\bar{b}$ hadron. Then the signature for B^0-$\bar{B}^0$ mixing in inclusive lepton events is an event with two leptons of the same charge on opposite sides of the event (*like-sign dileptons*). The leptons are considered to be on opposite sides when the angle between them is greater than 60°. As an example, Figure 6-1 shows a hadronic event containing two high momentum leptons, one muon and one electron. Both leptons come from the interaction region and have positive charge. There are background processes, in which one b decays into a prompt lepton ($b \rightarrow l^-$), and the second decays via the cascade $\bar{b} \rightarrow \bar{c} \rightarrow l^-$, J/ψ decays or misidentified hadron, which also can produce events with lepton pairs of like-sign charges. Because of the hard fragmentation and large mass of the b quark, leptons from b semileptonic decay have large momentum

p and large transverse momentum $p_\perp$, which separates leptons from prompt b decay and background processes.

As only the b quark sign on each side is tagged and we do not distinguish between B_d^0 and B_s^0 mesons in this analysis, the measured mixing parameter χ_B is a combination of the oscillation in the ${B_d}^0$-$\bar{B}_d^0$ and ${B_s}^0$-$\bar{B}_s^0$ system. Assuming that the production of b and $\bar{b}$ hadrons on both sides has no correlation and the semileptonic branching ratios for all b hadrons are the same, the mixing parameter χ_B can be expressed as:

$$\chi_B = f_d\chi_d + f_s\chi_s \tag{9.2}$$

where f_d and f_s are the fractions of B_d^0 and B_s^0 produced, and χ_d and χ_s are the mixing parameters for B_d^0 and B_s^0 mesons.

In the fragmentation of b quark into the hadrons, a pair of b hadrons are produced, such as $B_d^0\bar{B}_d^0$, $B_d^0\bar{B}_s^0$ and $B_d^0B^-$ etc. The Equation 9.2 is based on the assumption that the production of two b hadrons are completely uncorrelated. Ignoring the contribution to the *like-sign dilepton* events from the background, all the *like-sign dilepton* events come from the events where one b hadron has oscillated. The number of *like-sign dilepton* events is:

$$N^{\pm\pm} = 2\chi_B(1-\chi_B)N \tag{9.3}$$

where N is total number of $b\bar{b}$ events with both b hadrons decay semileptonically. Table 9.1 gives the probabilities for different b hadron pair combinations and the contribution to the *like-sign dilepton* events. In the Table 9.1, B^+ and B^- represent

b had. Type	probability	# of *like-sign dilepton* events
$B_d^0B_d^0$	f_d^2	$2\chi_d(1-\chi_d)f_d^2N$
$B_d^0\bar{B}_s^0$ or $\bar{B}_d^0B_s^0$	$2f_df_s$	$[\chi_s(1-\chi_d)+\chi_d(1-\chi_s)]2f_df_sN$
$B_d^0B^-$ or $B_d^0B^+$	$2f_d(1-f_d-f_s)$	$\chi_d2f_d(1-f_d-f_s)N$
$B_s^0B^-$ or $B_s^0B^+$	$2f_s(1-f_d-f_s)$	$\chi_s2f_s(1-f_d-f_s)N$
$B_s^0B_s^0$	f_s^2	$2\chi_s(1-\chi_s)f_s^2N$
B^+B^-	$(1-f_d-f_s)^2$	0

Table 9.1: *Like sign dilepton events from different b hadron combinations.*

charged B meson and b baryons. Adding all the *like-sign dilepton* events from different sources, one gets:

$$N^{\pm\pm} = 2(f_d\chi_d + f_s\chi_s)(1 - f_d\chi_d + f_s\chi_s)N \tag{9.4}$$

From Equation 9.3 and 9.4, the combined mixing parameter χ_B is $f_d\chi_d + f_s\chi_s$.

9.2 B^0-$\bar{B}^0$ Mixing Sample

As discussed in the early Chapter, the lepton candidates can be classified into eight categories to distinguish mixing events from background. The amount of mixing, χ_k, for each category is given by:

(1) $\chi_1 = \chi_B$ for $b \to \ell$

(2) $\chi_2 = \chi_B$ for $b \to \tau \to \ell$

(3) $\chi_3 = \chi_B$ for $b \to c \to \ell$

(4) $\chi_4 = \chi_B$ for $b \to \bar{c} \to \ell$

(5) $\chi_5 = 0.7\chi_B + 0.15$ for $b \to b$-hadron $\to$ background

(6) $\chi_6 = 0$ for $c \to \ell$

(7) $\chi_7 = 0$ for decay leptons from *udsc* quarks and $b\bar{b}$ fragmentation

(8) $\chi_8 = 0$ for fake leptons from *udsc* quarks and $b\bar{b}$ fragmentation

From Monte Carlo studies at the generator level, a strong correlation between the charge of K, π from b hadron decay and original b quark is observed. Table 9.2 lists the number of K *and* π from b hadron decays. About 80% K^- and 87% π^- come

Decay product	b quark	$\bar{b}$ quark
K^+	849	3332
K^-	3384	855
π^+	2803	18116
π^-	17915	2746

Table 9.2: *The number of K and π from b hadron decay from Monte Carlo studies.*

from the b quarks, hence the background from the b hadron decays would carry the mixing information. The effective mixing probability χ_5 of b background is large than χ_B due to the random production of the charged particles. From Equation 9.1, the effective χ_5, the probability of b decay into positive particle, is:

$$\chi_5 = Prob(b \to X^+) = 0.85\chi_B + 0.15(1 - \chi_B) = 0.7\chi_B + 0.15 \qquad (9.5)$$

15% is the average fraction of positive particles from the b quark. In Equation 9.5 the term $0.15(1-\chi_B)$ is the probability of observed positive particles from b quarks, while $0.85\chi_B$ is the probability of observed negative particles from $\bar{b}$ quarks because of oscillation.

The dilepton events are classified into eight categories, where the $b \to l$ also includes events with leptons from the cascades $b \to \tau \to \ell$, and $b \to \bar{c} \to \ell$. These cascades yield a lepton with the same sign as direct $b \to \ell$ decays. Table 9.3 shows the results of Monte Carlo studies giving the fraction of each source of prompt dileptons and of background for the data samples with no cut on $p_\perp$, and also with the high-$p_\perp$ requirement, which select preferentially $b \to \ell, b \to \ell$ events. The requirement is that the muons have $p_\perp > 1.5\ GeV$ and electrons have $p_\perp > 1.0\ GeV$ and the two leptons must be on opposite sides of the event. These $p_\perp$ cuts correspond to prompt $b \to \ell$ probabilities for electrons and muons of about 80%. The high-$p_\perp$

Lepton Pair Category	$p_\perp > 0$	high-$p_\perp$
1: $b \to \ell$, $b \to \ell$	47 %	80 %
2: $b \to c \to \ell$, $b \to c \to \ell$	5 %	2 %
3: $b \to \ell$, $b \to c \to \ell$	20 %	10 %
4: $b \to \ell$, $b \to$ background	9 %	5 %
5: $b \to c \to \ell$, $b \to$ background	3 %	1 %
6: $b \to$ background, $b \to$ background	1 %	0 %
7: $c \to \ell$, $c \to \ell$	7 %	0 %
8: others	9 %	2 %

Table 9.3: *Monte Carlo estimates of the fractions of various categories of dilepton events in the data*

sample can be used to estimate the B^0-$\bar{B}^0$ mixing by simple event counting. In Table 9.3, the first three sources are sensitive to B^0-$\bar{B}^0$ mixing, categories 4, 5 and 6 carry the mixing information because the charge of backgrounds arising from b hadron has a correlation with the original b quark, and the last two ($c \to \ell, c \to \ell$ and others) are not sensitive to B^0-$\bar{B}^0$ mixing. Leptons from J/ψ decay give false signal for mixing, there are about 2% J/ψ decay contribution to the dilepton sample, but only 0.9% in the high $p_\perp$ sample. They have a negligible effect on the mixing measurement.

Figure 9-1 shows a comparison for data and Monte Carlo for the smaller of the two lepton momenta in the inclusive dilepton sample which have passed the selection cuts. Figure 9-2 shows a similar distribution for the minimum transverse momentum with respect to the nearest jet, $p_\perp$, of each dilepton pair. The fraction of prompt b semileptonic decay events increases at higher p and $p_\perp$. Therefore, events with opposite side, high momentum p and high transverse momentum $p_\perp$ are most likely from prompt $b \to$ decays. An excess above background of hadronic events with two like-sign lepton in the region of high p and high $p_\perp$ dominated by leptons from prompt b semileptonic decays is a signal for B^0-$\bar{B}^0$ mixing. A value of χ_B can be extracted from the data by considering only lepton candidates with high p and high $p_\perp$ and subtracting the predicted background. A summary of the dilepton date sample is given in Table 9.4 here the high-$p_\perp$ requirement is described early. The number of events with electrons is smaller because of the strong isolation

Data Type	l^+l^-	l^+l^+	l^-l^-	Total
all $\mu\mu$ events	109	41	22	172
high-$p_\perp$ $\mu\mu$ events	22	3	4	29
all ee events	9	3	5	17
high-$p_\perp$ ee events	6	1	2	9
all μe events	42	18	14	74
high-$p_\perp$ μe events	20	3	7	30

Table 9.4: *Dilepton events in the data*

requirements. Without the $p_\perp$ cut, due to the difference in the punchthrough for

positive and negative charged particles, there is an excess of $\mu^+\mu^+$ events compared to $\mu^-\mu^-$ events.

Subtracting the predicted backgrounds from Monte Carlo, and inserting the estimates of the fractions of various dilepton categories, from the ratio $N^{\pm\pm}/N^{ll}$ the mixing parameter can be determined:

$$\begin{aligned}\frac{N^{\pm\pm}}{N^{ll}} &= (f^{b\to\ell,b\to\ell} + f^{b\to c\to\ell,b\to c\to\ell})\cdot 2\chi_B(1-\chi_B) \\ &+ f^{b\to\ell,b\to c\to\ell}\cdot[(1-\chi_B)^2+\chi_B^2] \\ &+ f^{b\to\ell,b\to\text{background}}\cdot[\chi_B(1-\chi_5)+\chi_5(1-\chi_B)] \\ &+ f^{b\to c\to\ell,b\to\text{background}}\cdot[(1-\chi_B)(1-\chi_5)+\chi_5\chi_B] \\ &+ f^{b\to\text{background},b\to\text{background}}\cdot 2\chi_5(1-\chi_5) \\ &+ 0.5\cdot f^{others} \end{aligned} \tag{9.6}$$

where the N^{ll} is total number of dilepton events. Using the data in Table 9.4, the ratio $N^{\pm\pm}/N^{ll}$ for opposite-side, high-$p_\perp$ events is 0.29 ± 0.05 while in the Monte Carlo (with $\chi_B=0$) it is 0.13 ± 0.04. The excess of like-sign events in the opposite side in the data as compared to the $\chi_B=0$ Monte Carlo is a clear evidence for B^0-$\bar{B}^0$ mixing. From Equation 9.6 and the ratio $N^{\pm\pm}/N^{ll}$, the mixing parameter χ_B is determined to be $\chi_B = 0.129\pm0.050$, where the error is statistical only.

9.3 Measurement of χ_B

At very large p and $p_\perp$ there is almost no background, the simple counting procedure weights all events equally. The statistical accuracy on χ_B can be enhanced by using a fitting procedure which gives a larger relative weight for events with high p and high $p_\perp$ leptons than events with low p or low $p_\perp$ leptons, where high p and high $p_\perp$ leptons are most likely from prompt b decays. This method allows the amount of data to be increased without losing the large p and $p_\perp$ event's sensitivity to mixing.

An event by event maximum likelihood fit is performed to determine the mixing parameter χ_B by fitting to two p and $p_\perp$ spectra for like-sign and unlike-sign dileptons events observed in hadronic decays of the Z^0. For dilepton events, the likelihood function is:

$$L = \frac{(N_{M2})^{N_{D2}}\cdot e^{-N_{M2}}}{N_{D2}!}\prod_{i=1}^{N_{D2}}\frac{1}{N_{M2}V_{box}(i)}\sum_{k,l}N_{k,l}(i)W_{k,l}(i) \tag{9.7}$$

where $W_{k,l}(i)$ is the weighting function, and $V_{box}(i)$ is the volume of the box. Because a minimum of 40 events is required in a box, the four dimensional space $(p_1, p_{\perp 1}, p_2, p_{\perp 2})$ is sparsely populated in the region of interest, where both leptons have high p and high $p_\perp$, Therefor the box can become large even with all the b-flavor Monte Carlo events. So, the relative weight of each Monte Carlo event in the box is calculated assuming exponential distributions in p and $p_\perp$. The Monte Carlo events are generated with no mixing, $\chi_B=0$, and must be weighted assuming

that a fraction χ_B leptons from b hadrons will change sign. Only the events with opposite-side dileptons contribute to the dilepton likelihood function. The weighting function of different class dileptons is listed in Table 9.5. This procedure for

Lepton Pair Category	$Q_1 \cdot Q_2 > 0$	$Q_1 \cdot Q_2 < 0$
1: $W_{b\to\ell,b\to\ell}$	$2\chi_B(1-\chi_B)$	$(1-\chi_B)^2+\chi_B^2$
2: $W_{b\to c\to\ell,b\to c\to\ell}$	$2\chi_B(1-\chi_B)$	$(1-\chi_B)^2+\chi_B^2$
3: $W_{b\to\ell,b\to c\to\ell}$	$(1-\chi_B)^2+\chi_B^2$	$2\chi_B(1-\chi_B)$
4: $W_{b\to\ell,b\to\text{background}}$	$\chi_5(1-\chi_B)+\chi_B(1-\chi_5)$	$(1-\chi_5)(1-\chi_B)+\chi_B\chi_5$
5: $W_{b\to c\to\ell,b\to\text{background}}$	$(1-\chi_5)(1-\chi_B)+\chi_B\chi_5$	$\chi_5(1-\chi_B)+\chi_B(1-\chi_5)$
6: $W_{b\to\text{background},b\to\text{background}}$	$2\chi_5(1-\chi_5)$	$(1-\chi_5)^2+\chi_5^2$
7: $W_{c\to\ell,c\to\ell}$	0	1
8: others	0.5	0.5

Table 9.5: *The mixing weight function for different class dileptons, where Q_1 and Q_2 are data lepton charges.*

determining χ_B has been cross-checked by fitting Monte Carlo event samples with different input χ_B values. All the fit results agree well with the input χ_B value.

The result of the fit is:

$$\chi_B = 0.122^{+0.057}_{-0.044} \quad for\ dimuon\ sample \tag{9.8}$$

$$\chi_B = 0.178^{+0.049}_{-0.040} \quad for\ dilepton\ sample \tag{9.9}$$

where the error is statistical only. The change in the logarithm of the likelihood function between this value and $\chi_B = 0$ is 32.3, or 8.0 standard deviations. This result is insensitive, within the statistical errors, to a variation of the lepton transverse momentum cut between 0.0 and 1.5 GeV. For example, a fit for χ_B with $p_\perp > 1.0\ GeV$ cut is repeated. In this restricted region, background is reduced substantially but also less statistic. The results are $\chi_B = 0.149 \pm 0.049$ and $\chi_B = 0.158 \pm 0.040$ (only statistical error), for muon and combined data sample respectively, in good agreement with the fit in the larger region. It indicates that the higher backgrounds at low $p_\perp$ are not influencing the result, thus the fit is relatively insensitive to the prediction of the background.

The systematic errors on χ_B arise from uncertainty in the prediction of the composition of the dilepton sample, the sources include the uncertainties of the heavy quark semileptonic branching ratio and fragmentation functions, lepton-hadron misidentification and background. These systematic effects are estimated by varying each with one standard deviation or more of their known or estimated error. Table 9.6 shows the systematic error on χ_B coming from each source of uncertainty. The systematic error is dominated by the possibility of charge confusion and the uncertainty in determination of the lepton $p_\perp$. The difference between data and Monte Carlo in the average dE/dX energy loss in the calorimeters for muons has similar effects as the uncertainty of the lepton $p_\perp$. Though the correlation between the charge of the b background (from b hadron decays) and the primary b quark has

Source	Variation	$\Delta\chi_B$
$\Gamma_{b\bar{b}} = 378\ MeV$	$\pm 10\ MeV$	± 0.0004
$Br(b \to l\nu X) = 0.117$	± 0.010	± 0.0015
ϵ_b=0.05	± 0.10	± 0.0014
$\chi_5 = 0.7\chi_B + 0.15$	from χ_B to 0.5	± 0.0033
$Br(c \to l\nu X) = 0.096$	± 0.010	± 0.0007
$\Gamma_{c\bar{c}} = 297\ MeV$	$\pm 7\ MeV$	± 0.0002
background	$\pm 15\%$	± 0.0005
muon dE/dX	$0.36\ GeV$	$+0.0035$
$\Delta p_\perp/p_\perp$ smearing	20%	± 0.0100
$\Delta p/p$ smearing	10%	± 0.0010
D^{**} fraction = 0.15	± 0.15	± 0.0004
0.5% charge confusion	—	$+0.0100$
opening angle requirement	from 45° to 90°	± 0.003
probability assignment	—	± 0.007

Table 9.6: *Sources of uncertainty and the corresponding systematic errors in the χ_B measurement*

been observed, it is not well known yet. Thus χ_5 is varied from χ_B (100% correlation) to 0.5 (no correlation at all) to estimate the systematic error. This changes χ_B by ± 0.0033. The error arising from the uncertainty in assigning probabilities to events has been estimated by changing the number of leptons required in the fit box (from 20 to 90), as well as using different samples of Monte Carlo events. Adding all contributions in quadrature, the combined systematic error is 0.017. The final result is:

$$\chi_B = 0.178^{+0.049}_{-0.040}(stat) \pm 0.017(sys) \tag{9.10}$$

As an additional check, the Monte Carlo events with $\chi_B = 0.178$ are generated and the distributions are compared with the data. Figure 9-3 shows the distribution of the lower momentum of two leptons in the opposite side together with the Monte Carlo predictions without and with mixing, where the $p_\perp$ is required to be more than 1 GeV both for muons and electrons.

9.4 Calculations of χ_s and ΔM_s

Using multihadronic Z^0 events with a pair of lepton candidates, the mixing parameter χ_B has been measured. The probability of $B^0 \to \bar{B}^0$ is determined to be $\chi_B = 0.178^{+0.052}_{-0.043}$. Information on χ_s can be obtained together with the combined ARGUS and CLEO measurements on χ_d [9-2]. As the B^0_d and B^0_s mesons are not distinguished in the analysis, our observed value of χ_B is a combination of B^0_d and B^0_s mixing. Assuming that b semileptonic branching ratio is equal for all B mesons and b baryons, the mixing parameter can be written as Equation 9.2. The relative abundances of B^0_d and B^0_s mesons at LEP energies are $f_d = 0.375$ and $f_s = 0.15$, which are estimated from the JETSET 7.2 program.

The weighted average of ARGUS and CLEO measurements of χ_d is $\chi_d = 0.16 \pm 0.04$, which is large, in the Standard Model it requires nearly complete mixing in the ${B_s}^0$-$\bar{B}_s^0$ system. Figure 9-4 shows our measurement χ_B along with the χ_d measurement and their $\pm\sigma$ bands in the $\chi_d - \chi_s$ plane. The Standard Model line indicates the upper limit on χ_d as a function of χ_s, which can be derived from existing limits on the CKM matrix elements with three families [9-3]. From our measurement of χ_B combined with the measurement of χ_d by ARGUS and CLEO and taking into account possible variation in the f_d and f_s parameters of up to 0.05, a value of $\chi_s = 0.79^{+0.54}_{-0.37}$ is found. However χ_s must lie in the range from 0 to 0.5, the usual statistical technique can not be used to give the lower limit on χ_s. A Gaussian distribution with one standard deviation $\sigma = 0.37$ is used to be the probability density function for $\chi_s < 0.79$, i.e.

$$f(\chi_s) = \frac{1}{\sqrt{2\pi}\sigma} exp[-\frac{(\chi_s - 0.79)^2}{2\sigma^2}] \tag{9.11}$$

When calculating limits, the non-physical regions are cut away and the remaining probability density is renormalized to one over the physical region [9-4]. For the lower limit on χ_s at certain CL is calculated by the following formula:

$$CL = \frac{\int_{x_{min}}^{0.5} f(x)dx}{\int_{0.0}^{0.5} f(x)dx} \tag{9.12}$$

The limits for χ_s are:

$\chi_s > 0.07$ at 95% CL. and

$\chi_s > 0.13$ at 90% CL.

with respect to the integral of the probability distribution for $0 \geq \chi_s \leq 0.5$.

The measured mixing parameter $\chi_B = 0.178^{+0.052}_{-0.043}$ gives $\chi_s = 0.79^{+0.54}_{-0.37}$. Combined it with the L3 b hadron lifetime measurement $\tau_b = 1.32 \pm 0.12$ [9-5], from the relationship,

$$\chi_s \approx \frac{x_s^2}{2 + 2x_s^2} \qquad x_s = \frac{\Delta M_s}{\Gamma} = \Delta M_s \cdot \tau_b \tag{9.13}$$

the lower limit on the mass difference ΔM_s between two B_s mass eigenstates can be determined by restricting the χ_s in the physical allowed region. The lower limit of ΔM_s are:

$\Delta M_s > 2.0 \times 10^{-4} eV$ at 95% CL. and

$\Delta M_s > 3.2 \times 10^{-4} eV$ at 90% CL.

Chapter 10

Conclusion

In this study, the properties of heavy quarks from Z^0 decays have been measured by using the data accumulated in 1989 and 1990 by the L3 experiment installed at the LEP e^+e^- collider at CERN. The heavy quark is tagged by inclusive lepton events. Due to the large mass and hard fragmentation, the leptons from heavy quark semileptonic decays have large momentum and transverse momentum. Especially b quarks can be separated with high purity from lighter quarks. An event by event unbinned maximum likelihood fit is performed to determine the heavy quark properties and the mixing parameter χ_B by fitting to the p and $p_\perp$ spectra for single lepton and dilepton events. The measurements on heavy quark partial width of the Z^0 decays and the $b\bar{b}$ forward-backward asymmetry in e^+e^- annihilation provide a test of the neutral current couplings to the heavy quarks. The observation of large B^0-$\bar{B}^0$ oscillation provides evidence of the existence of the top quark, which must be massive.

From the ratio of the number of inclusive dilepton events to the number of inclusive single lepton events, the b semileptonic branching ratio has been measured:

$$Br(b \to l\nu X) = 0.111 \pm 0.010(stat) \pm 0.006(sys) \tag{10.1}$$

which is almost independent of $\Gamma_{b\bar{b}}$. Combining this measurement with the PETRA and PEP measurements one obtains:

$$Br(b \to l\nu X) = 0.117 \pm 0.006 \tag{10.2}$$

This average is independent of assumptions about electroweak couplings, and therefore is used for the measurement of heavy quark properties.

By using the inclusive lepton data sample with the assumption of $\Gamma_{b\bar{b}} = 378\ MeV$ as predicted by the Standard Model, the fitted average b semileptonic branching ratio is found to be:

$$Br(b \to l\nu X) = 0.119 \pm 0.003(stat) \pm 0.006(sys) \tag{10.3}$$

Together with the ARGUS and CELO measurements on b and c quark masses, the ratio of $|V_{ub}/V_{cb}|$, the CKM matrix element $|V_{cb}|$ has been determined

$$|V_{cb}| = 0.046 \pm 0.002\ ^{+0.004}_{-0.003} \tag{10.4}$$

The neutral couplings between Z^0 and heavy quarks have been studied with inclusive lepton events, where the momentum and the transverse momentum of the lepton with respect to the closest jet is used to separate heavy quarks from lighter quarks. With the requirement of $p_\perp > 1\ GeV$ (about 80% events from $b\bar{b}$), the partial width of Z^0 decay into $b\bar{b}$ pairs is determined from a one-parameter fit, with the result:

$$\Gamma_{b\bar{b}} = 385 \pm 7(stat) \pm 15(sys) \pm 19(Br)\ MeV \tag{10.5}$$

in agreement with the Standard Model prediction. A two-parameter fit has been performed to determine $\Gamma_{b\bar{b}}$ and $\Gamma_{c\bar{c}}$ simultaneously, where only the inclusive muon data sample is used. The results are:

$$\Gamma_{b\bar{b}} = 396 \pm 10(stat) \pm 24(sys)\ MeV \tag{10.6}$$

$$\Gamma_{c\bar{c}} = 296 \pm 24(stat) \pm 36(sys)\ MeV \tag{10.7}$$

These results are consistent with Standard Model predictions.

Without assuming any b quark fragmentation function, a 7 bins fit has been made to fit the inclusive muon data. The measured average fractional energy of b hadron from b quark fragmentation is $<x_{_E}> = 0.680 \pm 0.011$. The shape of the fragmentation function is consistent with a Peterson *et al.* function. Assuming the b quarks were fragmented according to the Peterson *et al.* functional form, the b quark fragmentation has been measured by extracting ϵ_b from the fit. From the combined muon and electron data sample, the result is:

$$\epsilon_b = 0.050 \pm 0.004(stat) \pm 0.012(sys) \tag{10.8}$$

therefore the average fractional energy carried by b hadron is precisely determined

$$<x_{_E}> = 0.686 \pm 0.006(stat) \pm 0.020(sys) \tag{10.9}$$

Using the sign of inclusive lepton charge to tag primary b ($\rightarrow l^-$) or $\bar{b}$ ($\rightarrow l^+$) quark, the observed $b\bar{b}$ forward-backward asymmetry is

$$A_{b\bar{b}}^{obs} = 0.082 \pm 0.024(stat) \pm 0.015(sys) \tag{10.10}$$

$A_{b\bar{b}}$ after the correction from the mixing ($\chi_{_B}$ from this analysis),

$$A_{b\bar{b}} = 0.127^{+0.042}_{-0.040}(stat) \pm 0.023(sys) \tag{10.11}$$

The asymmetry measurement can be converted into a value of the effective mixing angle of $\sin^2\bar{\theta}_W$ after applying several corrections:

$$\sin^2\bar{\theta}_W = 0.226 \pm 0.008(stat) \pm 0.005(sys) \tag{10.12}$$

The above results can be compared with the Standard Model predictions of $A_{b\bar{b}}^0 = 0.104$ and $\sin^2\bar{\theta}_W = 0.231$ for Higgs mass of 100 GeV, top quark mass of 193 GeV and $\sqrt{s} = 91.28\ GeV$.

Hadronic events with two leptons (μ and e) produced in e^+e^- annihilation at the Z^0 pole have been used to measure the B^0-$\bar{B}^0$ mixing parameter χ_B. By fitting the inclusive dilepton p and $p_\perp$ spectra, χ_B is found to be:

$$\chi_B = 0.178^{+0.049}_{-0.040}(stat) \pm 0.017(sys) \tag{10.13}$$

The result is consistent with maximal mixing in the ${B_s}^0$-$\bar{B}^0_s$ system as expected in the Standard Model. The limits of $\chi_s > 0.13$ at 90% CL and $\chi_s > 0.07$ at 95% CL have been obtained. Also, the lower limit on the mass difference ΔM_s has been derived to be $\Delta M_s > 3.2 \times 10^{-4} eV$ and $\Delta M_s > 2.0 \times 10^{-4} eV$ at 90% and 95% CL respectively.

From all quark flavors, most attention at LEP has been devoted to the b quarks. The measurements on $b\bar{b}$ decays mode of Z^0 by LEP experiments [10-1] are summarized in Table 10.1. The other experiments give their results on $\Gamma_{b\bar{b}}$ and $Br(b \to$

	This Analysis	ALEPH [10-2]
$Br(b \to l\nu X)$	$0.119 \pm 0.003 \pm 0.006$	$0.103 \pm 0.004 \pm 0.005$ (Pre.)
$\Gamma_{b\bar{b}}\ (MeV)$	$385 \pm 7 \pm 15 \pm 19(Br)$	$334 \pm 13 \pm 12 \pm 17(Br)$ (Pre.)
$<x_E>$	$0.686 \pm 0.006 \pm 0.020$	0.719 ± 0.022 (Pre.)
$A^{obs}_{b\bar{b}}$	$0.082 \pm 0.024 \pm 0.015$	$0.093 \pm 0.021 \pm 0.005$
$A_{b\bar{b}}$	$0.127^{+0.042}_{-0.040} \pm 0.023$	$0.126 \pm 0.028 \pm 0.012$
χ_B	$0.178^{+0.049}_{-0.040} \pm 0.017$	$0.132 \pm 0.022^{+0.015}_{-0.012}$
$\sin^2\theta_W$	$0.226 \pm 0.008 \pm 0.005$	0.2262 ± 0.0053
$\lvert V_{cb}\rvert$	$0.046 \pm 0.002\ ^{+0.004}_{-0.003}$	$- - - -$
	DELPHI	OPAL [10-3]
$Br(b \to l\nu X)$	$0.106 \pm 0.005 \pm 0.005$ (Pre.)	$0.105 \pm 0.002 \pm 0.006$ (Pre.)
$\Gamma_{b\bar{b}}\ (MeV)$	$342 \pm 15 \pm 15 \pm 18(Br)$ (Pre.)	$340 \pm 7 \pm 16 \pm 17(Br)$ (Pre.)
$<x_E>$	0.703 ± 0.032 (Pre.)	$0.727 \pm 0.007 \pm 0.022$ (Pre.)
$A^{obs}_{b\bar{b}}$	$0.115 \pm 0.043 \pm 0.014$ (Pre.)	$0.072 \pm 0.042 \pm 0.010$
$A_{b\bar{b}}$	$0.161 \pm 0.061 \pm 0.020$ (Pre.)	$0.097 \pm 0.057 \pm 0.014$
χ_B	$- - - -$	$0.150^{+0.044\ +0.016}_{-0.038\ -0.015}$ (Pre.)
$\sin^2\theta_W$	0.221 ± 0.012 (Pre.)	0.232 ± 0.010
$\lvert V_{cb}\rvert$	$- - - - -$	$- - - -$

Table 10.1: *The measurements on b quarks by LEP experiments*

$l\nu X$) as the product $\Gamma_{b\bar{b}}/\Gamma_{had} \cdot Br(b \to l\nu X)$. In order to compare the LEP results $\Gamma_{b\bar{b}}$ value, $\Gamma_{b\bar{b}}$ is calculated by inserting the average hadronic width measured at LEP, $\Gamma_{had} = 1742 \pm 12\ MeV$, and the average b semileptonic branching ratio $Br(b \to l\nu X) = 0.117 \pm 0.006$, which is independent of $\Gamma_{b\bar{b}}$. The semileptonic branching ratio is determined by assuming the partial width $\Gamma_{b\bar{b}}$ and $\Gamma_{c\bar{c}}$ from the Standard Model. All measurement are compatible within errors. The measurements from MARK II and UA1 can be found in [10-4].

Presently all measurements are limited by statistics and therefore significant reductions in the measurement errors can be expected in the near future with 10^6 Z^0

events. The double tagging method is very promising in determining the b semileptonic branching ratio with high precision, independent of $\Gamma_{b\bar{b}}$. Also, the semileptonic branching ratio $Br(c \to l\nu X)$ can be improved at high statistics. Higher statistics will also help to reduce the systematic errors. Significant improvements on $\Gamma_{b\bar{b}}$ and $A_{b\bar{b}}$ can be achieved, which can help in understanding the weak interaction of the heavy quarks. A high statistics measurement of the $b\bar{b}$ forward-backward asymmetry, $A_{b\bar{b}}$, will provide a precise determination of the weak mixing angle $\sin^2\bar{\theta}_W$. Comparing $\sin^2\bar{\theta}_W$ from $b\bar{b}$ and leptonic Z^0 decays will give a stringent test of the Standard Model.

With more data, $\chi_{\bar{B}}$ can be precisely determined. It is also possible to observe and measure the ${B_s}^0$-$\bar{B}_s^0$ system oscillation at different decay length of B_s mesons. The precise measurement of χ_s will provide a stringent test of the validity of the Standard Model. The precise determination of B^0-$\bar{B}^0$ mixing, together with the mass limit of the top quark and improvements in the accuracy of the theoretical calculations, may give hints about new physics. For instance, the charged Higgs particles and right-handed W bosons could contribute to the box-diagram amplitudes and enhance B^0-$\bar{B}^0$ mixing.

More precise determinations of the semileptonic branching ratio $Br(b \to l\nu X)$, b hadron lifetime and the mixing parameters (χ_d and χ_s) can be used to improve knowledge about the CKM matrix elements and thus will improve our knowledge of electroweak interactions.

Appendix A

Trigger Efficiency

Table A.1 shows the number of inclusive lepton events triggered by different triggers, where the events with trigger DAQ problems are removed (such as trigger data transfer problem etc.). For inclusive muon events (including inclusive dimuon

Trigger	$\mu + X$	$\mu\mu + X$	$e + X$
All	5325	213	1458
Cal.	5321	213	1458
SCNT Mult.	5148	201	1437
TEC	5209	210	1436
Muon	4558	210	—

Table A.1: *Number events triggered by each trigger*

events), among 5325 selected $\mu + hadrons$ events, 5321 events are triggered by the calorimeter trigger. The calorimeter trigger efficiency is measured by comparing the number of events which are triggered by both the calorimeter trigger and an another independent trigger to the number of events which are triggered by this independent trigger. For instance, among 5209 events, which were triggered by the TEC trigger, there are 5206 events where the calorimeter trigger was on. This gives a trigger efficiency for the calorimeter trigger of $(99.94 \pm 0.03)\%$. Similarly, the calorimeter trigger efficiency can be obtained from the events triggered by the scintillator multiplicity and muon trigger. The trigger efficiencies for Scintillator, TEC and muon trigger can be calculated by using the same method. Table A.2 lists each trigger efficiency. The efficiency of each trigger is calculated by combining this trigger with another independent trigger. The results are exactly the same from different combinations. The calorimeter trigger efficiency is $(99.94 \pm 0.03)\%$ for inclusive muon events and is larger than $(99.94 \pm 0.03)\%$ for inclusive electrons. For inclusive electron events, the TEC is required to be fully operational, hence the TEC trigger efficiency from inclusive electron events is higher than the one from inclusive muon events. The difference of the scintillator multiplicity trigger efficiency is due to two reasons: (a) the energy leakage of the electromagnetic shower; (b) the inclusive electron events are restricted in the barrel region compared to inclusive muon events. The inclusive dimuon events can be used to verify the trigger effi-

Trigger	efficiency of $\mu + X$	efficiency of $e + X$	combining with
Cal.	$(99.94 \pm 0.03)\%$	1.00	SCNT mult.
	$(99.94 \pm 0.03)\%$	1.00	TEC
	$(99.93 \pm 0.03)\%$	—	Muon
SCNT mult.	$(96.69 \pm 0.25)\%$	$(98.56 \pm 0.31)\%$	Cal.
	$(96.68 \pm 0.25)\%$	$(98.54 \pm 0.32)\%$	TEC
	$(96.49 \pm 0.27)\%$	—	Muon
TEC	$(97.84 \pm 0.20)\%$	$(98.49 \pm 0.32)\%$	Cal.
	$(97.82 \pm 0.20)\%$	$(98.47 \pm 0.32)\%$	SCNT mult.
	$(97.81 \pm 0.22)\%$	—	Muon
Muon	$(85.60 \pm 0.48)\%$	—	Cal.
	$(85.43 \pm 0.49)\%$	—	SCNT mult.
	$(85.58 \pm 0.49)\%$	—	TEC

Table A.2: *Trigger efficiencies determined from different combination for inclusive lepton events*

ciencies. From the trigger efficiencies and 213 inclusive dimuon events, 212.9 ± 0.4, 206.0 ± 2.6 and 208.4 ± 2.1 events would be triggered by calorimeter, scintillator multiplicity and TEC trigger respectively. Indeed, these numbers are the same as in the data (see Table A.1). This is not true for the muon trigger. The muon trigger has a higher efficiency for inclusive dimuon events compared to single muon events, because the muon trigger is designed to trigger dimuon events and it requires tight conditions for single muon events.

To check whether each trigger is really independent, the expected number of events triggered by combined triggers are compared with the number of events from the real data. The comparison is shown in Table A.3. The calculation agrees

Triggers	# of expected events	# of events
Cal.+SCNT+TEC	5035 ± 17	5033
Cal.+SCNT+Muon	4405 ± 28	4396
Cal.+TEC+Muon	4457 ± 27	4456
SCNT+TEC+Muon	4312 ± 29	4302
Cal.+SCNT+TEC+Muon	4310 ± 29	4300

Table A.3: *Comparison the number of events from real data and calculation*

perfectly with the number of observed events in the data. It means that each trigger can be treated as an independent trigger. Then the combined trigger efficiency is larger than 99.99% for both inclusive muon and inclusive electron events.

Bibliography

[1-1] UA1 Collaboration, G. Arnison *et al.*, Phys. Lett. **B 122** (1983) 103; Phys. Lett. **B 126** (1983) 398;
UA2 Collaboration, P. Bagnaia *et al.*, Phys. Lett. **B 129** (1983) 130;
UA2 Collaboration, R. Ansari *et al.*, Phys. Lett. **B 186** (1987) 440.

[1-2] S.L. Glashow, Nucl. Phys. **22** (1961) 579;
S.L. Glashow, J. Ilipoulos and L. Maiani, Phys. Rev. **D 2** (1970) 1285;
S. Weinberg, Phys. Rev. Lett. **19** (1967) 1264;
A. Salam and J.C. Ward, Phys. Lett. **13** (1964) 168;
A. Salam, "Elementary Particle Theory", edited by N. Svartholm (Almquist and Wiksell, Sockholm, 1968) 367.

[1-3] P.W. Higgs, Phys. Lett. **12** (1964) 132; Phys. Rev. Lett. **13** (1964) 508; Phys. Rev. **145** (1966) 1156;
F. Englert and R. Brout, Phys. Rev. Lett. **13** (1964) 321.

[2-1] R.P. Feynman, Rev. Mod. Phys. **20** (1948) 367; Phys. Rev. **74** (1948) 939, 1430; **76** (1949) 749, 769; **80** (1950) 440;
S. Tomonaga, Prog. Theor. Phys. **1** (1946) 27;
F.J. Dyson, Phys. Rev. **75** (1949) 468, 1736.

[2-2] C.N. Yang and R.L. Mills, Phys. Rev. **96** (1954) 191;
M. Gell-Mann, *Acta Physica Austriaca, Suppl.* **IX** (1072) 733;
H. Fritzsch and M. Gell-Mann, XVI International Conference on High Energy Physics, Batavia, Vol. II p.135 (1972);
H. Fritzsch, M. Gell-Mann and H. Leutwyler, Phys. Lett. **B 47** (1973) 365.

[2-3] See Reference [2-3].

[2-4] L3 Collab., B. Adeva *et al.*, Phys. Lett. **B 231** (1989) 509; **B 237** (1990) 136; **B 249** (1990) 341;
L3 Collab., B. Adeva *et al.*, Z. Phys. **C 51** (1991) 179;
ALEPH Collab., D. Decamp *et al.*, Phys. Lett. **B 231** (1989) 519; **B 235** (1990) 399; Z. Phys. **C 48** (1990) 365;
DELPHI Collab., P. Aarnio *et al.*, Phys. Lett. **B 231** (1989) 539;
DELPHI Collab., P. Abreu *et al.*, Phys. Lett. **B 241** (1990) 435;
OPAL Collab., M.Z. Akrawy *et al.*, Phys. Lett. **B 231** (1989) 530; **B 240**

(1990) 497; Z. Phys. **50** (1991) 373;
MARK II Collab., G.S. Abrams *et al.,* Phys. Rev. Lett. **63** (1989) 2173.

[2-5] Particle Data Group, G.F Bertsch *et al.,* Phys. Lett. **B 239** (1990) 1;
M. Consoli *et al.,* "Z Physics at LEP 1", edited by G. Altarelli *et al.,* CERN 89-08, Vol. 1, (1989) 7.
F. Mandl and G. Shaw, "Quantum Field Theory".

[2-6] J.H. Kühn *et al.,* "Z Physics at LEP 1", edited by G. Altarelli *et al.,* CERN 89-08, Vol. 1, (1989) 267.
J. Jersak, E. Laermann and P.M. Zerwas, Phys. Lett. **B 98** (1981) 363; Phys. Rev. **D 25** (1982) 1218.

[2-7] J.H. Kühn *et al.,* "Z Physics at LEP 1", edited by G. Altarelli *et al.,* CERN 89-08, Vol. 1, (1989) 267.
B.A Kniehl and J.H. Kühn, Phys. Lett. **B 224** (1989) 229.

[2-8] S. Gorishny, A.L Kataev and S.A. Larin, Phys. Lett. **B 259** (1991) 144.

[2-9] L3 Collab., B. Adeva *et al.,* Phys. Lett **B 248** (1990) 464; Phys. Lett **B 257** (1991) 469.

[2-10] D. Bardin *et al.,* Phys. Lett. **B 206** (1988) 539;
D. Bardin *et al.,* Berlin-Zeuthen preprint PHE-89-19 (1989).

[2-11] L3 Collab., B. Adeva *et al.,* Z. Phys. **C 51** (1991) 179.

[2-12] M. Böhm, W. Hollik *et al.,* "Z Physics at LEP 1", edited by G. Altarelli *et al.,* CERN 89-08, Vol. 1, (1989) 203.

[2-13] R.S. Orr, "Selected Topics in Electroweak Interactions", edited by J.M. Cameron *et al.,* Proc. 2th in Part. Phys., Lake Louise (1987) 1;
D.G. Hitlin, "Particles and Fields", edited by A.N. Kamal and F.C. Khanna, Proc. of the BSI, Banff Alberta (1988) Vol. 3, 607;
E691 Collab. J.R. Raab, *et al.,* Phys. Rev. **D 37** (1988) 2391;
CLEO Collab. S.C. Csorna, *et al.,* Phys. Lett. **B 191** (1987) 318;
ARGUS Collab. H. Albrecht, *et al.,* Phys. Lett. **B 210** (1988) 267;
Mark III Collab. R.M. Baltrusaitis, *et al.,* Phys. Rev. Lett. **54** (1985) 1976.

[2-14] N. Cabibbo and L. Maiani, Phys. Lett. **B 19** (1978) 109;
M. Suzuki, Nucl. Phys. **B 145** (1978) 420;
A. Ali and E. Pietarinen, Nucl. Phys. **B 145** (1979) 519.
C.S. Kim and A.D. Martin, Phys. Lett. **B 225** (1989) 186.

[2-15] M. Suzuki, Phys. Lett. **B 71** (1977) 139;
J.D. Bjorken, Phys. Rev. **D 17** (1978) 171;
V.A. Khoze, Ya.I. Azimov and L.L. Frankfurt, Proceedings, Conference on High Energy Physics, Tbilisi 1976.

[2-16] S. Bethke, Z. Phys. **C 29** (1985) 175;
J. Chrin, Z. Phys. **C 36** (1987) 163.

[2-17] B. Andersson, *et al.,* Phys. Rep. **97** (1983) 31;
G. Marchesini and B.R. Webber, Nucl. Phys. **B 310** (1988) 461;
R.D. Field and R.P. Feynman, Nucl. Phys. **B 136** (1978) 1.

[2-18] C. Peterson, *et al.,* Phys. Rev. **D 27** (1983) 105.

[2-19] T. Sjöstrand, *et al.,* "Z Physics at LEP 1", edited by G. Altarelli *et al.,* CERN 89-08, Vol. 3, (1989) 143.

[2-20] H. Schröder, Rep. Prog. Phys. **52** (1989) 765;
P.J. Franzini, Phys. Rep. **173** (1989) 1.
J.L. Rosner, Univ. of Chicago preprint, EFI 90-63, (1990).

[2-21] ARGUS Collaboration, H. Albrecht *et al.,* Phys. Lett. **B 192** (1987) 245;
CLEO Collaboration, M. Artuso *et al.,* Phys. Rev. Lett. **62** (1989) 2233;
UA1 Collaboration, G. Albajar *et al.,* Phys. Lett. **B 186** (1987) 237; **B 186** (1987) 247.

[3-1] LEP Design Report, Vol. I II, CERN-LEP/84-01, June 1984.

[3-2] Ian Wilson and Heino Henke, "The LEP Main Ring Accelerating Structure", CERN 89-09 (1989).

[3-3] R. Bailey *et al.,* "LEP Energy Calibration", CERN SL/90-95 (1990).

[4-1] L3 Collaboration, B. Adeva *et al.,* "The Construction of the L3 Experiment", **NIM A 289** (1990) 35, and the references therein.
L3 Technical Proposal to CERN-LEPC (May 1983).

[4-2] ALEPH Collab. D. Decamp *et al.,* "ALEPH: A Detector for Electron-Positron Annihilations at LEP", **NIM A 294** (1990) 121;
DELPHI Collab. P. Aarnio *et al.,* "The DELPHI Detector at LEP", **NIM A 303** (1991) 233;
OPAL Collab. M.Z.Akrawy *et al.,* "The OPAL Detector at LEP", **NIM A 305** (1991) 275.

[4-3] D.N. Ren, "The L3 Vertex Chamber Development and Infrastructure", thesis, Swiss Federal Institute of Tech. Zurich (1990).

[4-4] J.A. Bakken *et al.,* "Performance of A prototype BGO Calorimeter in An Electron Beam from 2 to 50 GeV ", **NIM A 254** (1987) 535;
M. Schneegans, "Progress of the L3/BGO Calorimeter", **NIM A 257** (1987) 528.

[4-5] Yu. Galaktionov *et al.*, "The Performance of A Uranium Gas Sampling Calorimeter", **NIM A 251** (1986) 258;
A. Arefiev *et al.*, "A Detailed Study of the Performance of the Uranium-Gas Sampling Calorimeter", **NIM A 285** (1989) 403;
B. Bleichert *et al.*, "Test Results from A Uranium Hadron Calorimeter Using Wire Chamber Readout", **NIM A 254** (1987) 529;
H. Martyn and J.F. Zhou, "Monte Carlo Simulation of A Uranium Calorimeter with Proportional Chamber Readout", **NIM A 256** (1987) 143;
A. Arefiev *et al.*, "Analysis and Simulation of Hadronic Showers in A Uranium Gas-Sampling Calorimeter", **NIM A 288** (1990) 364;
O. Adriani *et al.*, "Hadronic Calorimetry in the L3 Detector", **NIM A 302** (1991) 53.

[4-6] S. Burov *et al.*, CERN-EP/88-84, March (1988), submitted to NIM.

[4-7] B. Adeva *et al.*, "Muon Detection in the L3 Experiment at LEP", **NIM A 277** (1989) 187;
Y. Peng, "The Muon Spectrometer of the L3 Detector at LEP", thesis, Univ. of Amsterdam (1988);
J. Onvlee, "The Behaviour of the L3 Muon Chambers in a Magnetic Field", thesis, Univ. of Amsterdam (1989).

[4-8] R. Bizzarri *et al.*, **NIM A 283** (1989) 799;
M. Fukushima, "L3 Level-1 Muon Trigger", L3 notes # 515 (1987);
T.S. Dai and M. Fukushima, "Level 1 Muon Trigger Schematics" L3 notes # 668, May (1989);
J. Perrier, "Level 1 TEC Trigger" L3 notes # 622, Nov. (1988);
M. Bourquin *et al.*, **NIM A 306** (1991) 151.

[5-1] L3 Collab. B. Adeva *et al.*, **Phys. Lett. B 249** (1990) 341; Z. Phys. **C 51** (1991) 179.

[5-2] O. Adriani *et al.*,, **NIM A 302** (1991) 53.

[6-1] L3 Collab. B. Adeva *et al.*, Phys. Lett. **B 259** (1991) 199;
MARK II Collab. G.S. Abrams *et al.*, Phys. Rev. Lett. **64** (1990) 1334;
ALEPH Collab. D. Decamp *et al.*, Phys. Lett. **B 234** (1990) 209;
DELPHI Collab. P. Aarnio *et al.*, Phys. Lett. **B 240** (1990) 271;
DELPHI Collab. P. Abreu *et al.*, Z. Phys. **C 50** (1991) 185;
OPAL Collab. M.Z. Akrawy *et al.*, Z. Phys. **C 47** (1990) 505;
OPAL Collab. G. Alexander *et al.*, Phys. Lett. **B 264** (1991) 467.

[6-2] Y.J. Pei, L3 notes. #838 (1990), unpublished.

[6-3] T. Sjöstrand and M. Bengtsson, Comput. Phys. Commun. **43** (1987) 367;
See Reference [2-19].

[6-4] See Reference [2-18].

[6-5] L3 Collaboration, B. Adeva *et al.,* Phys. Lett. **B 241** (1990) 416.

[6-6] GEANT Version 3.13, September 1989; See R. Brun *et al.*, GEANT 3, CERN report DD/EE/84-1 (Revised) (Sept. 1987);
H. Fesefeldt, RWTH Aachen Preprint PITHA 85/02 (1985).

[6-7] For the experimental results see: J. Chrin, Z. Phys. **C 36** (1987) 163.

[6-8] The semileptonic branching ratios are taken from PEP and PETRA data. See JADE Collaboration, W. Bartel *et al.,* Z. Phys. **C 33** (1987) 339, and references therein.

[6-9] KORALZ, S. Jadach *et al.*, "Z Physics at LEP 1", edited by G. Altarelli, R. Kleiss and C. Verzegnassi, CERN Report 89-08, Vol.III, 69, to be published in Comp. Phys. Comm..

[6-10] M. Böhm, A. Denner and W. Hollik, Nucl. Phys. **B 304** (1988) 687;
F.A. Berends, R. Kleiss and W. Hollik, Nucl. Phys. **B 304** (1988) 712.

[6-11] F.A. Berends, P.H. Daverveldt and R. Kleiss, Nucl. Phys. **B 253** (1985) 441.
F.A. Berends, P.H. Daverveldt and R. Kleiss, Comp, Phys. Com. **40** (1986) 285.

[6-12] D. Bardin *et al.*, Nucl. Phys. **B 351** (1991) 1;
D. Bardin *et al.*, Z. Phys. **C 44** (1989) 493;
D. Bardin *et al.*, Phys. Lett. **B 255** (1991) 290;
M. Bilenky and A. Sazonov, JNIR Dubna preprint E2-89-792 (1989) unpublished.

[6-13] L3 Collab. B. Adeva *et al.,,* Phys. Lett. **B 250** (1990) 183; Z. Phys. **C 51** (1991) 179;
J. Alcaraz and T.S. Dai, "Muon trigger efficiency for the $\mu\mu(\gamma)$ sample", L3 notes, # 947 (1991).

[7-1] T.S. Dai and T. Foreman, " Determination of the Muon Chamber Efficiency in the 1990 Data", L3 note #954 (1990);
J.M. Qian, "Study of Muon Pair Production at LEP", thesis, MIT (1990).

[7-2] Y.J. Pei, " TEC Efficiency in the 1990 Data", L3 note #954 (1991);
J.C. Sens, L3 notes #997 (1991); L3 notes L3 notes #998 (1991).

[8-1] See Reference [2-11].

[8-2] F. James and M. Roos, "MINUIT Function Minimization and Error Analysis", CERN, **D506** (1989) 1.

[8-3] A.G. Frodesen *et al.,* "Probability and Statistics in Particle Physics", Universitesforlaget (1979) 195.

[8-4] See Reference [6-7].

[8-5] See J.J. Hernöndez *et al.*, Review of Particle Properties 1990, Phys. Lett **B 239** (1990) 1, pages VII.112-113 and VII.134. The measurements are averaged according to the procedure used by the Particle Data Group.

[8-6] CLEO Collaboration, D. Bortoletto *et al.*, Phys. Rev. Lett **63** (1989) 1667; R. Fulton *et al.*, CLNS 90/989 (August 1990).

[8-7] B. Grinstein and M.B. Wise, Phys. Lett **B 197** (1987) 249;
N. Isgur, D.Scora, B. Grinstein and M.B. Wise, Phys. Rev. Lett **D 39** (1989) 799.

[8-8] CUSB Collaboration, K. Han *et al.*, Phys. Rev. Lett **55** (1985) 36.

[8-9] MAC Collab. B. Fernandez *et al.*, Phys. Rev. Lett. **50** (1983) 2054;
MARK II Collab. M.E. Nelson *et al.*, Phys. Rev. Lett. **50** (1983) 1542; R.A. Ong *et al.*, Phys. Rev. Lett. **60** (1988) 2587;
MARK J Collab. B. Adeva *et al.*, Phys. Rev. Lett. **51** (1983) 443; Phys. Rep. **109, Nos. 3&4** (1984) 131;
CELLO Collab. H. Behrend *et al.*, Z. Phys. **C 19** (1983) 291;
TASSO Collab. M. Althoff *et al.*, Z. Phys. **C 22** (1984) 219; Phys. Lett. **B 146** (1984) 443;
TPC Collab. H. Aihara *et al.*, Phys. Rev. **D 31** (1985) 2719; Z. Phys. **C 27** (1985) 39;
DELCO Collab. T. Pal *et al.*, Phys. Rev. **D 33** (1986) 2708;
JADE Collab. W. Bartel *et al.*, Z. Phys. **C 33** (1987) 339.

[8-10] D. Bardin, *et al.*, Berlin-Zeuthen preprint PHE-89-19 (1989);
See also: J.E. Campagne and R. Zitoun, Z. Phys. **C 43** (1989) 469.

[8-11] L3 Collab., B. Adeva *et al.*, L3 preprint #32 (1991), submitted to Phys. Lett **B.**

[8-12] ARGUS Collab., H. Albrecht *et al.*, Phys. Lett **B 249** (1990) 359;
J.C. Gabriel, Ph.D. Thesis, Univ. of Heidelberg, IHEP-HD/89-1 (1989).

[8-13] G. Altarelli, *et al.*, Nucl. Phys. **B 208** (1982) 365.

[8-14] L3 Collab., B. Adeva *et al.*, Phys. Lett **B 248** (1990) 464; Phys. Lett **B 257** (1991) 469.

[8-15] CLEO Collab., S.J. Behrends *et al.*, Phys. Rev. Lett **59** (1987) 407;
CLEO Collab., R. Fulton *et al.*, Phys. Rev. Lett **64** (1990) 16;
ARGUS Collab., H. Albrecht *et al.*, Phys. Lett **B 255** (1991) 297.

[8-16] Particle Data Group, Phys. Lett. **B 239** (1990) III.62.

[8-17] A. Djouadi, J.H. Kühn and P.M. Zerwas, Z. Phys. **C 46** (1990) 411.

[9-1] A. Pais, S.B. Treiman, Phys. Rev. **D 12** (1975) 2744;
J. Ellis., M.K. Gaillard, D.V. Nanopoulos, Nucl. Phys. **B 109** (1976) 213;
P.J. Franzini, Phys. Rep. **173** (1989) 1.

[9-2] See Reference [2-21]

[9-3] P.J. Franzini, Phys. Rep. **173** (1989) 1;
K. Kleinknecht and B. Renk, Z. Phys. **C 34** (1987) 209.

[9-4] Particle Data Group, Phys. Lett. **B 239** (1990) III.35.

[9-5] See Reference [8-11].

[10-1] P. Roudeau, talk at Lepton Photon Conference, LP-HEP91, July 1991, Geneva, Switzerland.
P. Wells, talk at 4th International Symposium on Heavy Flavor Physics, June 1991, Orsay, France.
P. Dornan, talk at 4th International Symposium on Heavy Flavor Physics, June 1991, Orsay, France.

[10-2] ALEPH Collab. D. Decamp *et al.*, Phys. Lett. **B 244** (1990) 551; Phys. Lett. **B 258** (1991) 236; Phys. Lett. **B 263** (1991) 325.

[10-3] OPAL Collab. M.Z. Akrawy *et al.*, Phys. Lett. **B 263** (1991) 311.

[10-4] Mark II Collab. G.S. Abrams *et al.*, Phys. Rev. Lett. **64** (1990) 1211;
UA1 Collab. C.Albajar *et al.*, CERN preprint CERN-PPE/91-55, March 18, 1991, submitted to Phys. Lett. B.

Figure Captions

Fig. 4-2 The Central Track Detector (TEC) (a) General view; (b) Wire configuration.

Fig. 4-3 (a) Longitudinal cut through the BGO electromagnetic calorimeter. (1) the barrel, (2) the endcap, (3) FTC. The endcap and FTC were not installed at the time of this study; (b) Cross sectional view of a BGO crystal.

Fig. 4-4 The view of the Hadron Calorimeter, (a) Longitudinal view; (b) Perspective view.

Fig. 4-5 (a) Perspective view of an octant of the muon system;
(b) Schematic view of the chambers in an octant and the laser beacon system;
(c) Illustration of the measurement of the sagitta in the muon system from the centroid positions of the track in the three chamber layers.

Fig. 4-6 The Luminosity Monitor, (a) side view; (b) end view of the BGO crystal array.

Fig. 6-1 An inclusive lepton event recorded at L3 detector, there are two leptons, one muon and one electron. Both figures show the $R-\phi$ projection of the event. The muon is passing through three layers of chambers, as shown in upper figure. The lower figure shows a close-up view in the BGO calorimeter and TEC chamber. The electron candidate is the large cluster in the BGO, and has only one track associated with it and no energy in the hadron calorimeter behind this electron candidate. The muon has a momentum of 17 GeV and 1.7 GeV in $p_\perp$, the electron has an energy of 14 GeV and 2.7 GeV in $p_\perp$. The sign of both lepton charges is positive.

Fig. 6-2 Sources of inclusive leptons (See page 35).

Fig. 6-3 The energy distribution for $e^+e^- \rightarrow hadrons$: (a) visible energy fraction; (b) energy in the calorimeter; (c) transverse energy imbalance; (d) longitudinal energy imbalance, are compared with the same distribution for Monte Carlo events of $Z^0 \rightarrow q\bar{q}$. The low energy events are mainly from the two photon process and beam gas and are not simulated in figure (a) and (b). In these figures all hadronic selection cuts are imposed, except the cut on the variable plotted.

Fig. 6-4 Number of clusters reconstructed in the calorimeters for hadronic events (a) barrel region, (b) EndCap region, are compared with the same distributions for Monte Carlo signal of $Z^0 \rightarrow q\bar{q}$. The dilepton events and two photon process events are the main sources of low multiplicity events and are not included in the plots. In the figure all hadronic selection cuts are imposed, except the cut on the variable plotted.

Fig. 6-5 The reconstructed distance of closest approaches and their relative errors, (a) R in the $R-\phi$ plane; (b) Z in the $R-Z$ plane; (c) R/σ_R; (d) Z/σ_Z, of muons from $e^+e^- \rightarrow \mu\nu + X$ process, where the σ is define as the associated error . of DCA. In the figures all selection cuts are imposed, except the cut on the variable plotted.

Fig. 6-6 The angular distributions in (a) ϕ and (b) θ of the selected inclusive muon events.

Fig. 6-7 The E_9/E_{25} distribution in the BGO calorimeter compares with Monte Carlo distribution for (a) the electron candidates of inclusive electron events, where all the selection cuts are imposed, except the cut on the variable plotted; (b) the electron candidates of $e^+e^- \rightarrow e^+e^-(\gamma)$ events. The E_9/E_{25} is centered at 1.01 with a width about 1%. Because the energy correction for 3×3 crystals is not the same as the energy correction for 5×5 crystals, the value of E_9/E_{25} can be larger than 1.

Fig. 6-8 The $\Delta\phi$ distributions, which is the difference of the azimuthal angle between the centroid of the electromagnetic shower and a track in the TEC. (a) Average $\Delta\phi$ in the measured the azimuthal angle ϕ. The curve shows the correction function from a fit. The data point at 3 rad is far away from the fitted curve because the TEC sector 12 was broken. (b) Average $\Delta\phi$ in ϕ after correction applied. (c) The $\Delta\phi$ distribution after correction applied, which centered near zero. In the figure all selection cuts are imposed, except the cut on the variable plotted. The Monte Carlo didn't simulate data very well, but data and Monte Carlo are in agreement at large $\Delta\phi$ ($\Delta\phi > 4\ mrad$).

Fig. 6-9 The ratio of the energy measured in the BGO and the signed momentum measured in the TEC (qE/p) for electron candidates, (a) the tracks around the anode and cathode planes are removed; (b) all the tracks. The low values of E/p is from the charged particles which deposit a fraction of energy in the BGO, and the tails at large values of E/p are due to energetic photons and π^0's that have a nearby charged track.

Fig. 6-10 The distributions of opening angle between muon and (i) thrust axis; (ii) jet axis, the muon momentum included in the jet; (iii) jet axis, the muon momentum excluded from the jet; (iv) original hadrons. The angular distribution in (ii) is similar as (iv).

Fig. 6-11 The distributions of the $\Delta p_\perp$, the difference between the $p_\perp$ with respective to the original hadrons and the $p_\perp$ with respective to, (a) the thrust axis; (b) the jet axis, the muon momentum included in the jet; (c) the jet axis, the muon momentum excluded from the jet.

Fig. 6-12 Without $p_\perp$ cut, the measured (a) muon momentum and (b) electron energy distributions of inclusive lepton events are compared to the same

direction is estimated by the thrust axis of the event. The solid curve plots the expected distribution for $A_{b\bar{b}}^{obs} = 0.82$. In the fit, acceptance correction was not applied.

Fig. 8-4 The nearest jet energy distributions are compared with the same distributions of the Monte Carlo simulation, where in defining the jet direction the measured muon momentum are (a) first excluded from jet and (b) included in the jet.

Fig. 8-5 The muon transverse momentum with respect to the nearest jet, where the measured muon momentum are (a) excluded from jet and (b) included in the jet to calculate the jet axis. The distributions are compared with the prediction of Monte Carlo.

Fig. 8-6 The comparison of the V_{cb} and V_{ub} measurement with those from ARGUS/CLEO. The solid curve is derived from this measurement of b quark semileptonic branching ratio and the L3 b hadron life measurement, and the solid line is the ARGUS/CLEO measurement of $|V_{ub}/V_{cb}|$. The dashed curves and line corresponding to the one standard deviation limits including the theoretical uncertainties.

Fig. 9-1 The distributions of the minimum momenta of the two leptons in the opposite hemisphere, (a) like-sign dileptons; (b) unlike-sign dileptons, are compared the Monte Carlo prediction with $\chi_B = 0$. No $p_\perp$ cut has been applied.

Fig. 9-2 The distributions of the minimum transverse momentum of the two leptons in the opposite hemisphere, (a) like-sign dileptons; (b) unlike-sign dileptons, are compared the Monte Carlo prediction with $\chi_B = 0$. In the large $p_\perp$ region, there are more like-sign dilepton events in the data than those in the Monte Carlo.

Fig. 9-3 The distributions of the minimum momenta of the two leptons in the opposite hemisphere are compared with Monte Carlo predictions (a) with $\chi_B = 0$; (b) with $\chi_B = 0.178$. The predictions of the Monte Carlo for the various sources are shown also. From (a), clearly there is an excess of like-sign dilepton events, thus a clear evidence for B^0-$\bar{B}^0$ mixing.

Fig. 9-4 The plot of χ_d versus χ_s for the measured $\chi_B = f_d\chi_d + f_s\chi_s$, assuming $f_d = 0.375$ and $f_s = 0.15$. The dashed lines indicating the $\pm 1\sigma$ bands. The same is shown for the ARGUS/CLEO measurements. The hatched region is allowed by the Standard Model.

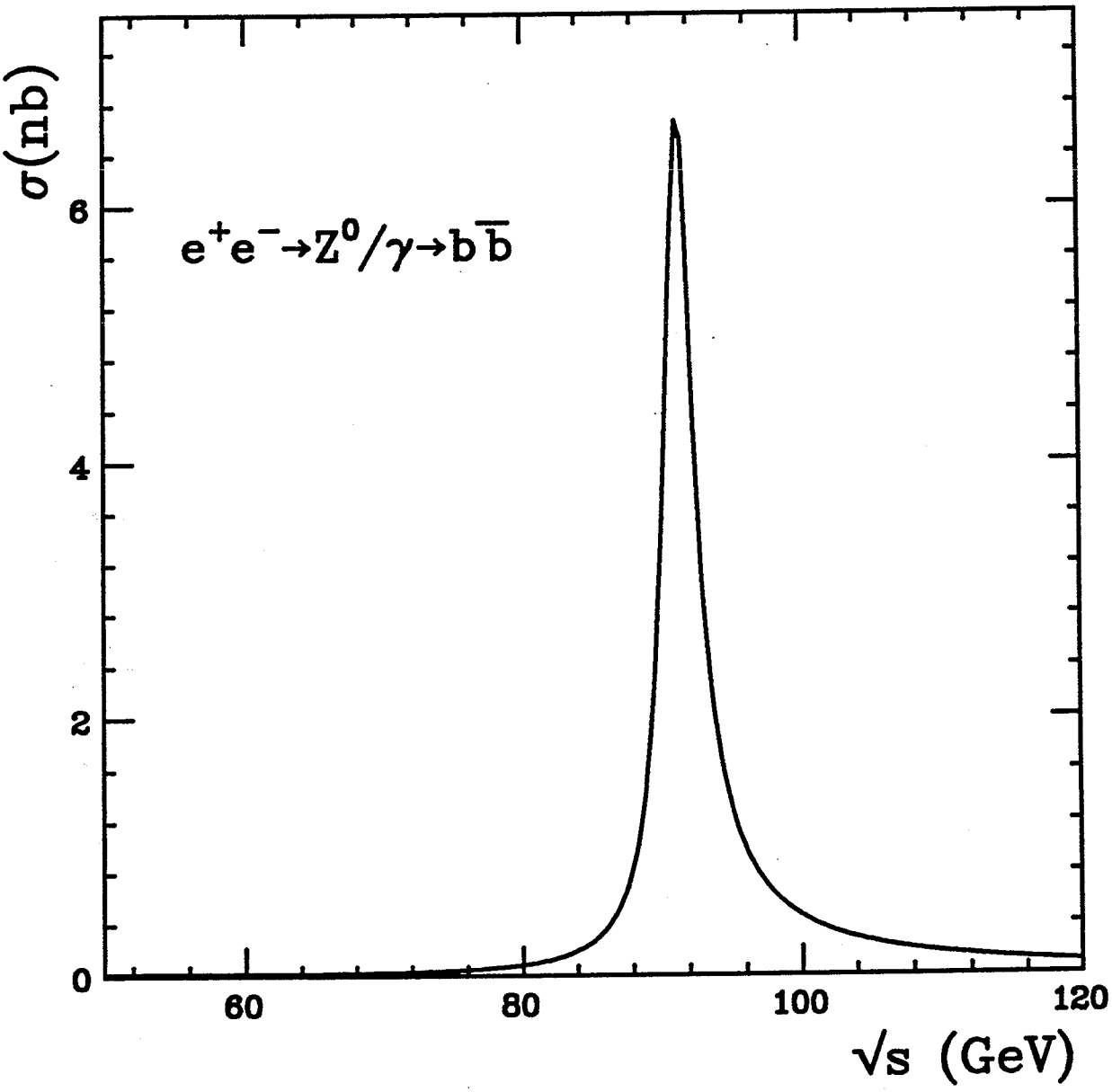

Figure 1-1: $\sqrt{s}$-dependence of the cross section of $e^+e^- \rightarrow b\bar{b}$ with radiative and electroweak corrections predicted by the Standard Model.

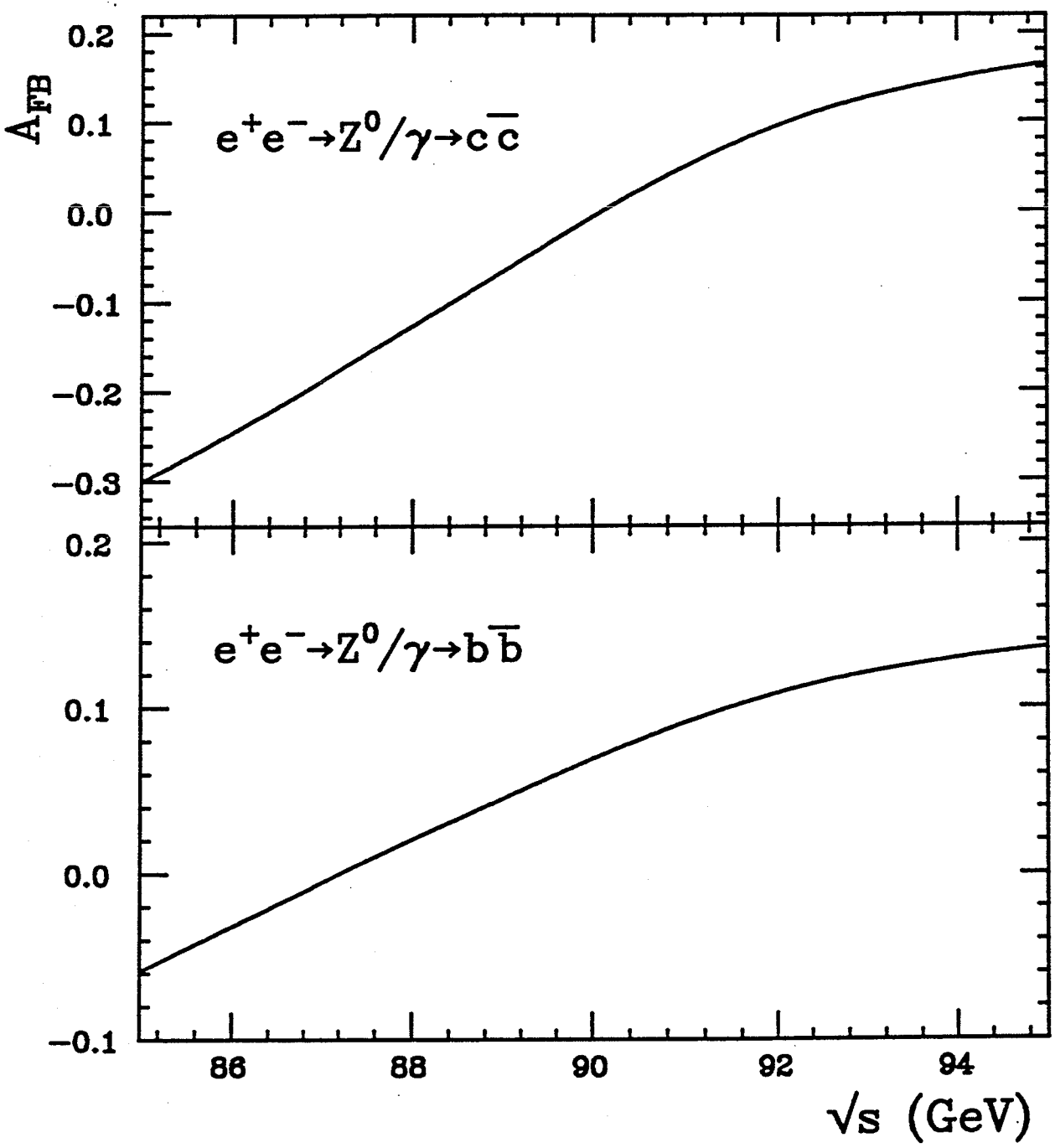

Figure 2-3: $\sqrt{s}$-dependence of the forward-backward asymmetry for heavy flavor production, where the radiative, electroweak and QCD corrections included.

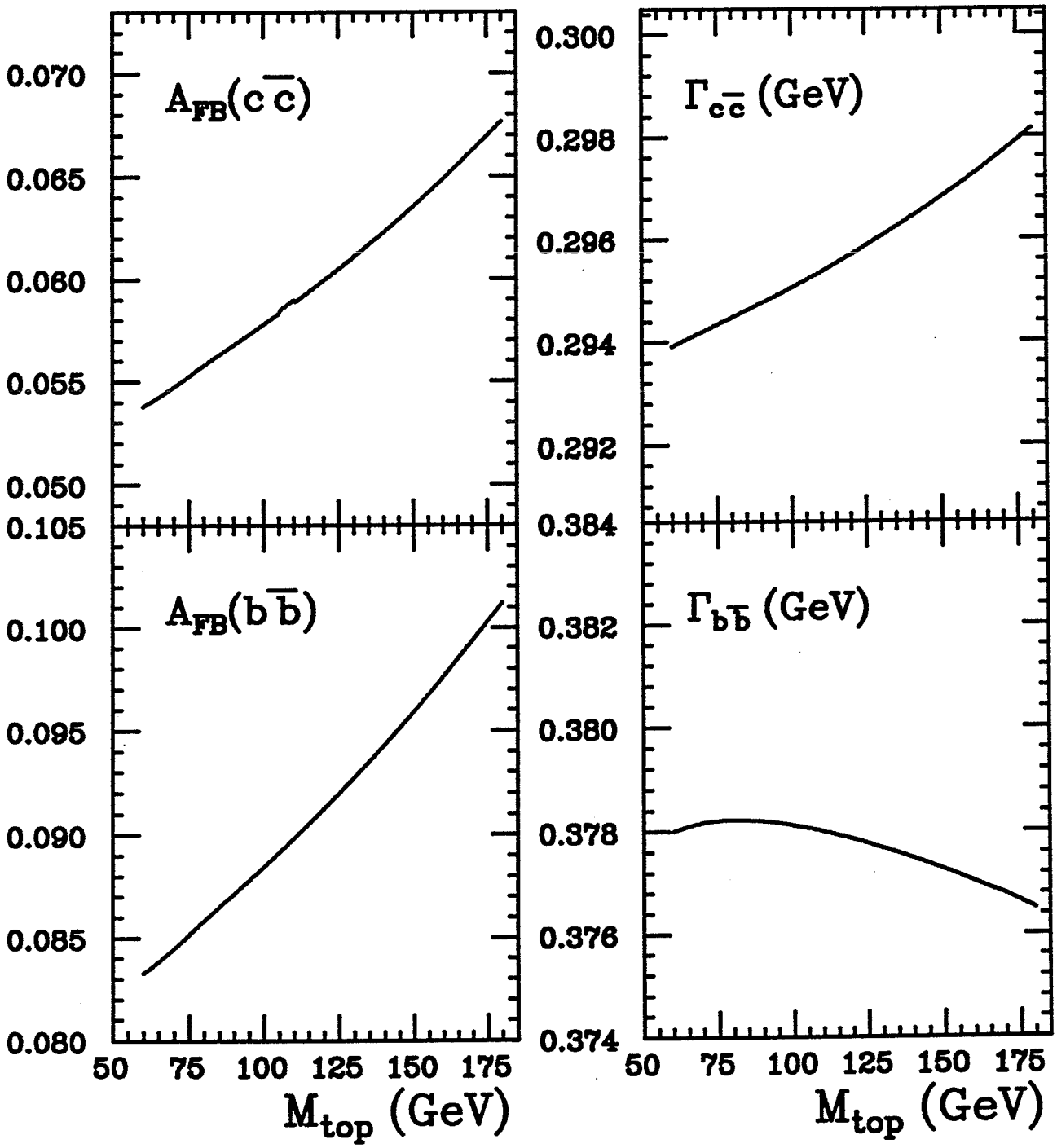

Figure 2-4: The dependence of the partial decay widthes (right) and of the forward-backward asymmetry (left) on the top mass, where the radiative, electroweak and QCD corrections included.

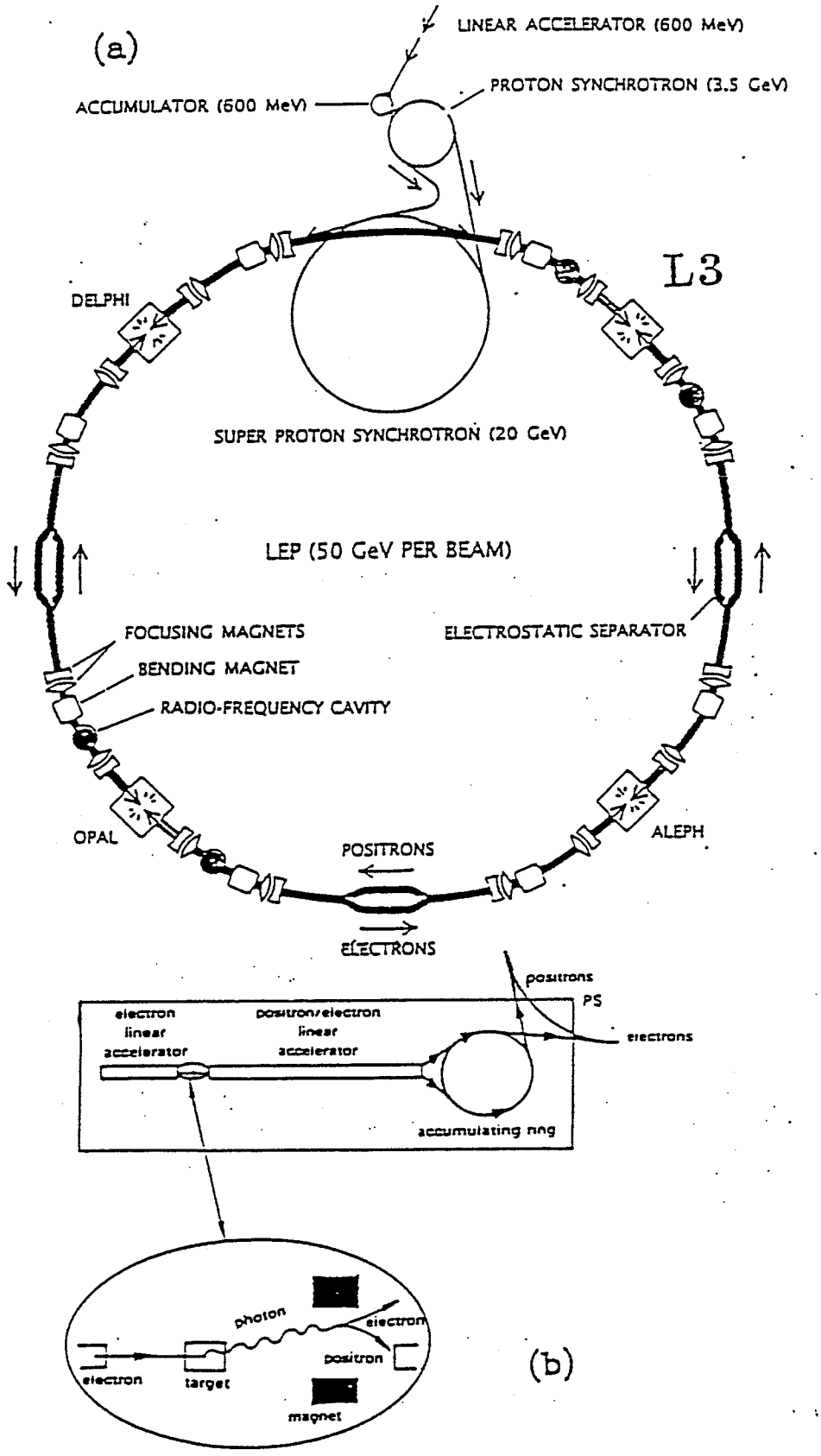

Figure 3-1: A schematic view of LEP collider, (a) LEP injection chain and the LEP ring where four LEP detectors are installed; (b) the LEP pre-injection chain.

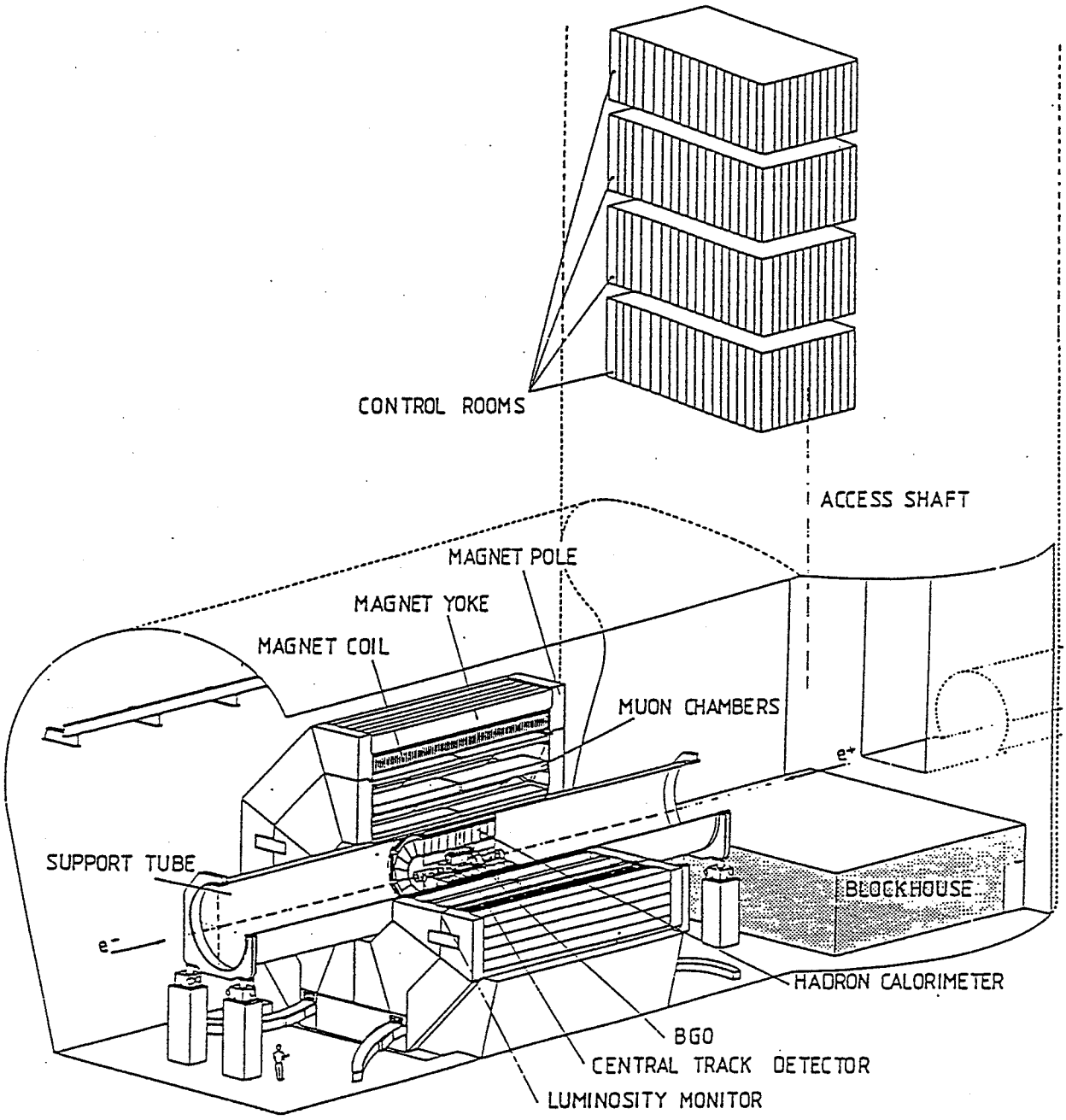

Figure 4-1: (a) General view of the L3 detector.

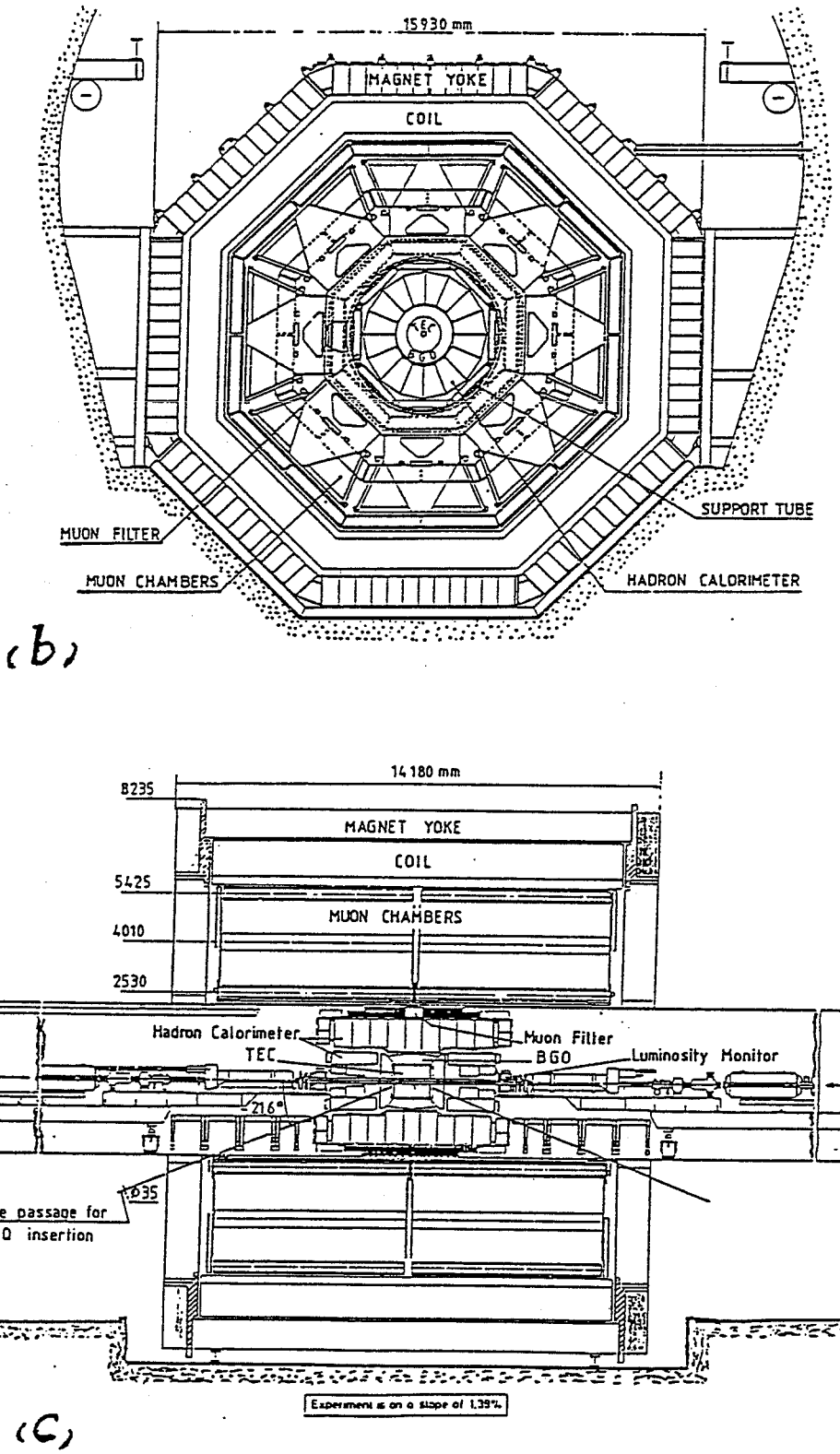

Figure 4-1: (b) End view of the L3 detector; (c) Side view of the L3 detector.

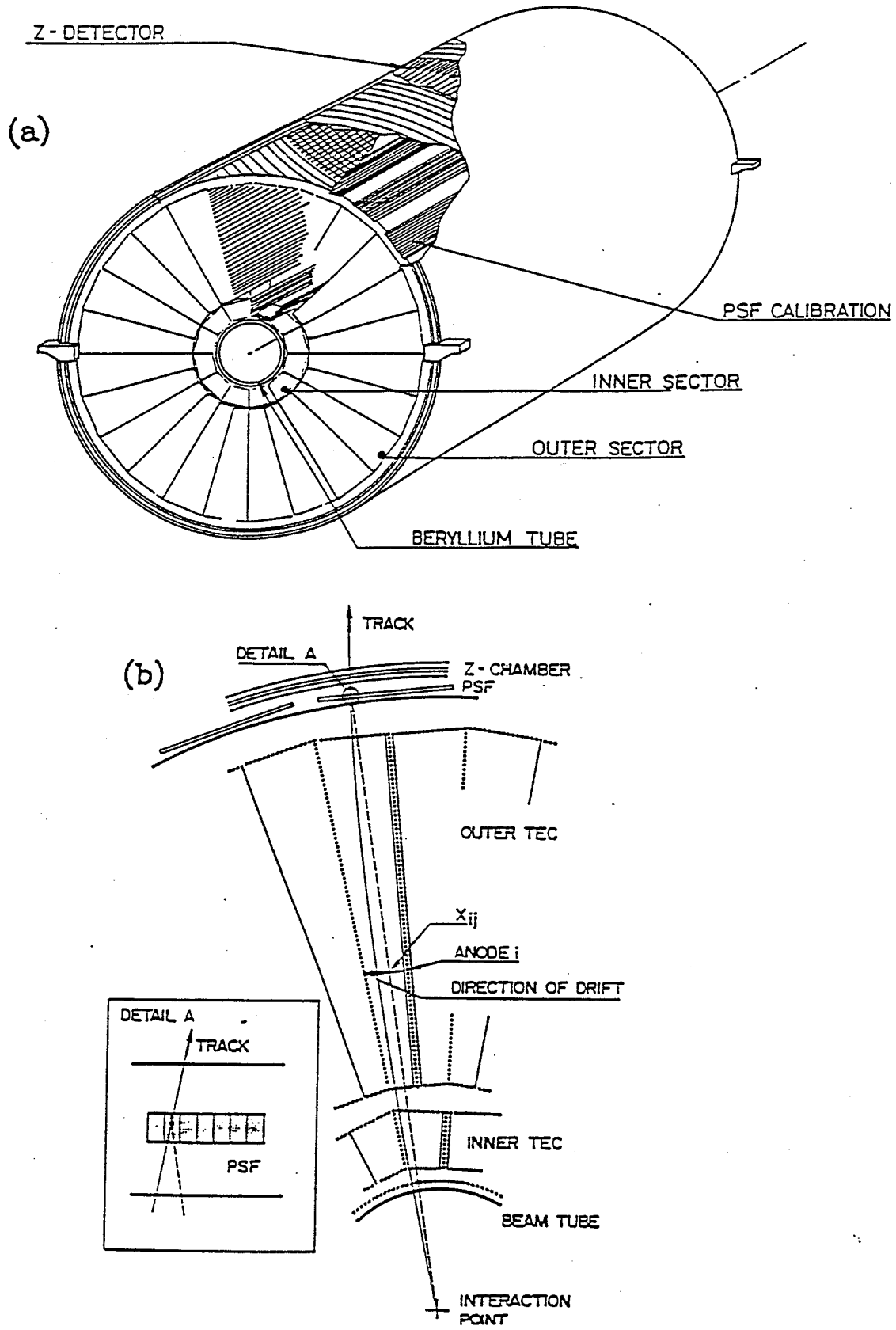

Figure 4-2: The Central Track Detector (a) General view; (b) Wire configuration.

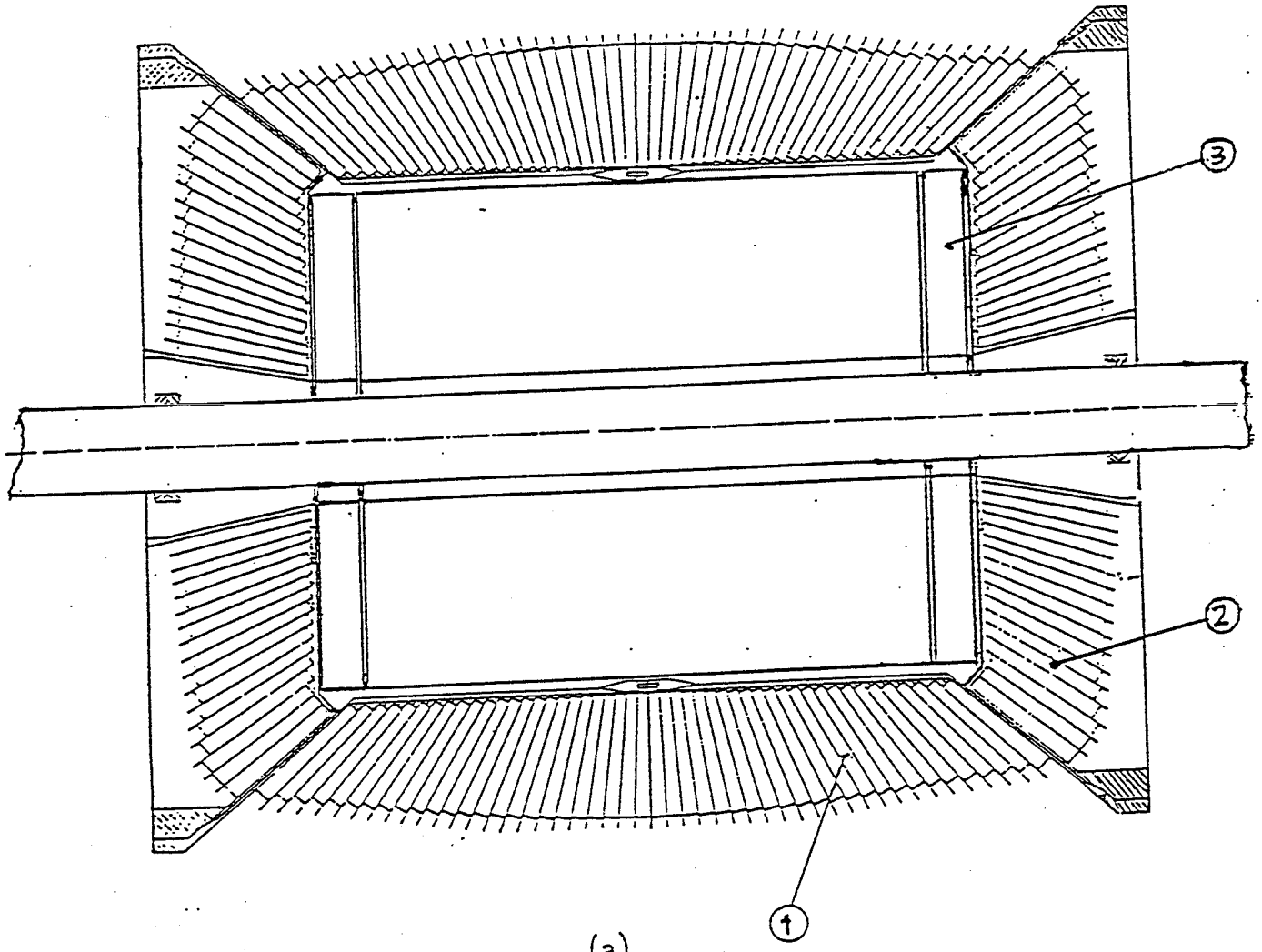

(a)

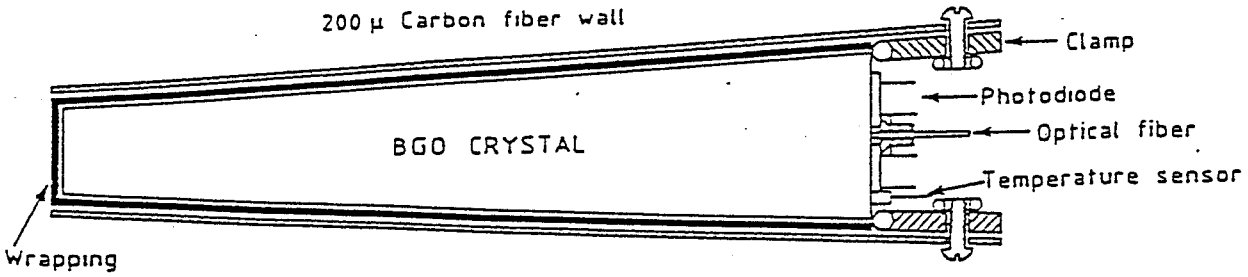

(b)

Figure 4-3: (a) Longitudinal cut through the BGO electromagnetic calorimeter; (b) Cross sectional view of a BGO crystal.

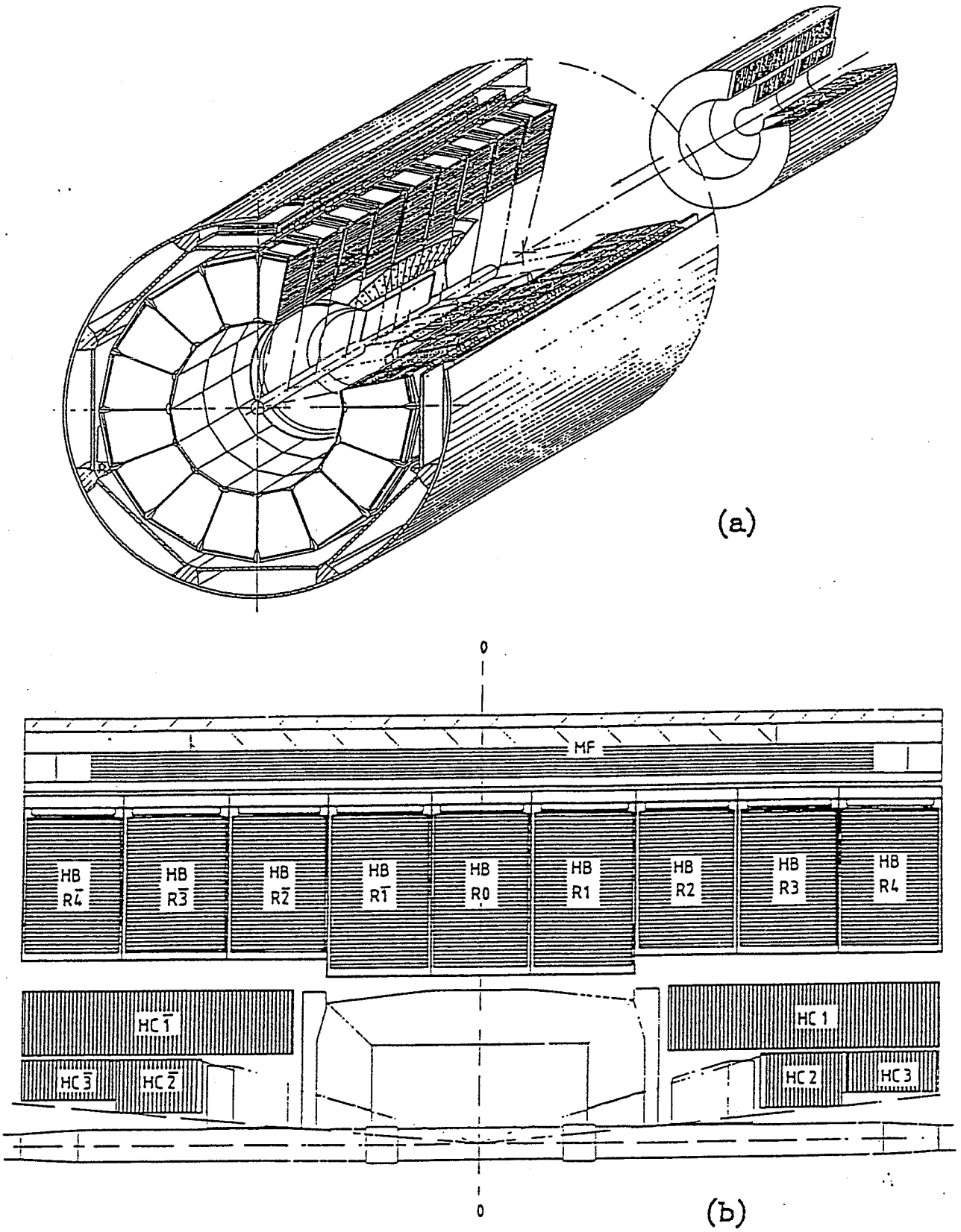

Figure 4-4: The view of the Hadron Calorimeter, (a) Longitudinal view; (b) Perspective view.

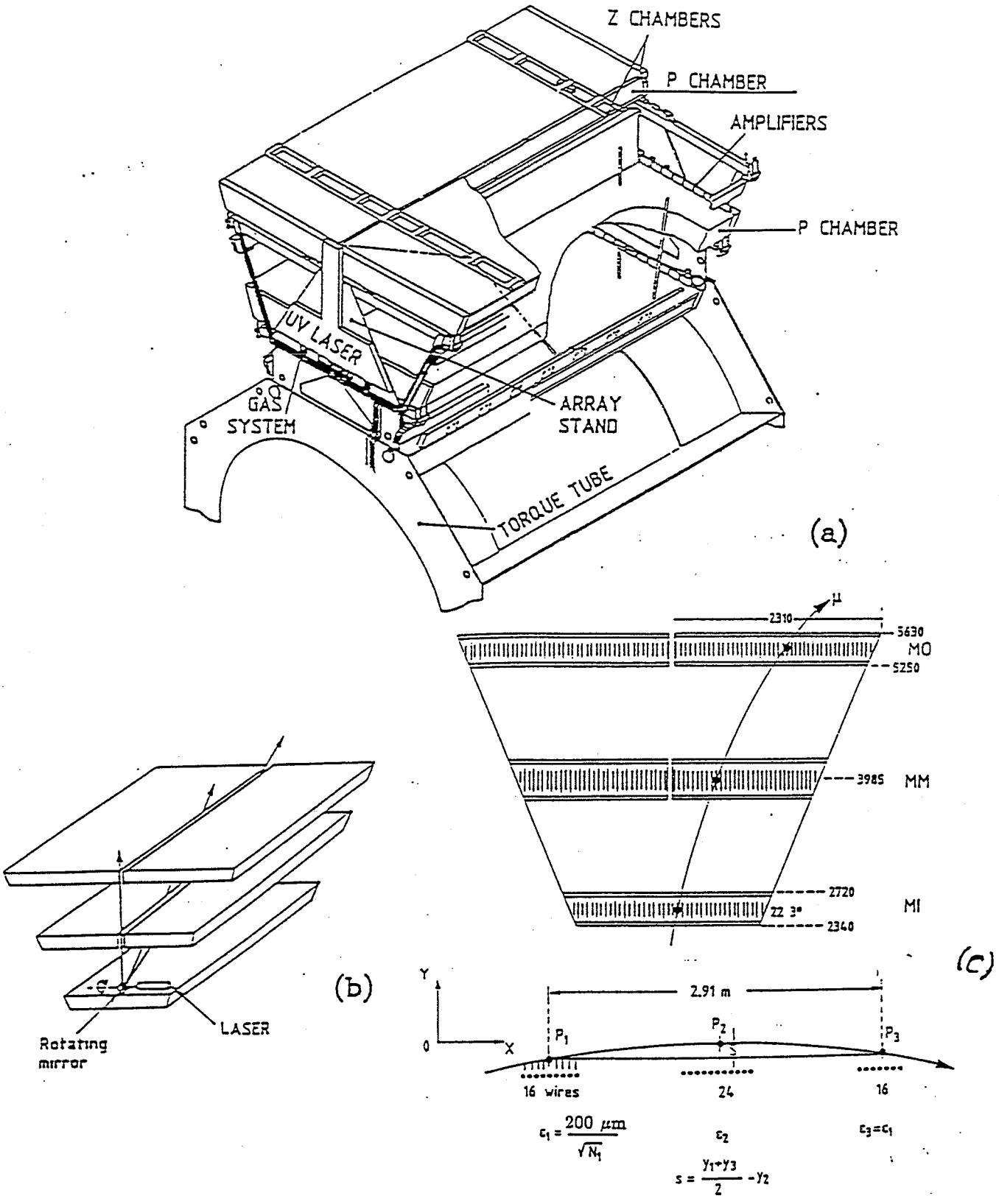

Figure 4-5: (a) Perspective view of an octant of the muon system; (b) The view of the laser beacon system; (c) Illustration of the measurement of the sagitta.

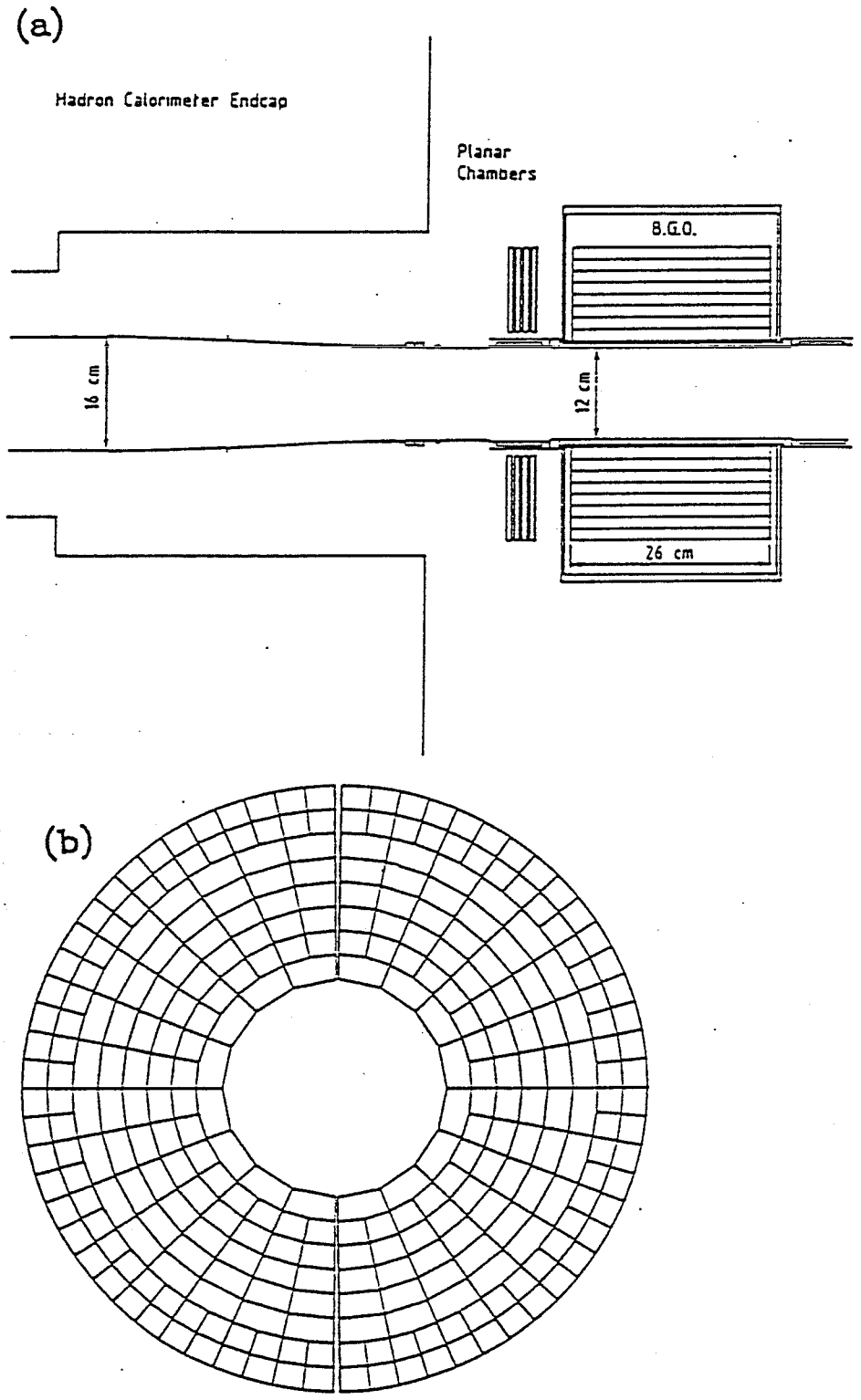

Figure 4-6: Luminosity Monitor (a) side view; (b) end view of the BGO crystal array.

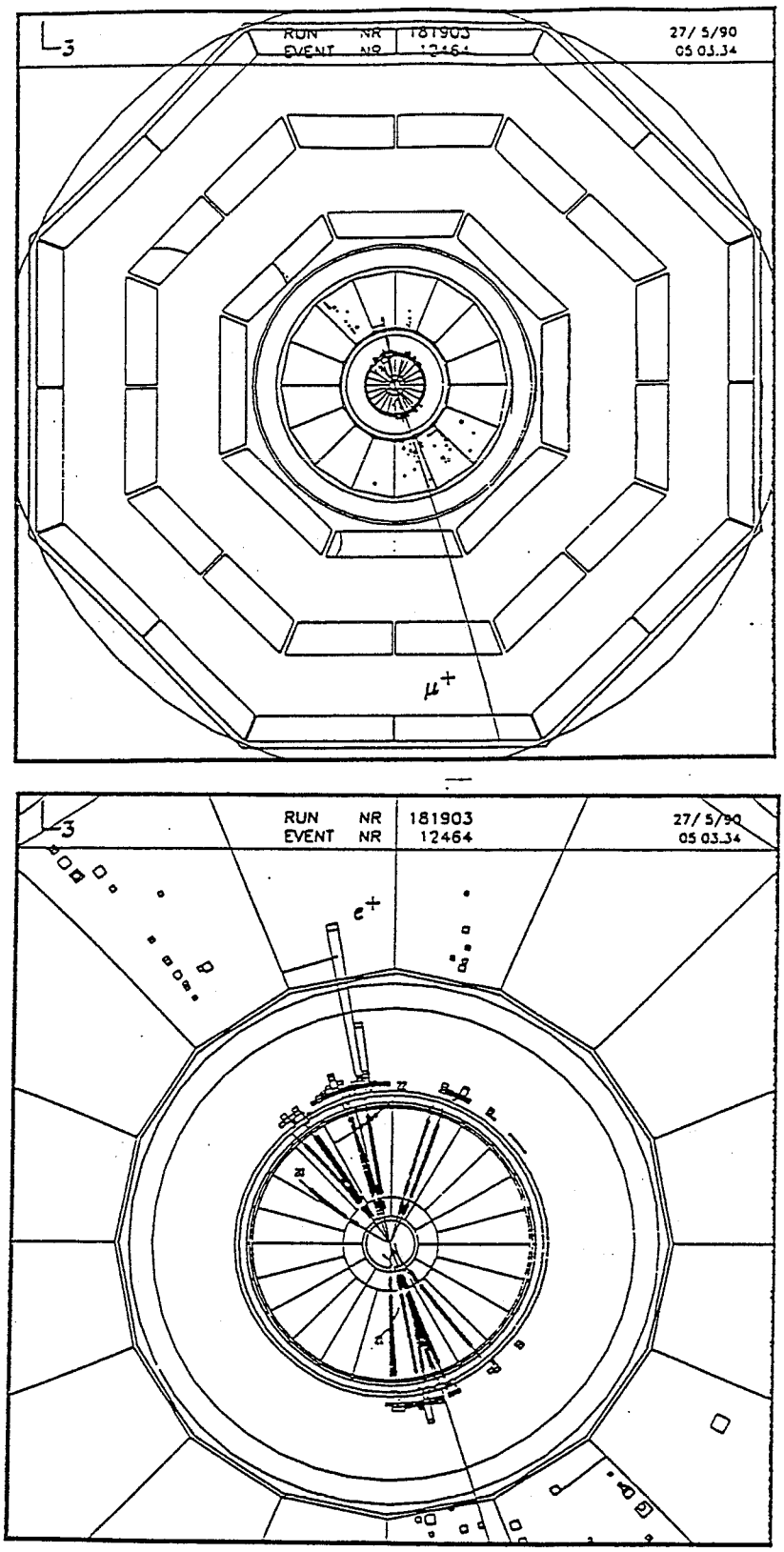

Figure 6-1: An inclusive lepton event recorded at L3 detector.

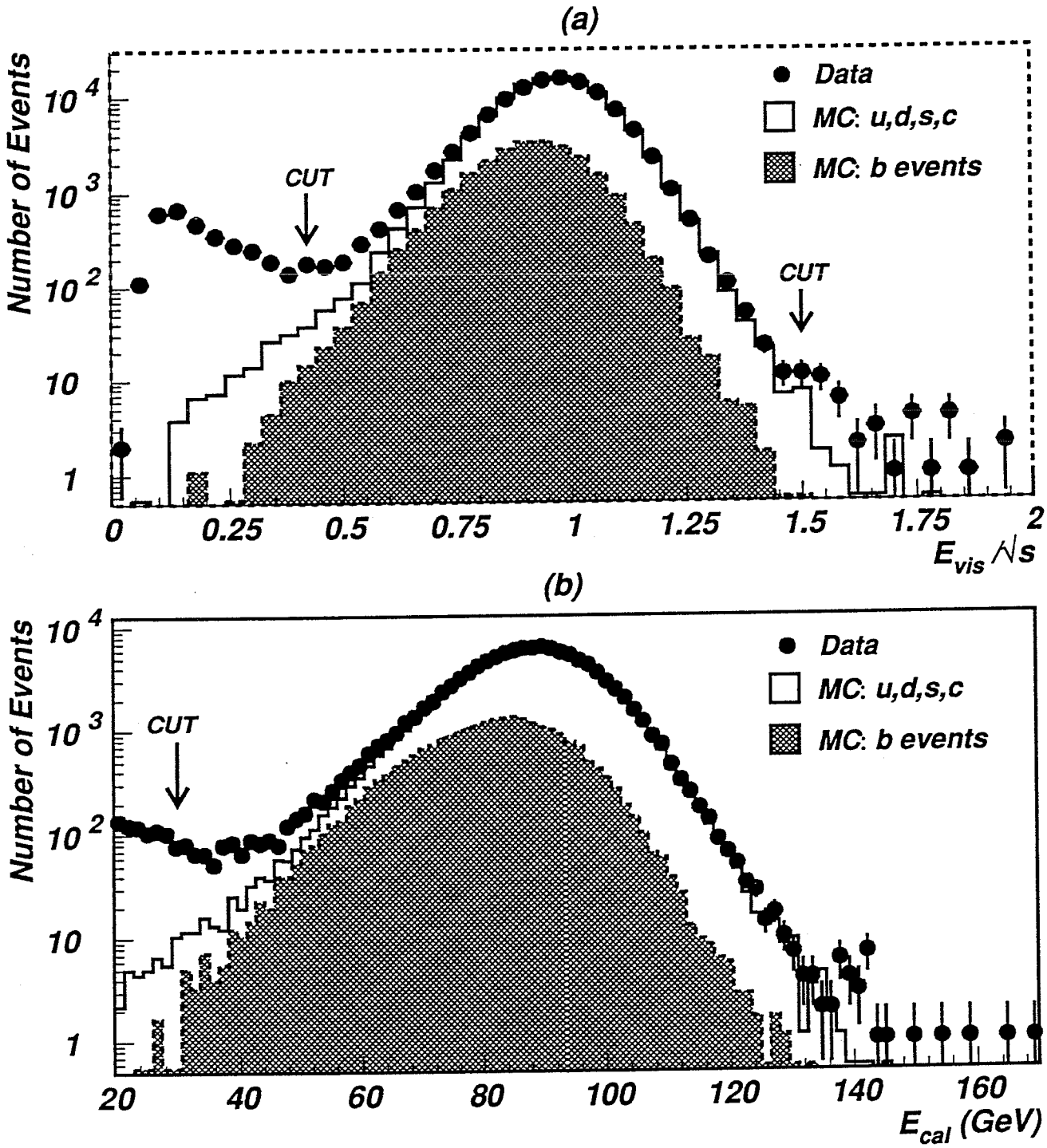

Figure 6-3: The energy distribution for $e^+e^- \rightarrow$ *hadrons* , (a) visible energy fraction; (b) energy in the calorimeter;

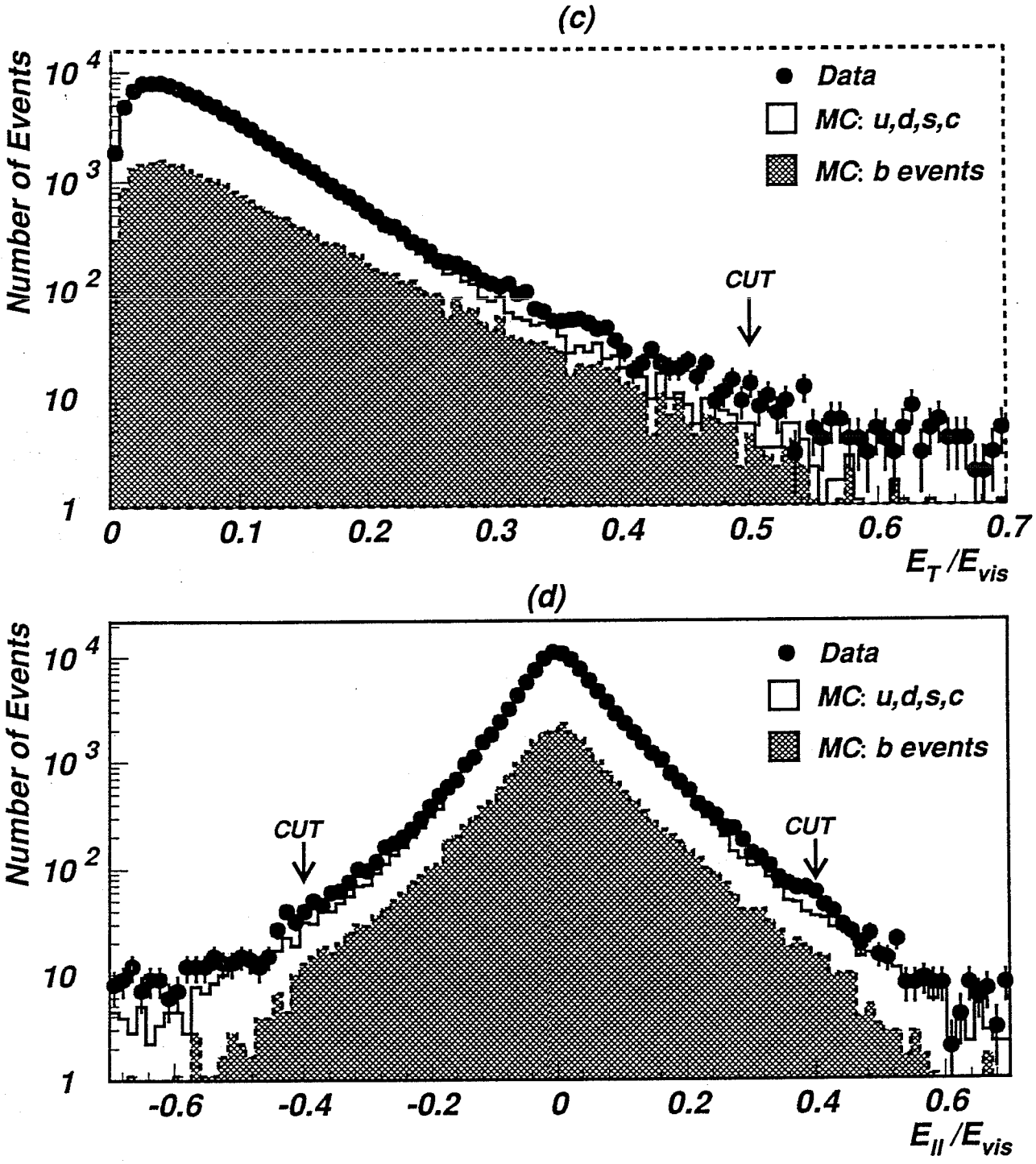

Figure 6-3: (c) transverse energy imbalance; (d) longitudinal energy imbalance.

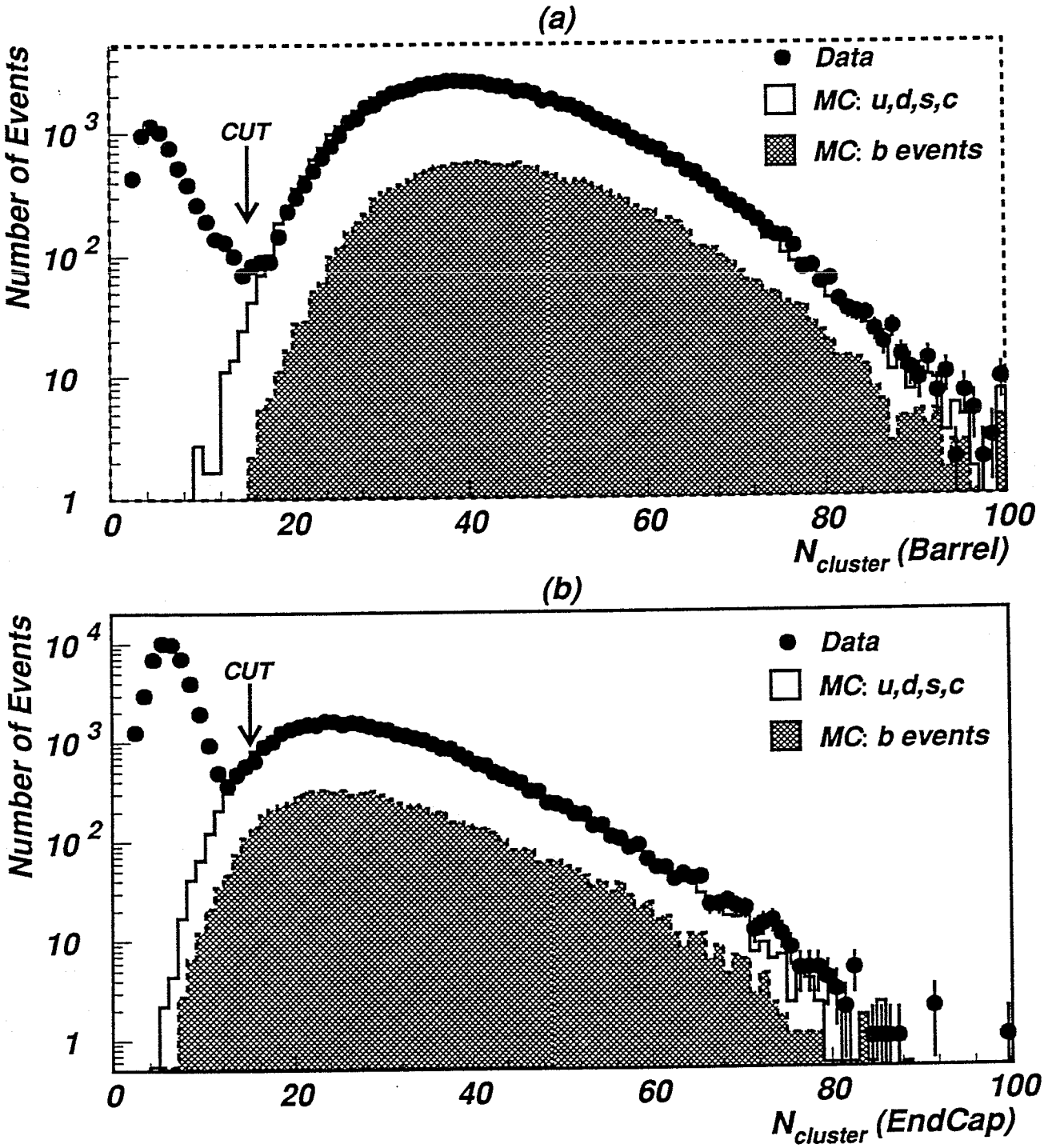

Figure 6-4: Number of clusters reconstructed in the calorimeters for hadronic events (a) barrel region, (b) EndCap region.

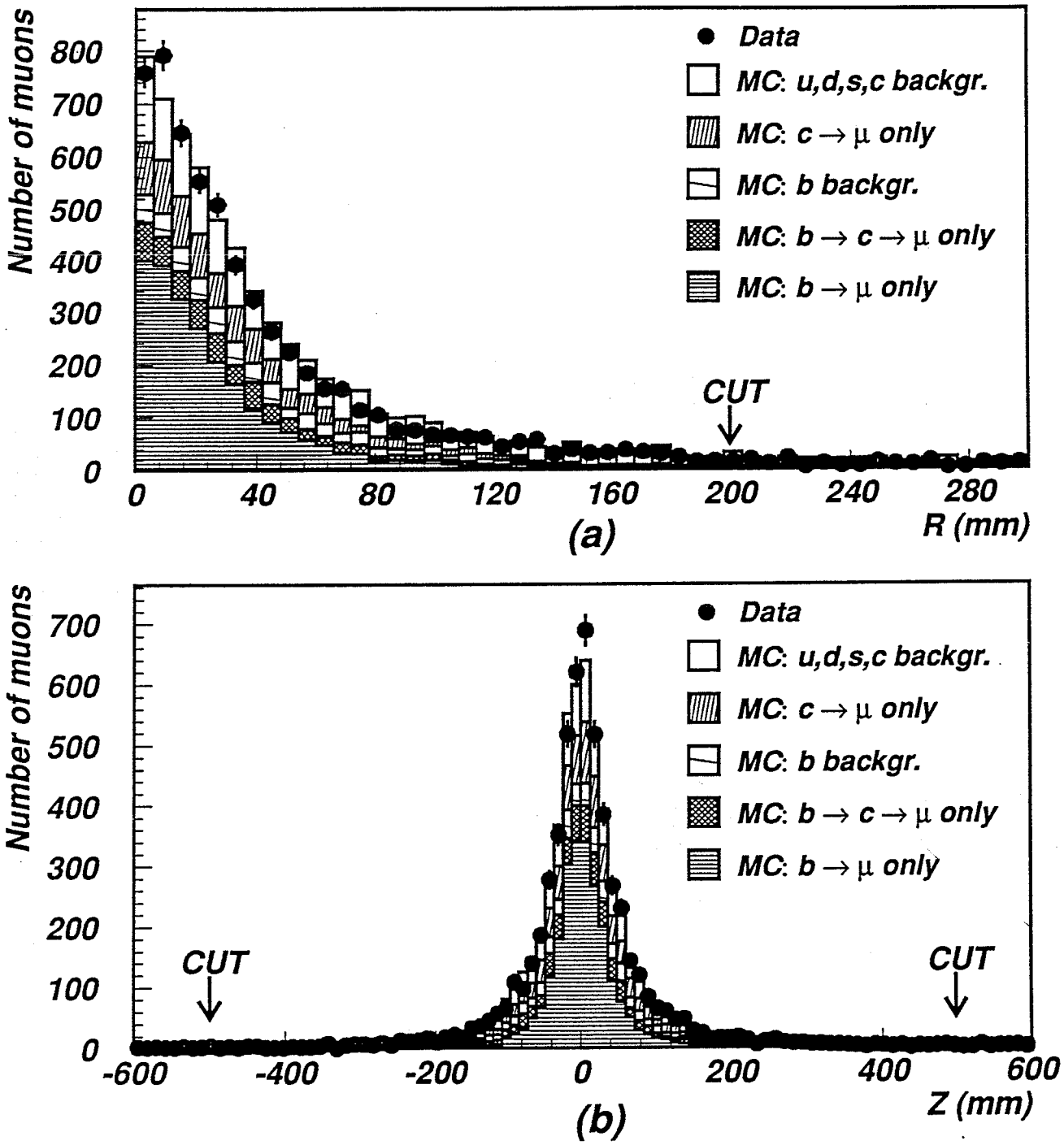

Figure 6-5: The reconstructed vertex distributions, (a) in the $R-\phi$ plane; (b) in the $R-Z$ plane.

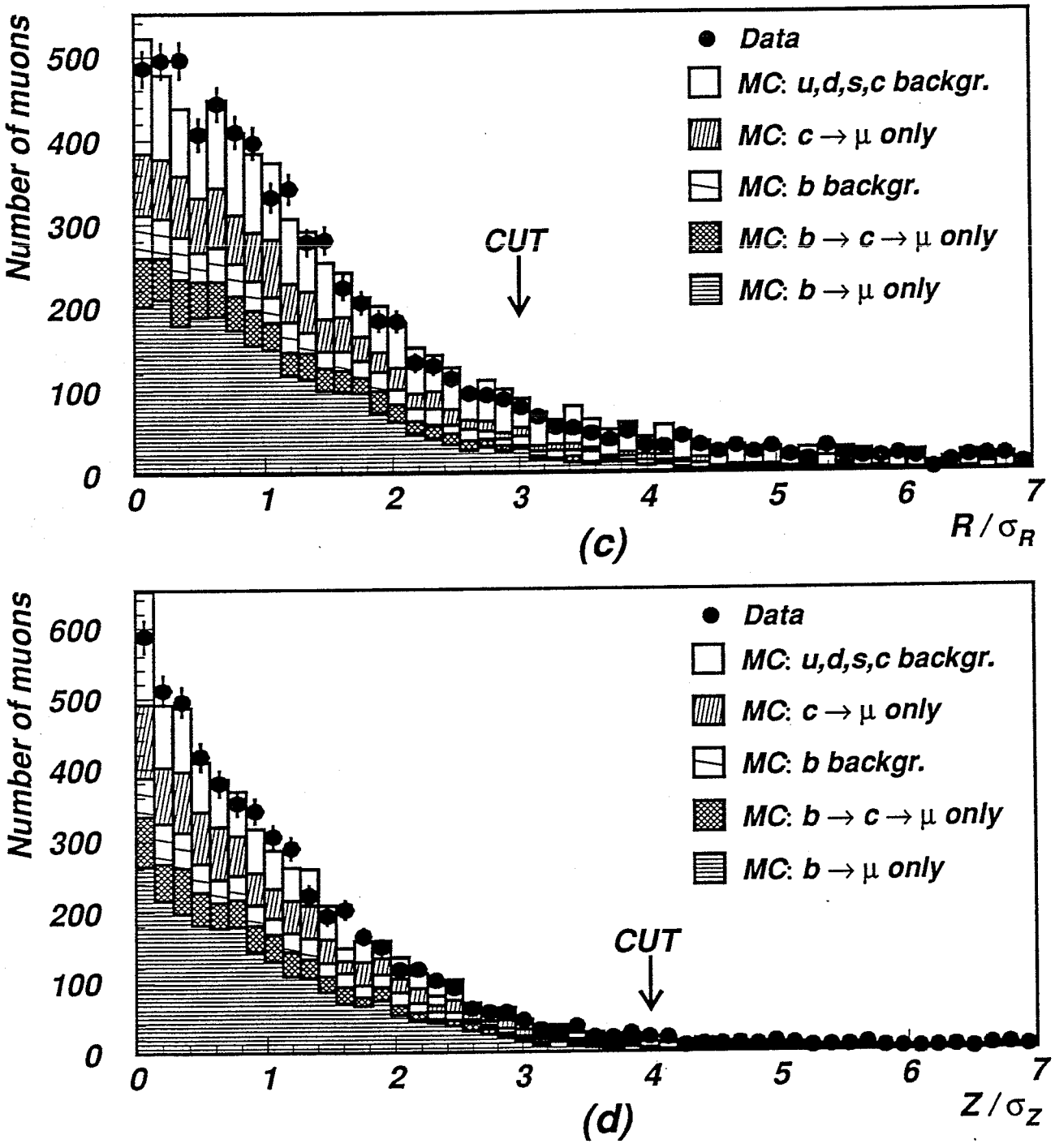

Figure 6-5: The reconstructed vertex distributions, (c) R/σ_R in the $R-\phi$ plane; (d) Z/σ_Z in the $R-Z$ plane.

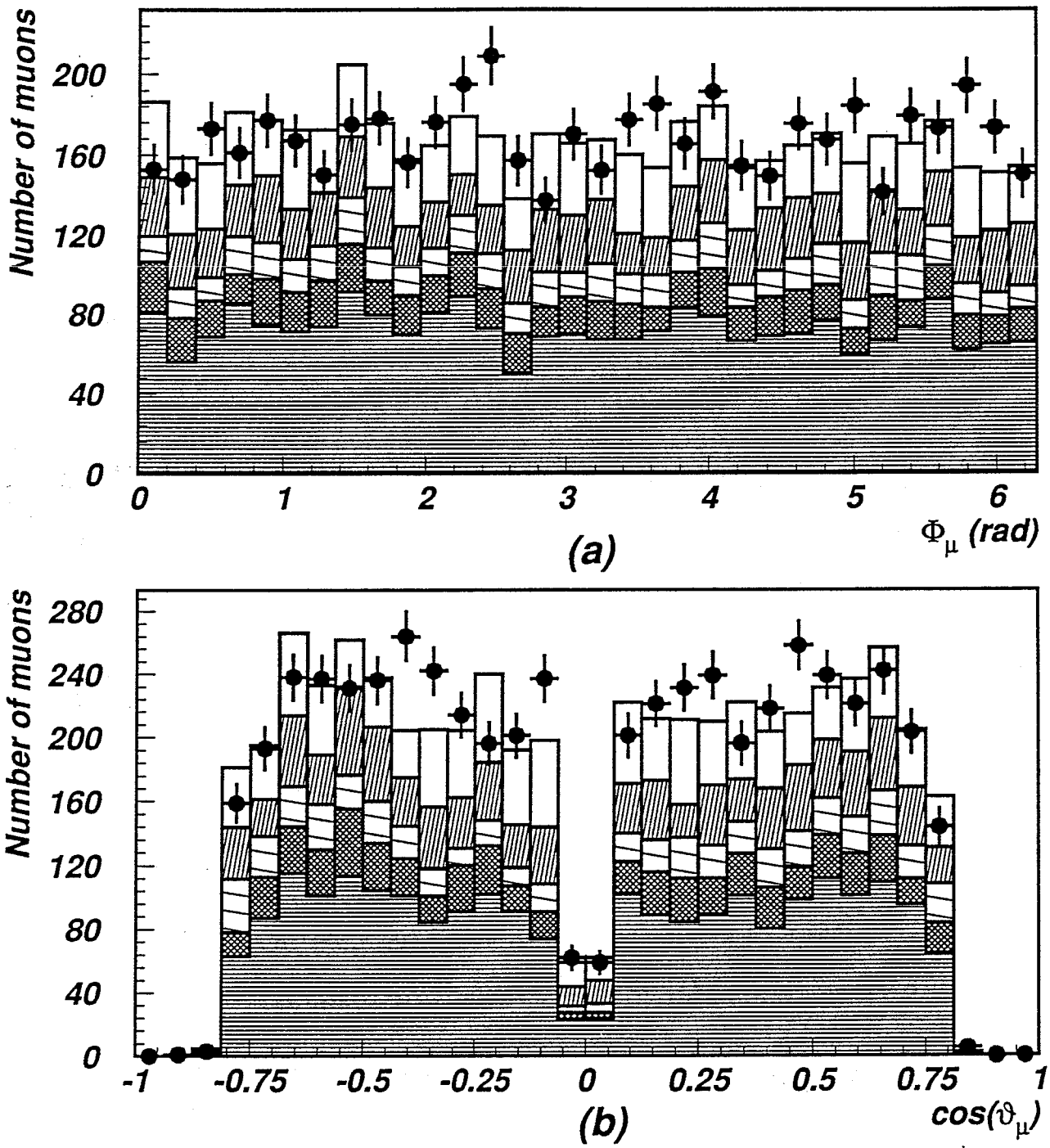

Figure 6-6: The angular distributions in (a) ϕ and (b) θ of the selected inclusive muon events.

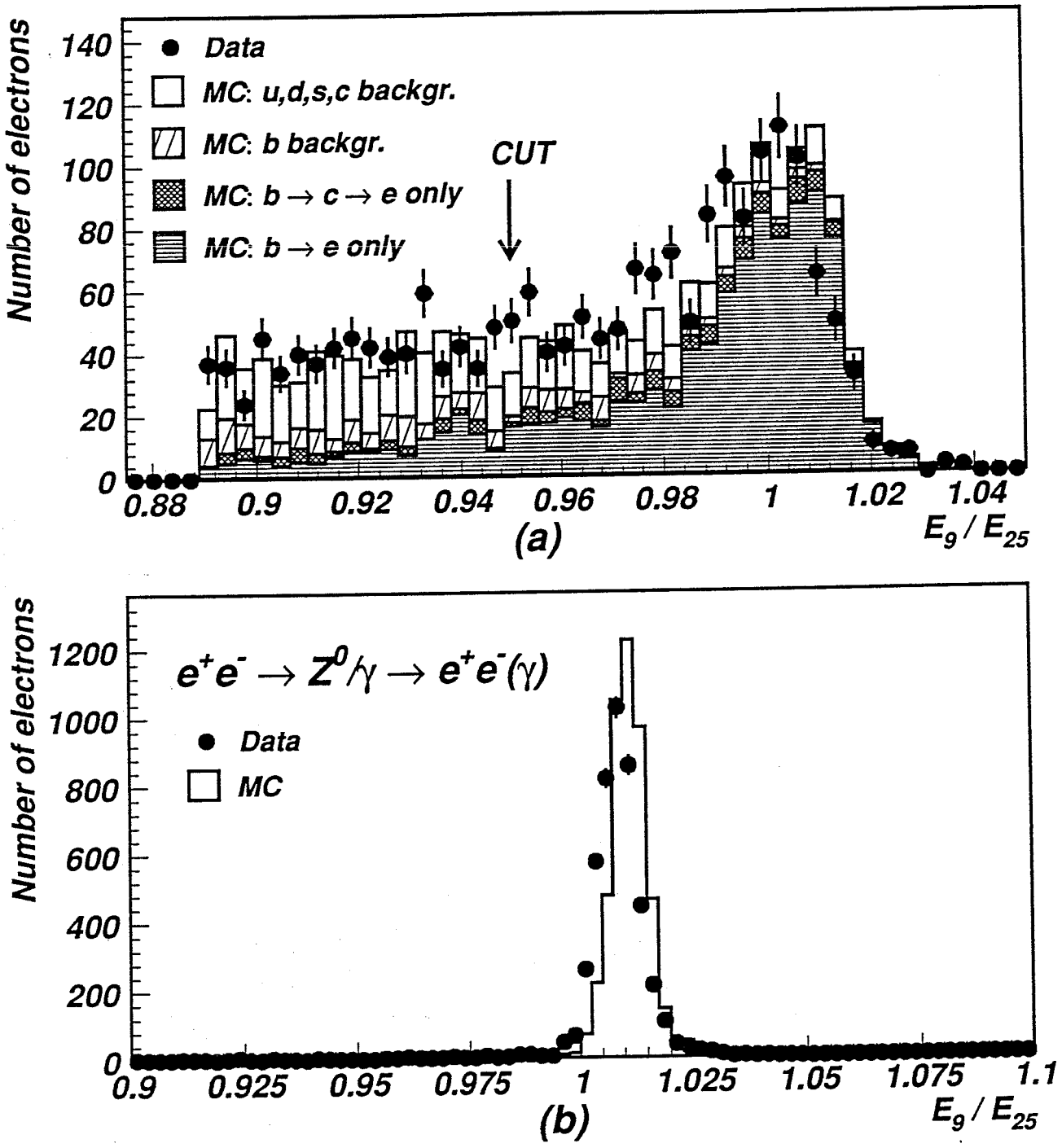

Figure 6-7: The E_9/E_{25} distribution of electron candidates in the BGO calorimeter for (a) inclusive electron events; (b) Bhabha events.

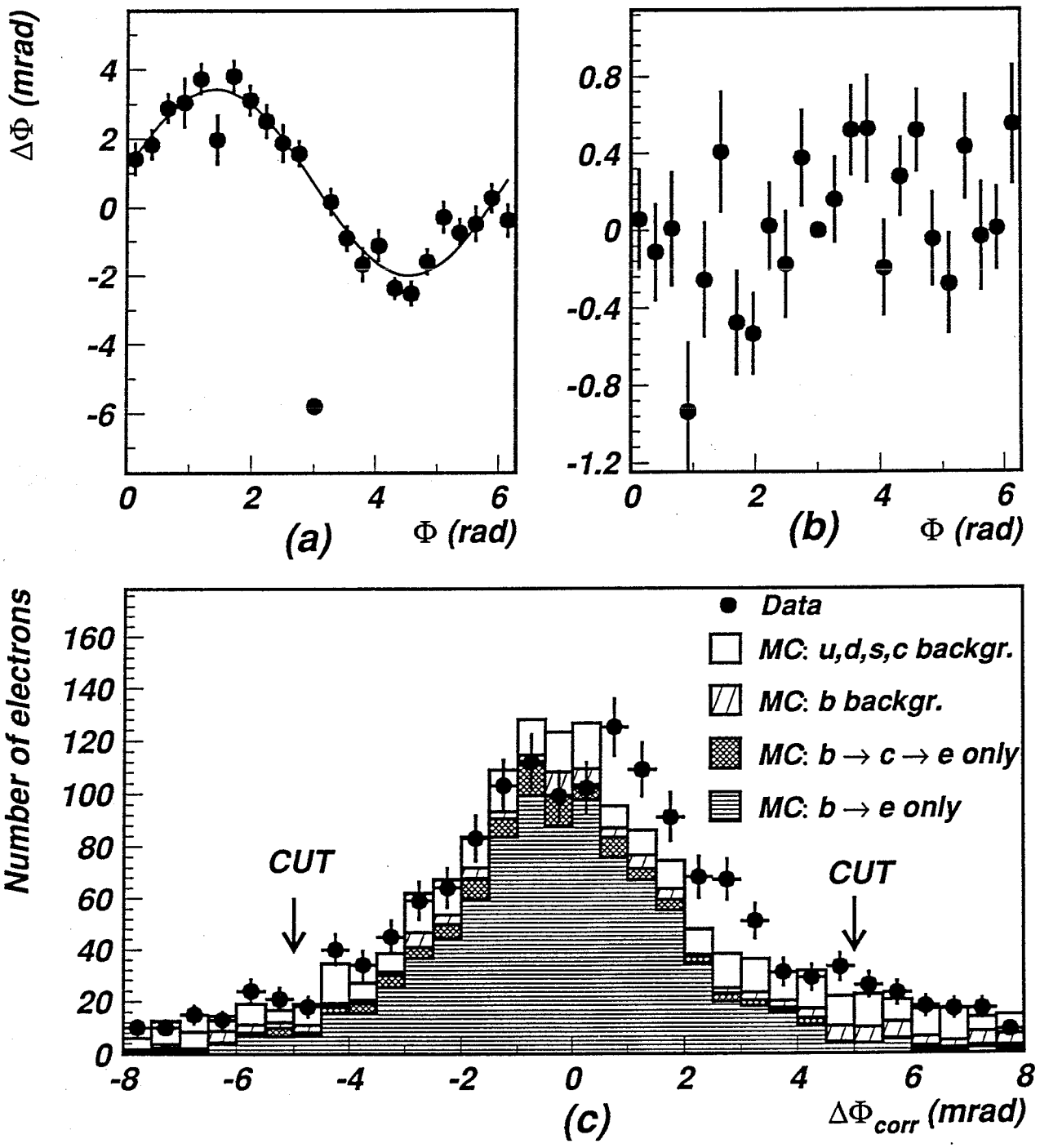

Figure 6-8: (a) average $\Delta\phi$ without correction, the curve is the correction function; (b) average $\Delta\phi$ with correction; (c) the $\Delta\phi$ distribution with correction.

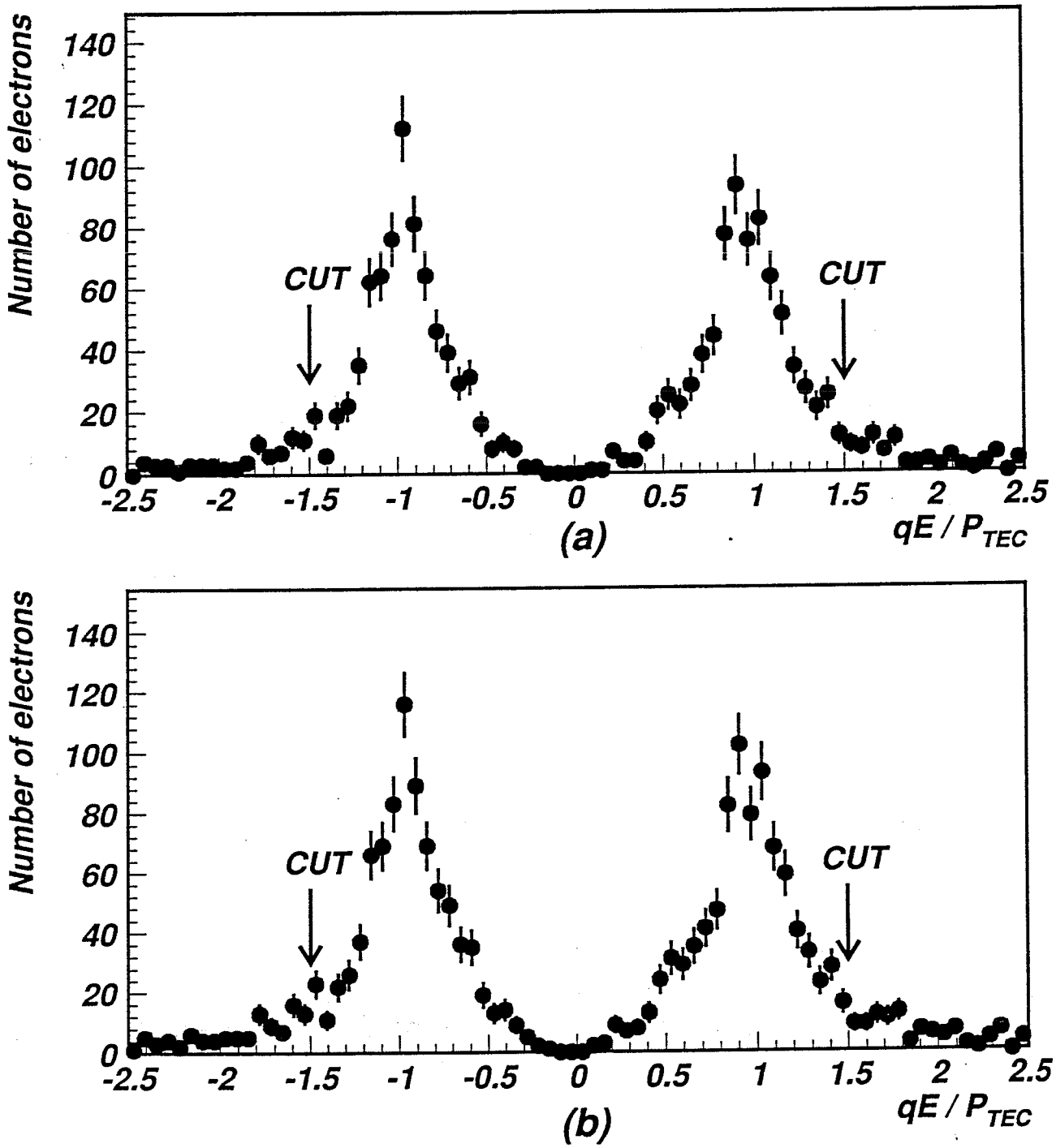

Figure 6-9: The qE/p distribution for electron candidates : (a) the tracks around electrode removed; (b) all the tracks.

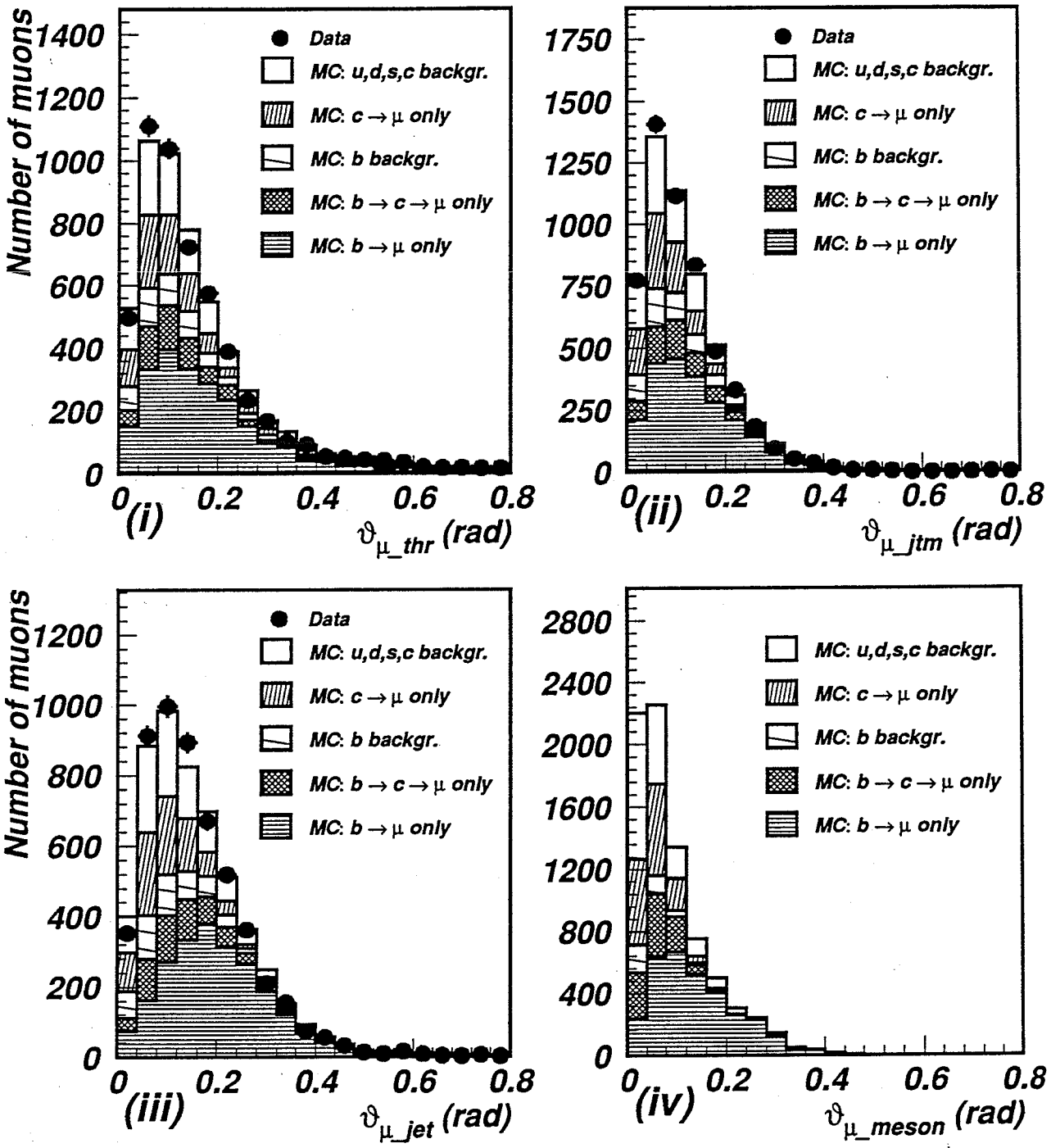

Figure 6-10: The distributions of opening angle between muon and (i) thrust axis; (ii) jet axis, the muon included in the jet; (iii) jet axis, the muon excluded from the jet; (iv) original hadrons.

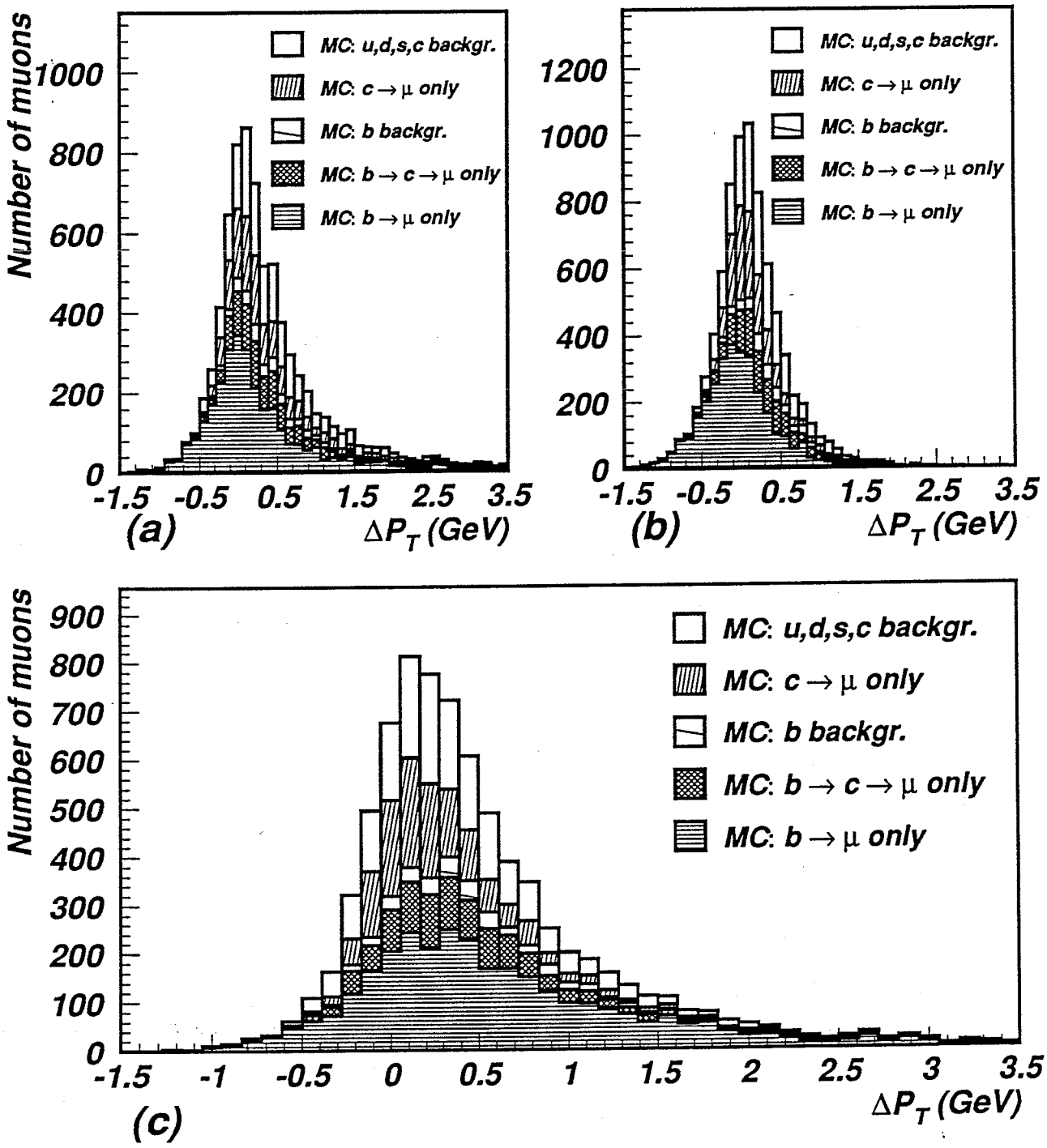

Figure 6-11: The distributions of the $\Delta p_{\perp}$, (a) $p_{\perp thrust} - p_{\perp meson}$; (b) $p_{\perp jtm} - p_{\perp meson}$; (b) $p_{\perp jet} - p_{\perp meson}$.

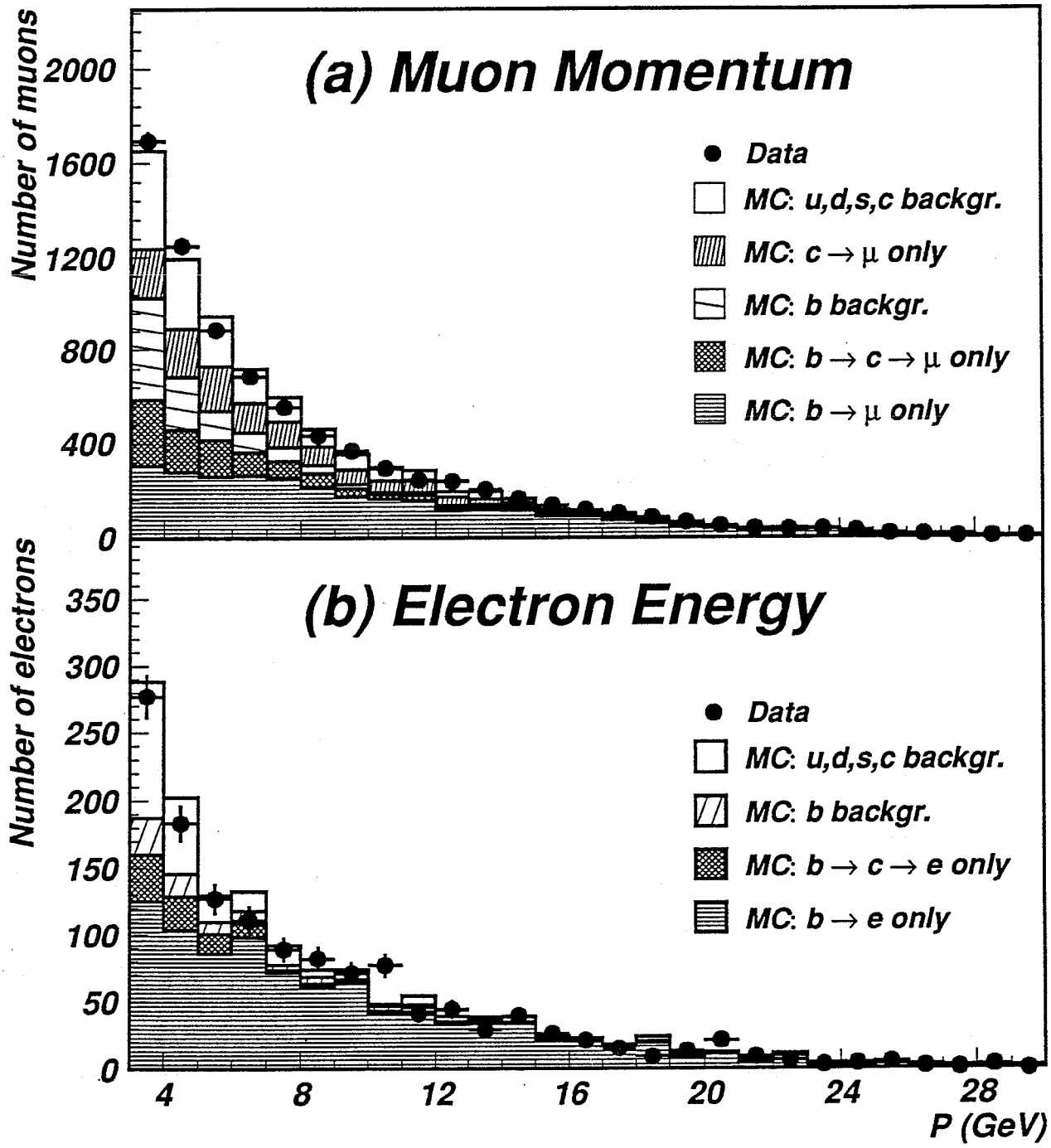

Figure 6-12: The measured (a) muon momentum and (b) electron energy of inclusive lepton events.

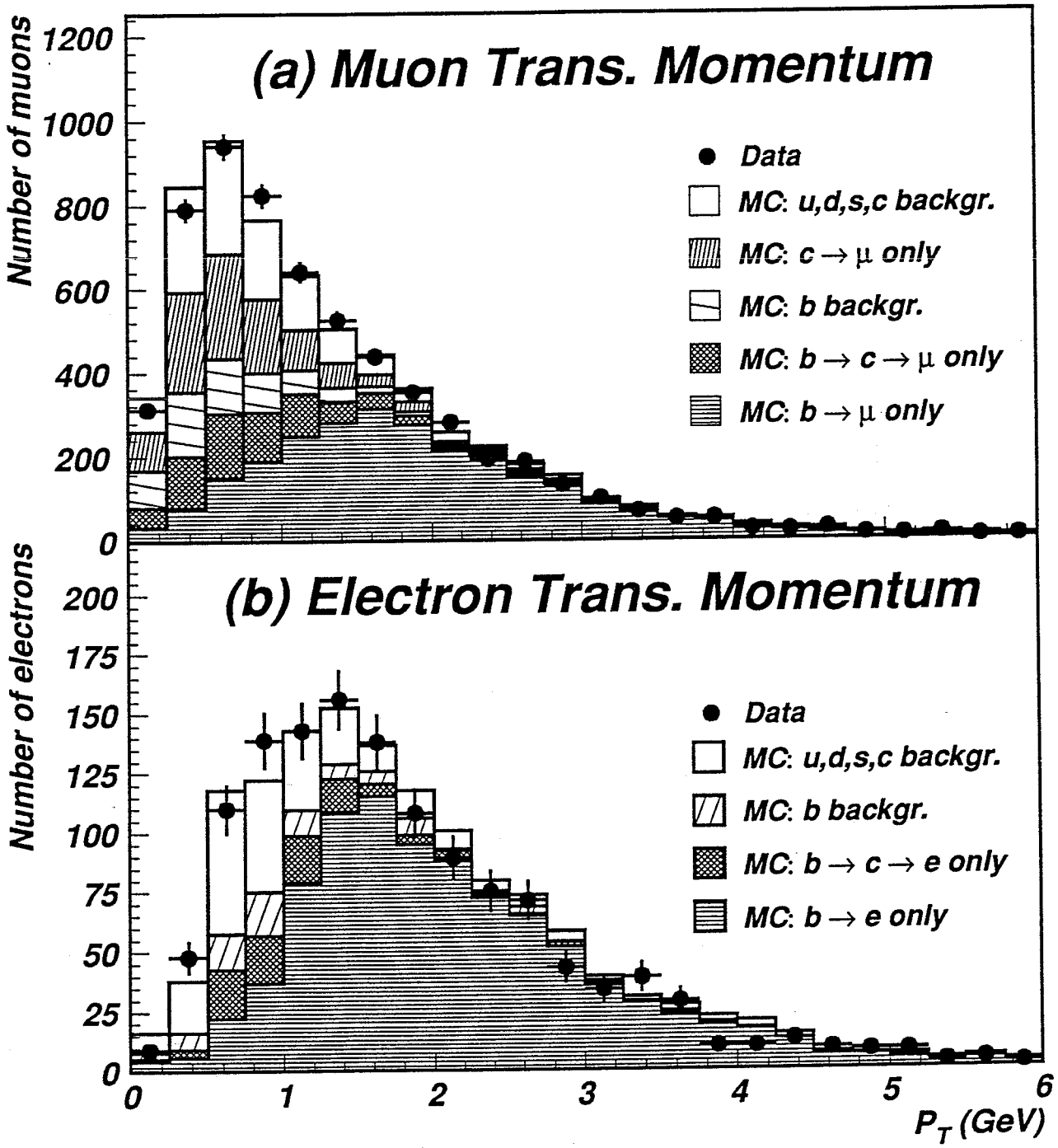

Figure 6-13: The measured transverse momentum of (a) muons and (b) electrons for inclusive lepton events.

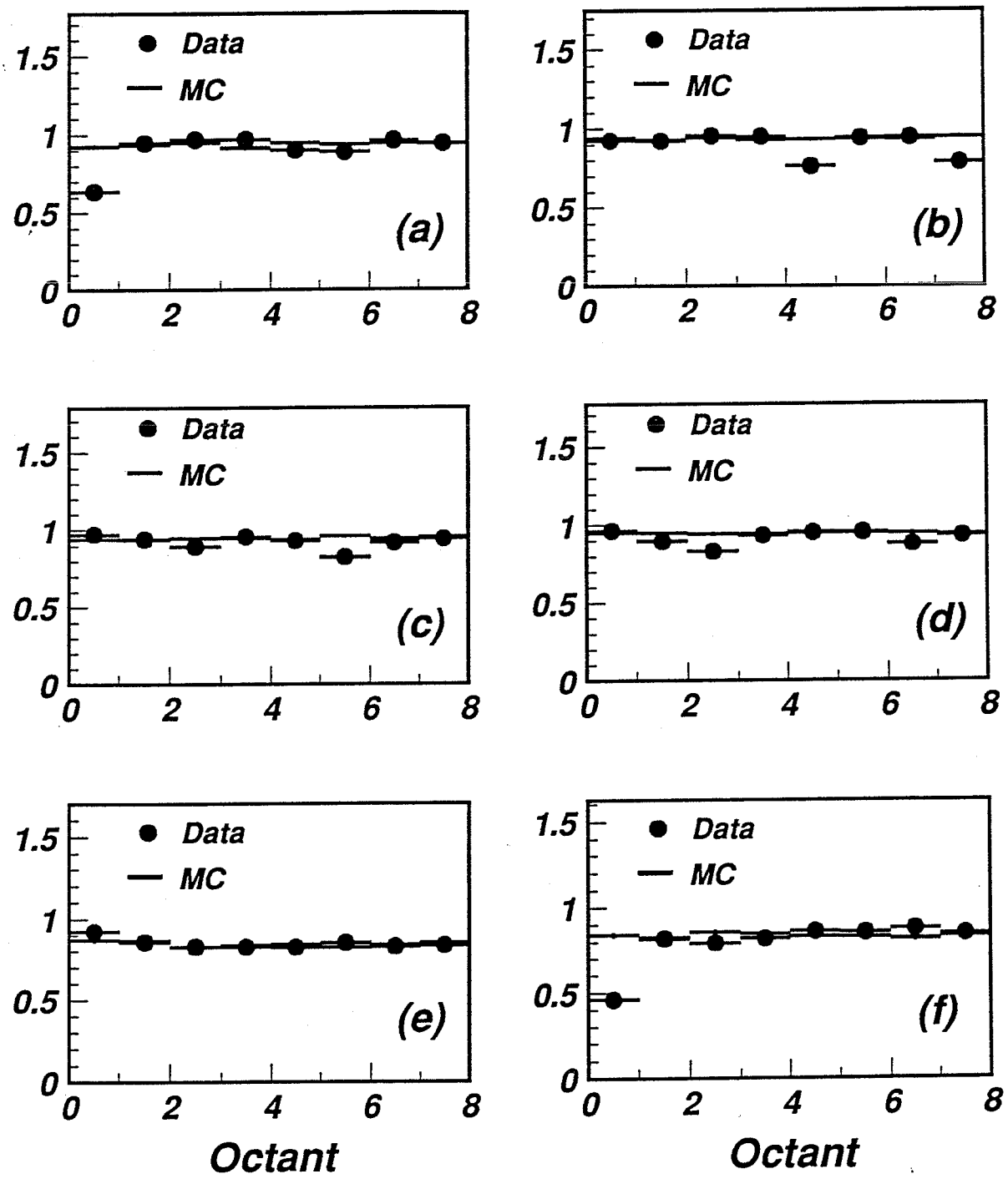

Figure 7-1: The fraction of tracks in P chamber (a) MI master, (b) MI slave, (c) MM master, (d) MM slave, (e) MO master, (f) MO slave, for data (dots) and perfect Monte Carlo (solid lines).

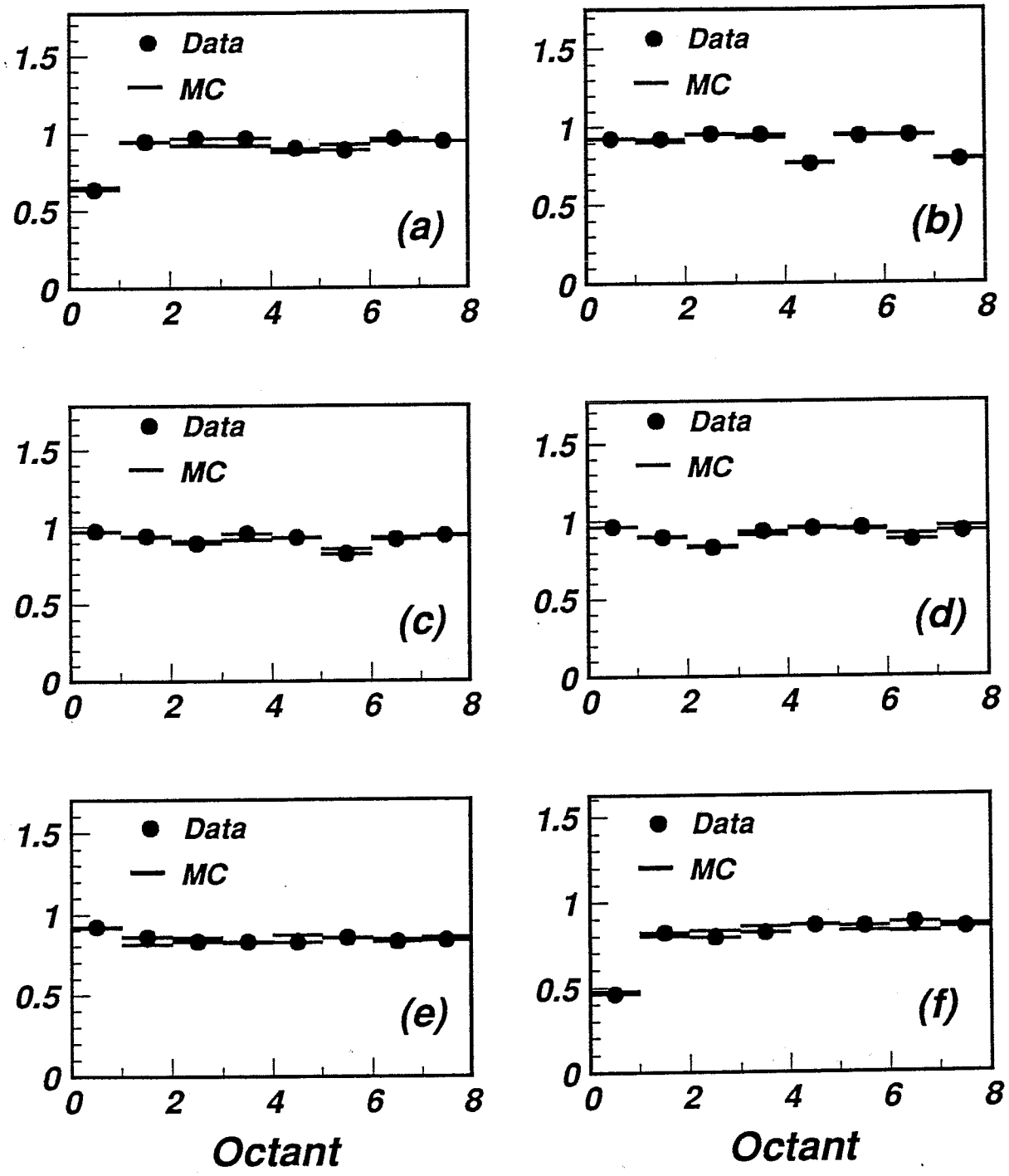

Figure 7-2: The fraction of tracks in P chamber (a) MI master, (b) MI slave, (c) MM master, (d) MM slave, (e) MO master, (f) MO slave, for data (dots) and corrected Monte Carlo (solid lines).

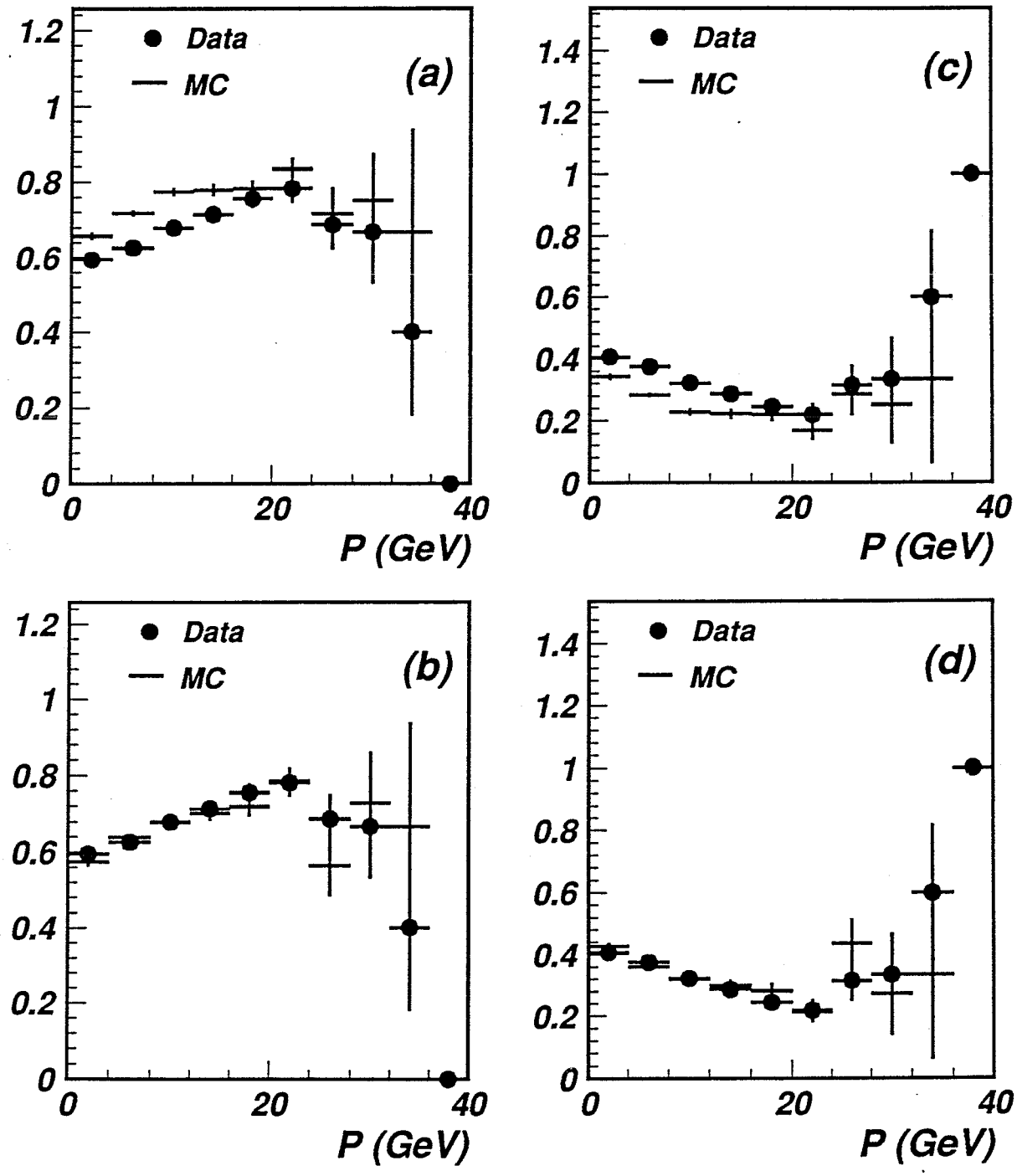

Figure 7-3: The fraction of tracks with (a) and (b) three P-segments, (c) and (d) two P-segments, for data compared to (a) and (c): perfect Monte Carlo, (b) and (d): corrected Monte Carlo.

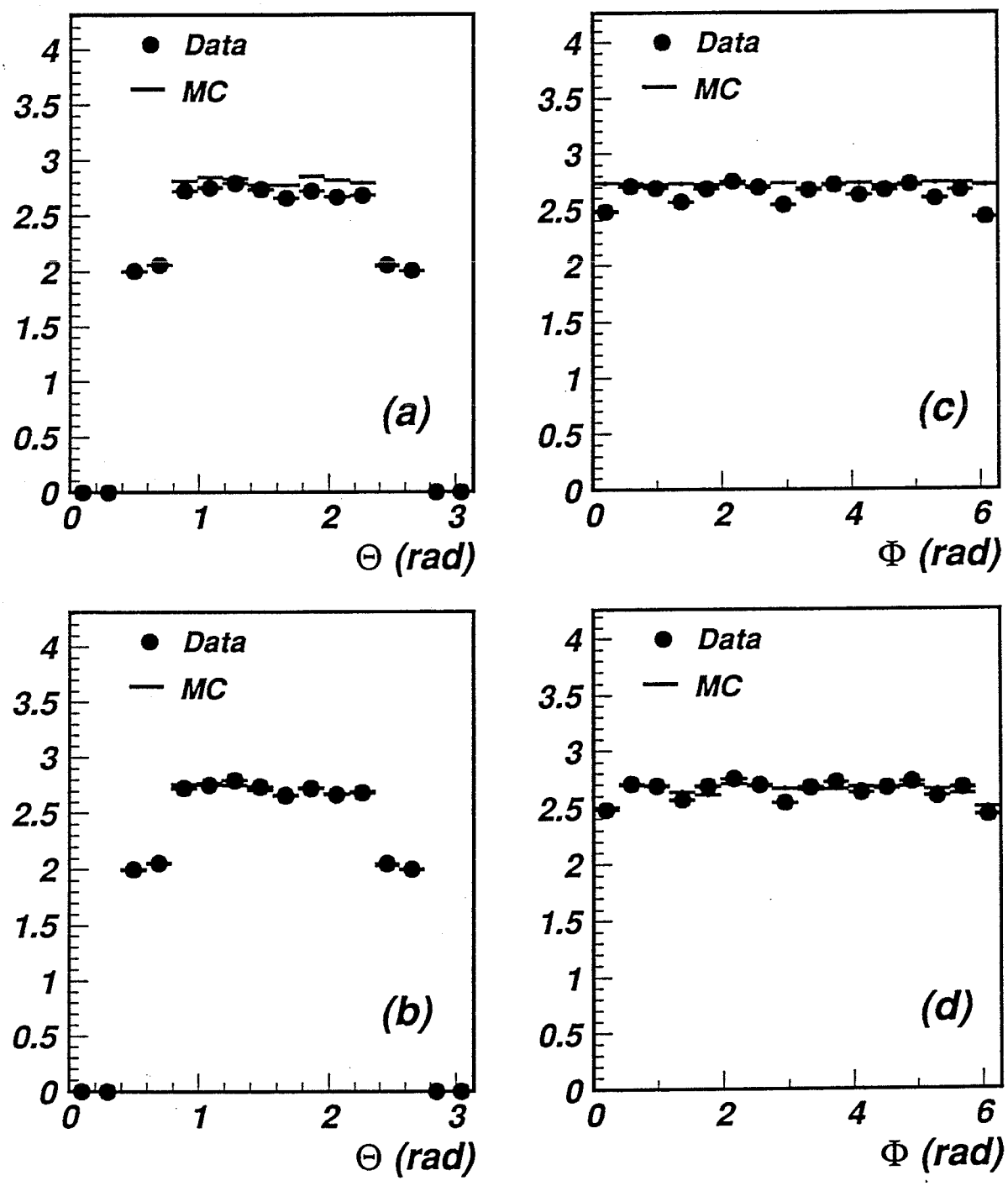

Figure 7-4: The average number of P segments in θ and ϕ for data compared to (a) and (c): perfect Monte Carlo, (b) and (d): corrected Monte Carlo.

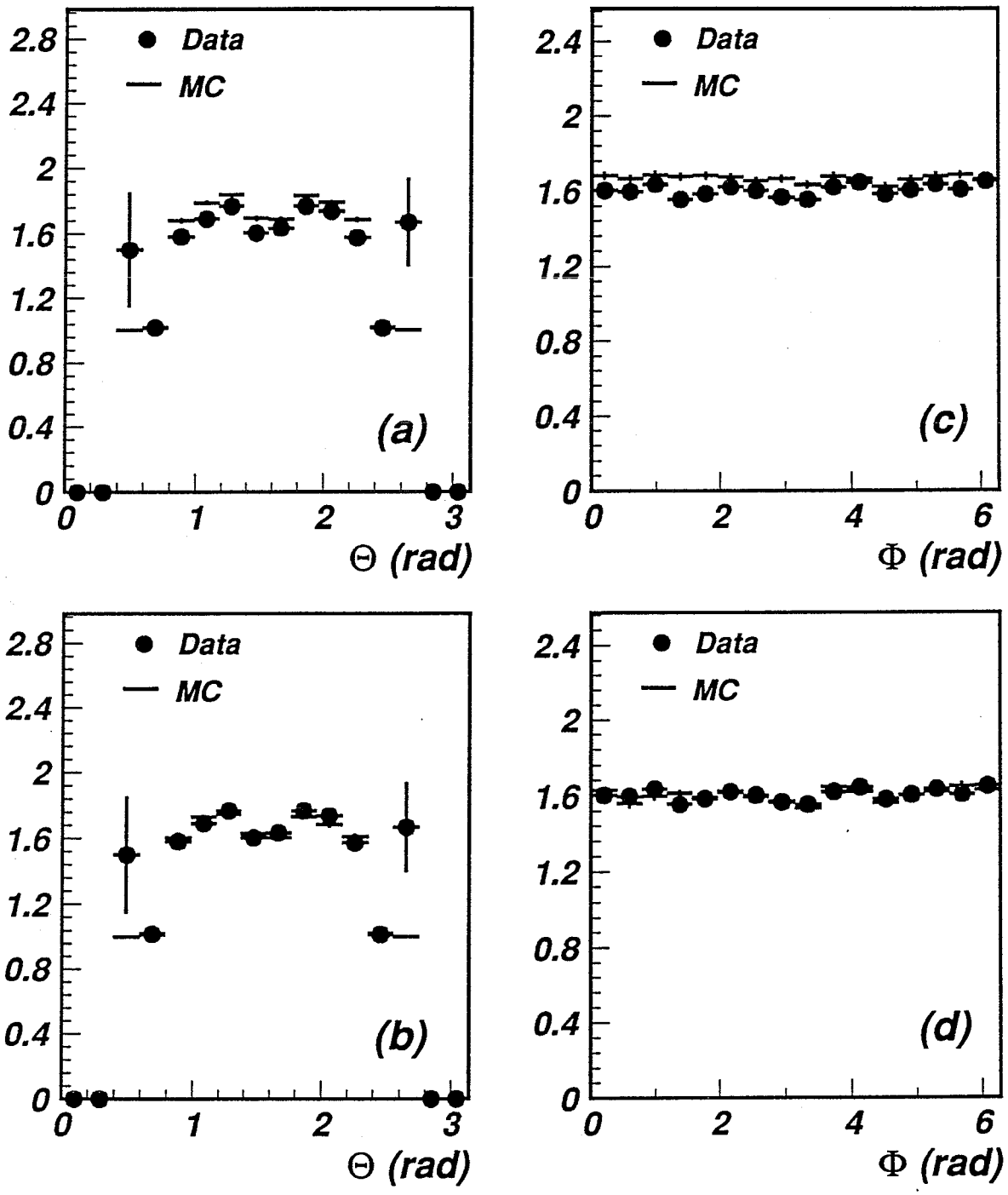

Figure 7-5: The average number of Z segments in θ and ϕ for data compared to (a) and (c): perfect Monte Carlo, (b) and (d): corrected Monte Carlo.

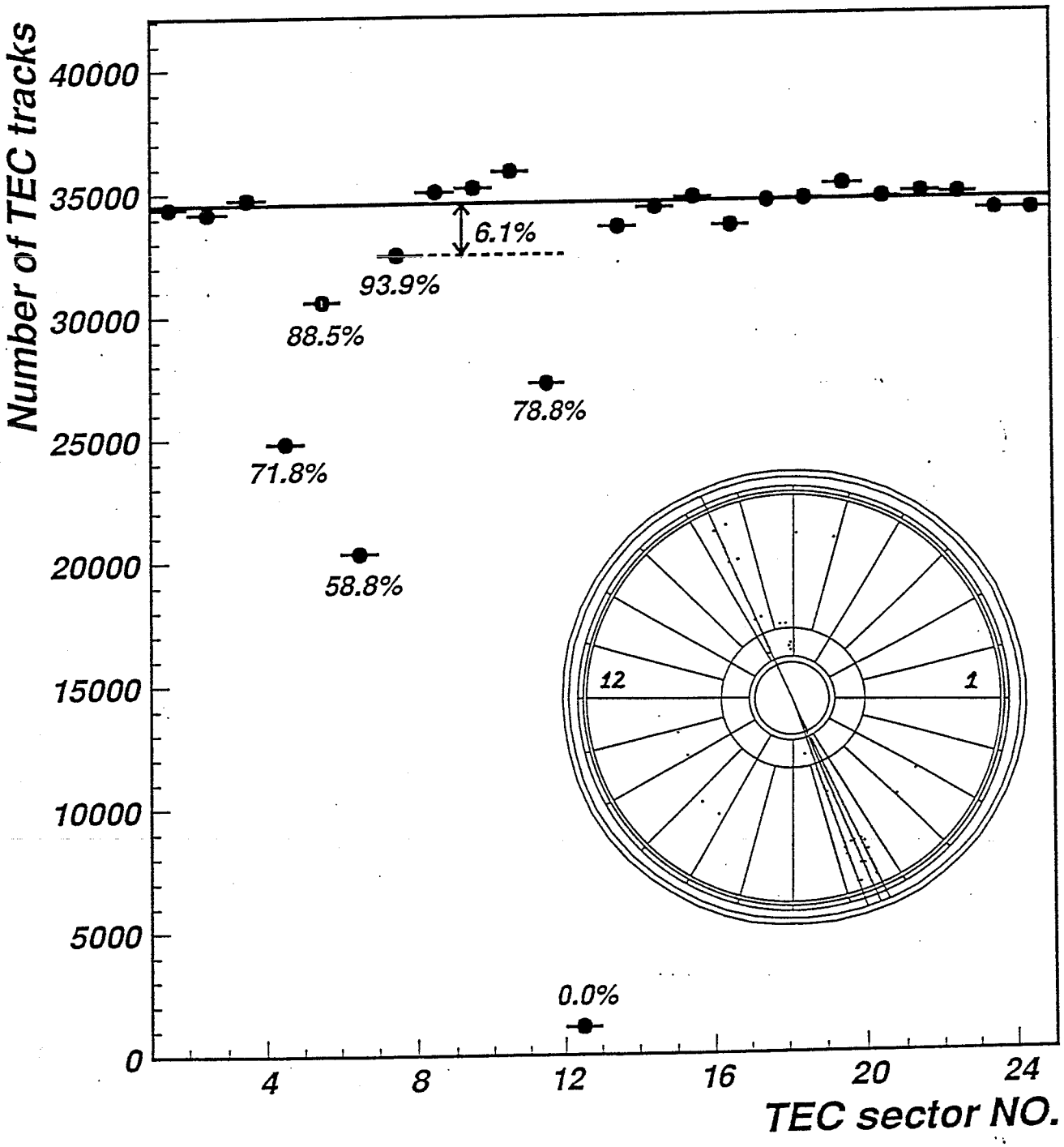

Figure 7-6: Number of tracks and efficiency of individual TEC sector from the hadronic events.

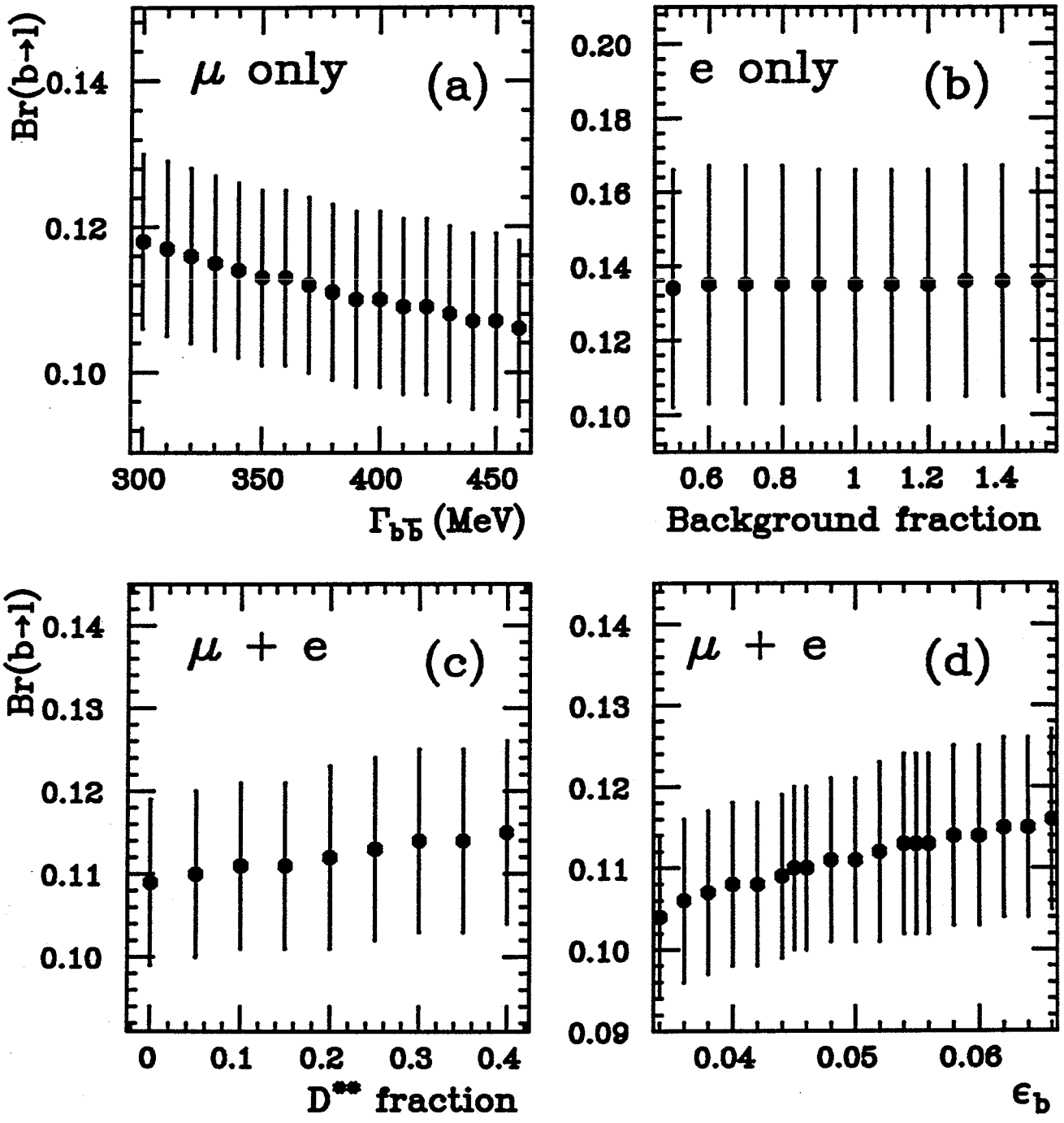

Figure 8-1: The systematic studies of $Br(b \to l\nu X)$ in variation of (a) $\Gamma_{b\bar{b}}$; (b) background fraction; (c) D^{**} fraction; (d) b fragmentation function ϵ_b.

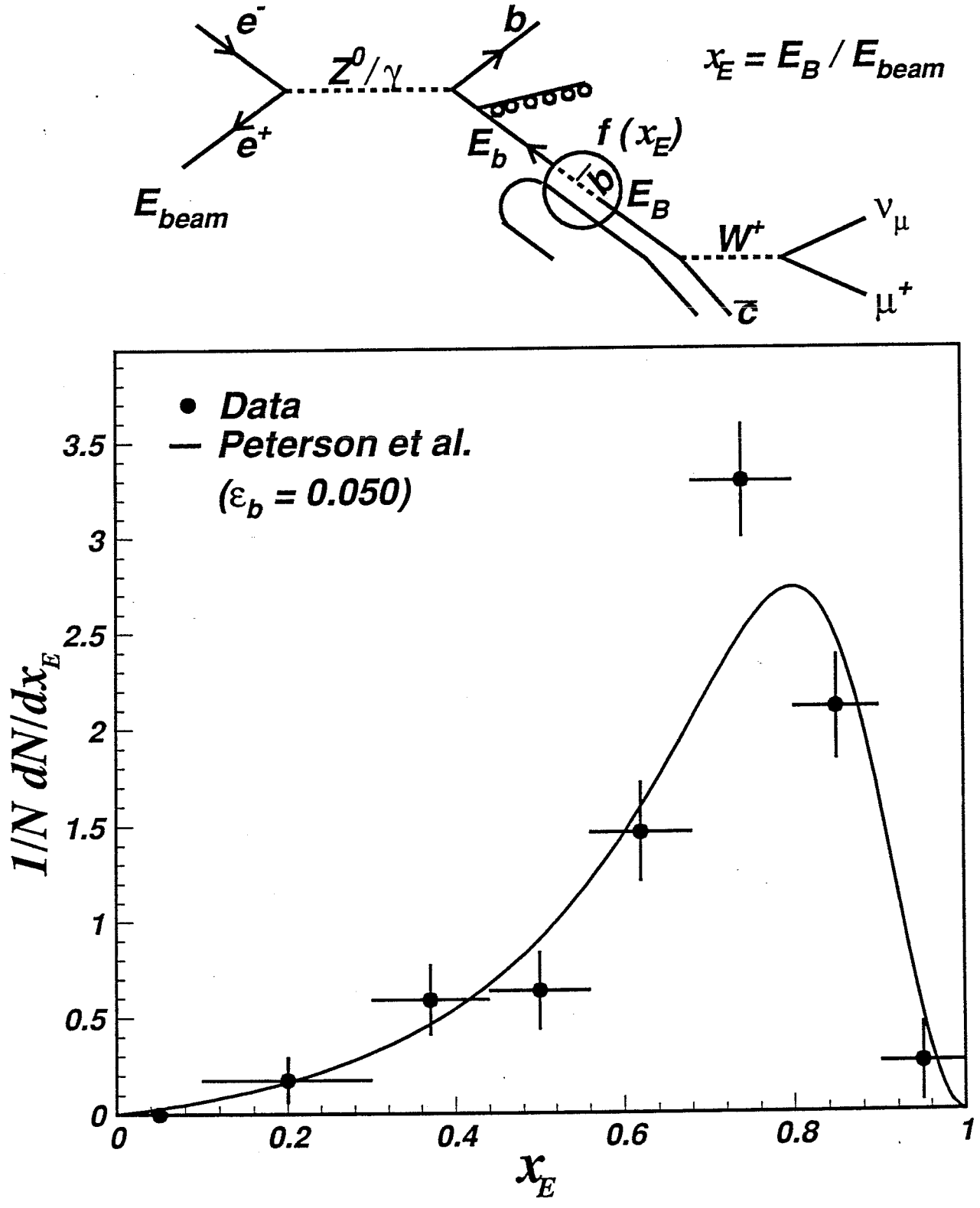

Figure 8-2: Measured b quark fragmentation function $f(x_E)$ from a six-parameter fit to the inclusive muon data. The solid line shows the Peterson *et al.* with $\epsilon_b = 0.050$.

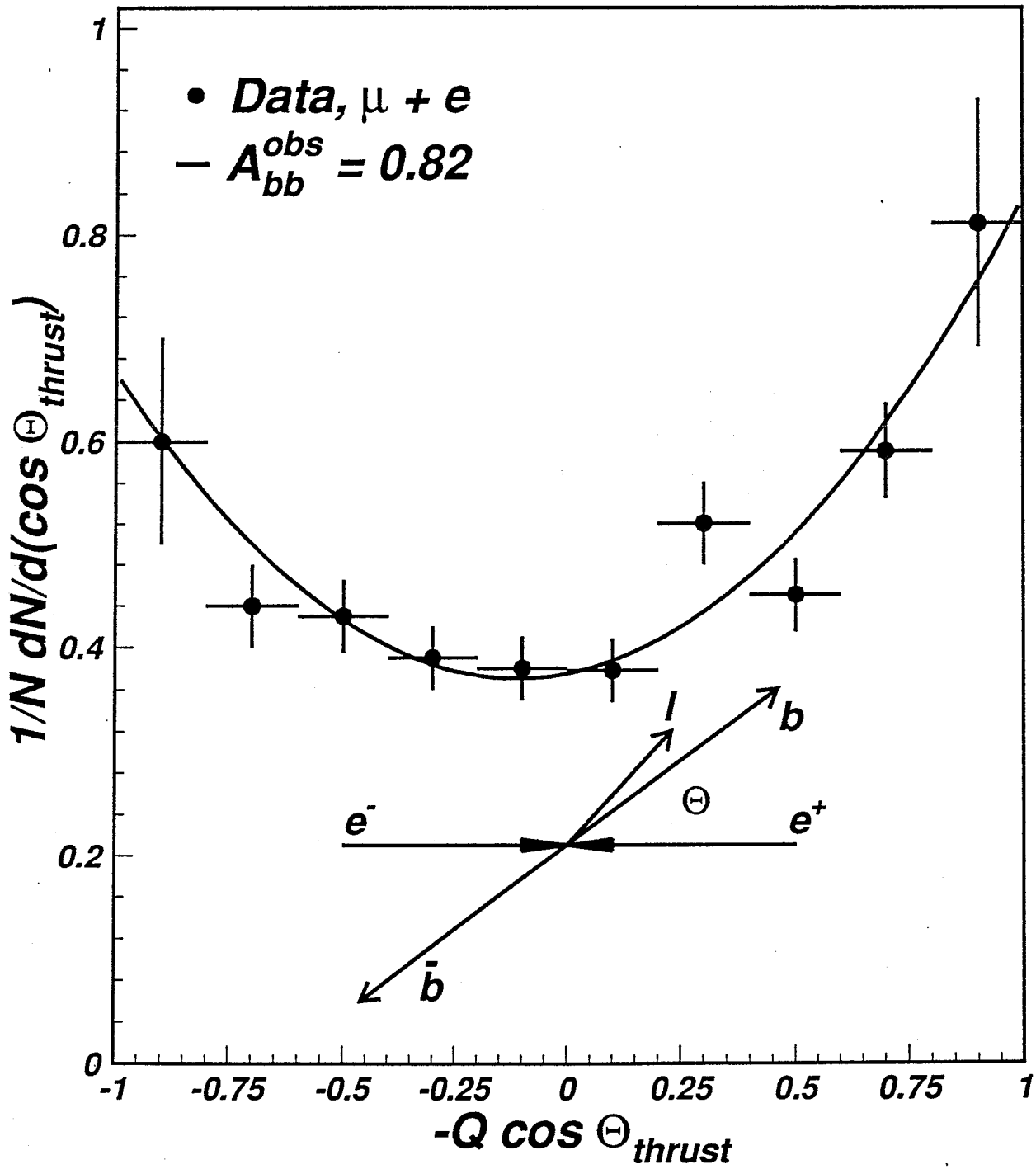

Figure 8-3: Distribution of measured $-Q\cos\theta_b$ for inclusive lepton sample, after background and acceptance corrections. The solid curve shows the expected distribution for $A_{b\bar{b}}^{obs} = 0.82$.

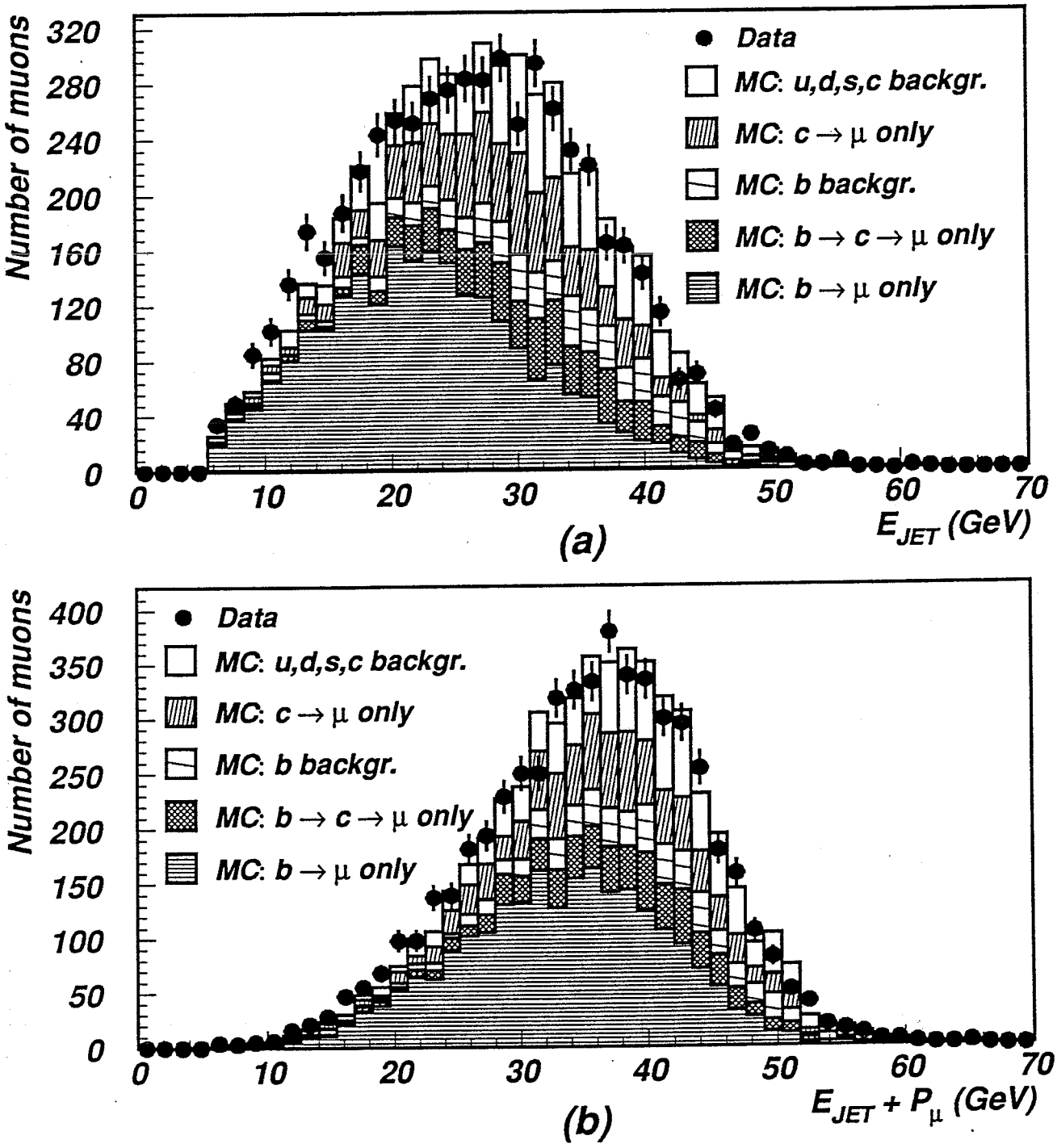

Figure 8-4: The nearest jet energy distributions (a) muon excluded from jet; (b) muon included in the jet.

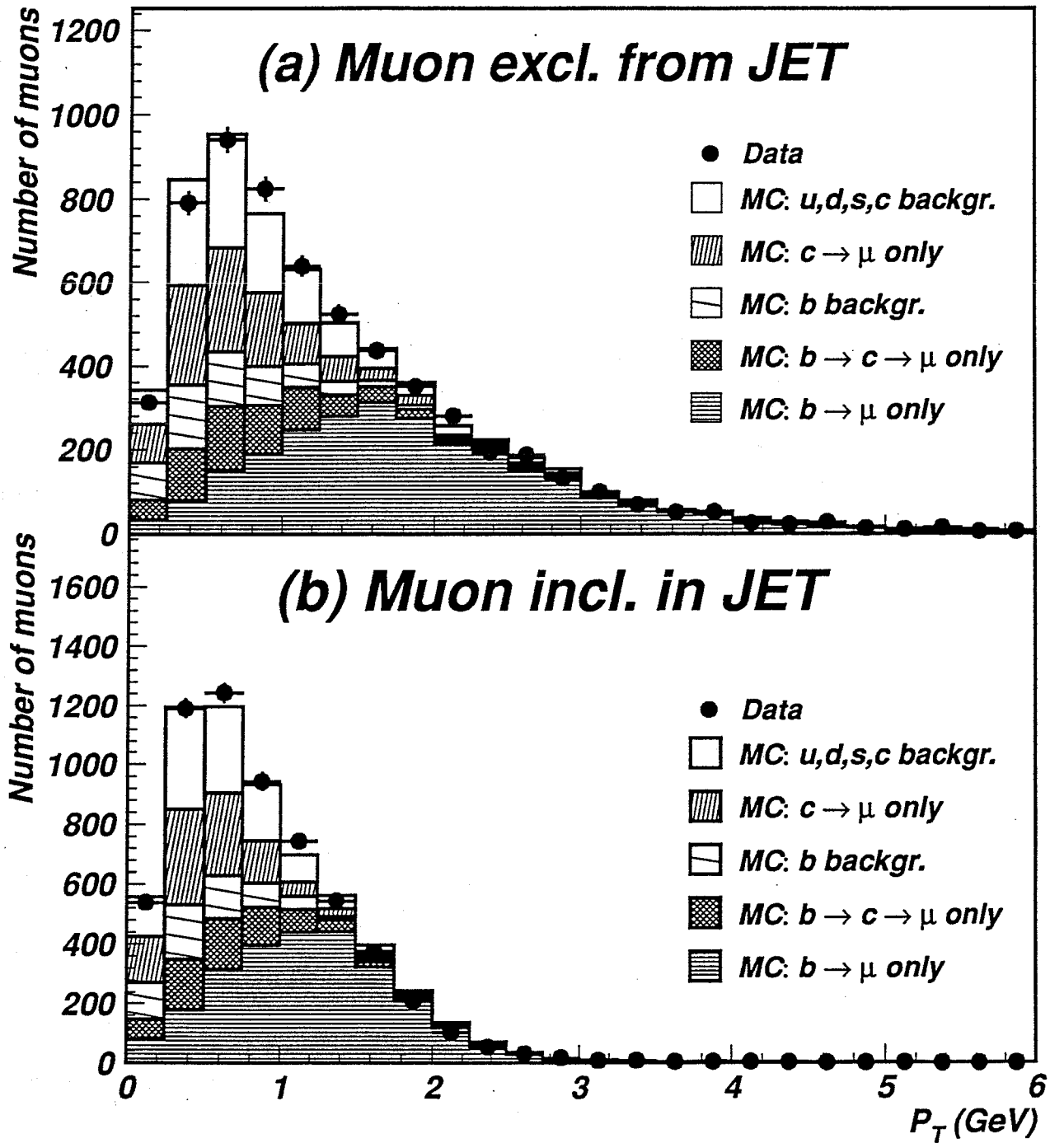

Figure 8-5: The muon $p_\perp$ distributions, where the measured muon momentum (a) excluded from jet and (b) included in the jet to calculate jet axis.

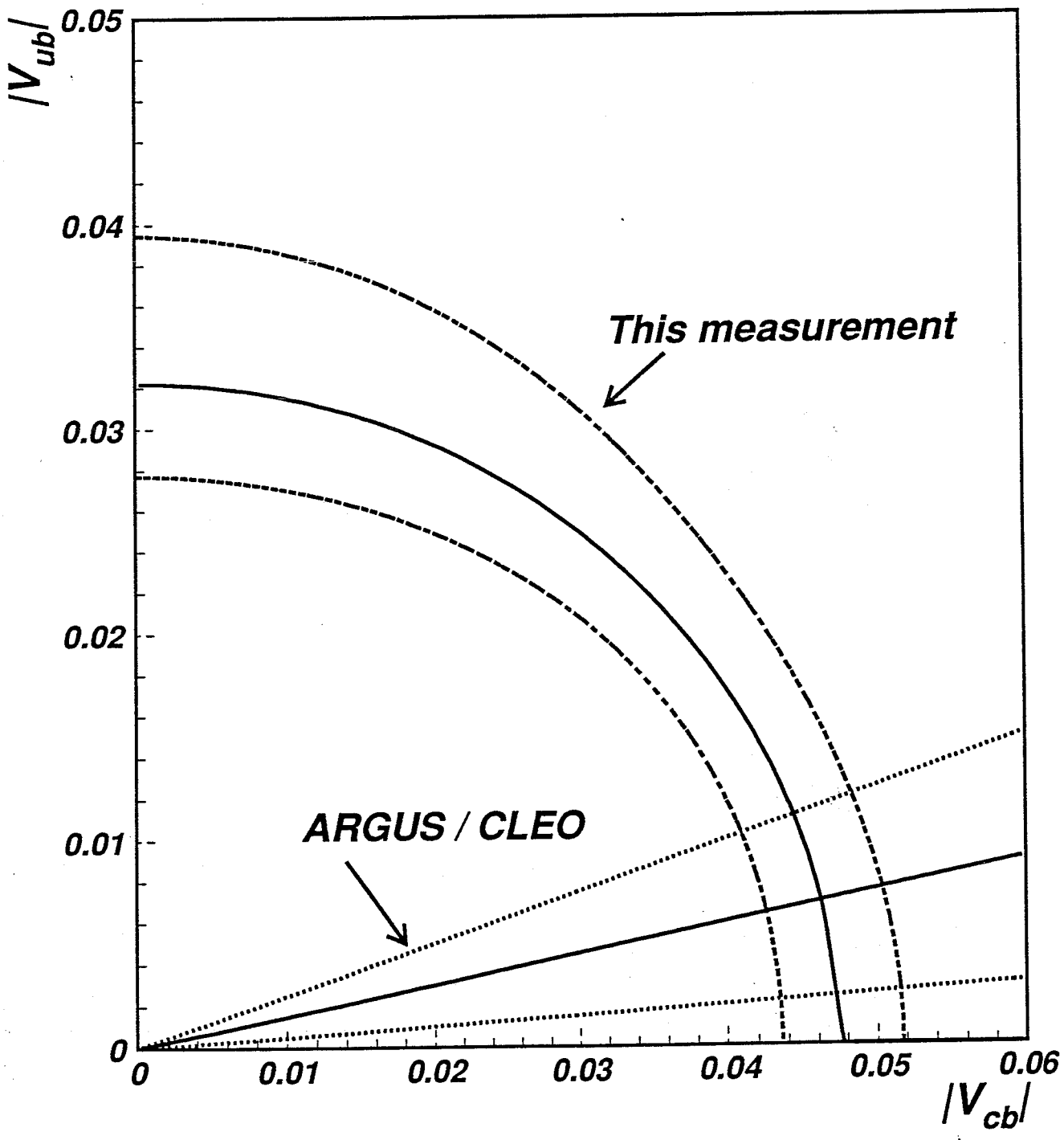

Figure 8-6: The comparison of the V_{cb} and V_{ub} measurement with those from ARGUS/CLEO. The solid curves are measurements, and the dashed curves corresponding to the 1 standard deviation limits.

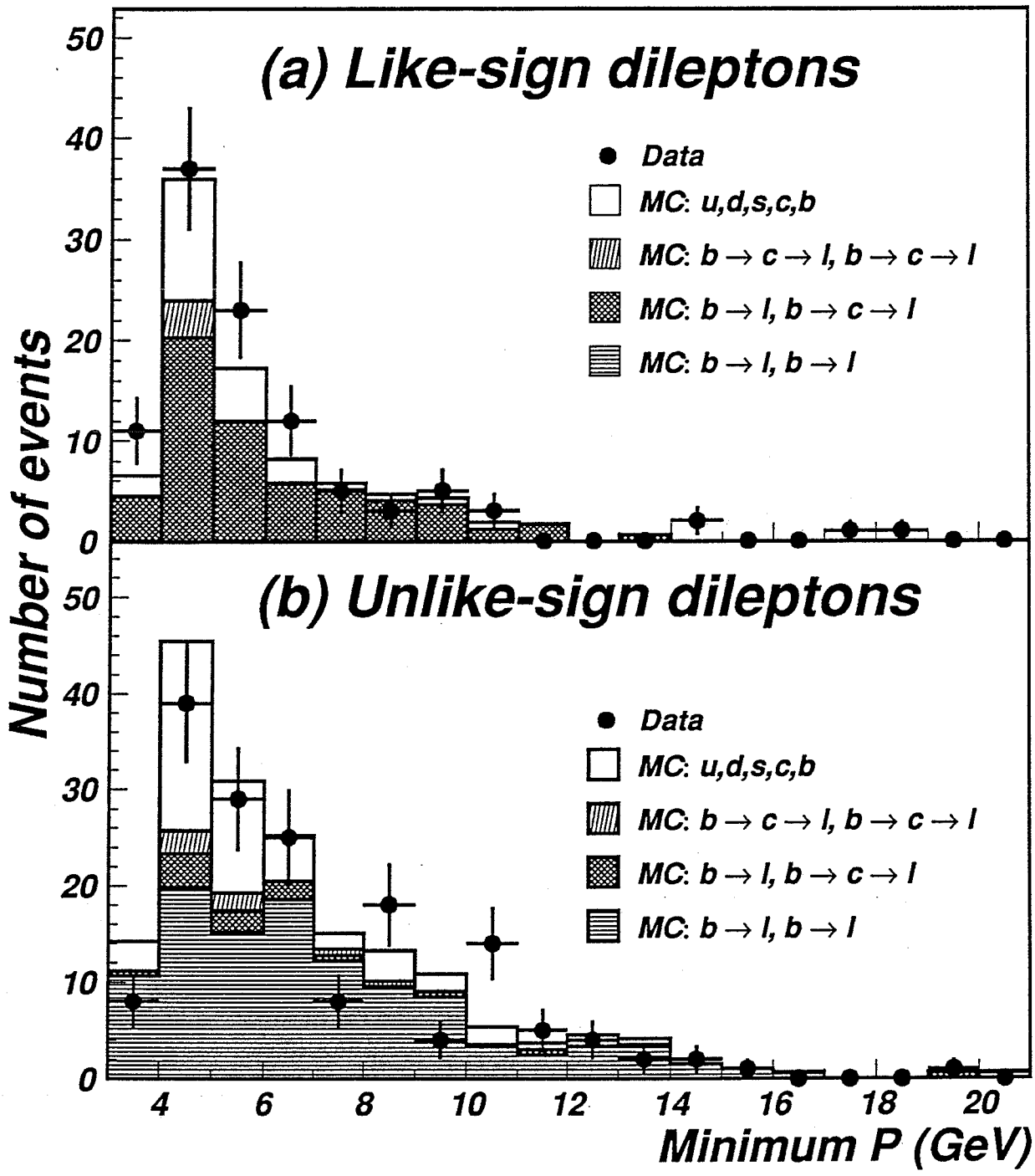

Figure 9-1: The minimum of momenta of the two leptons in the opposite hemisphere, (a) like-sign dileptons; (b) unlike-sign dileptons.

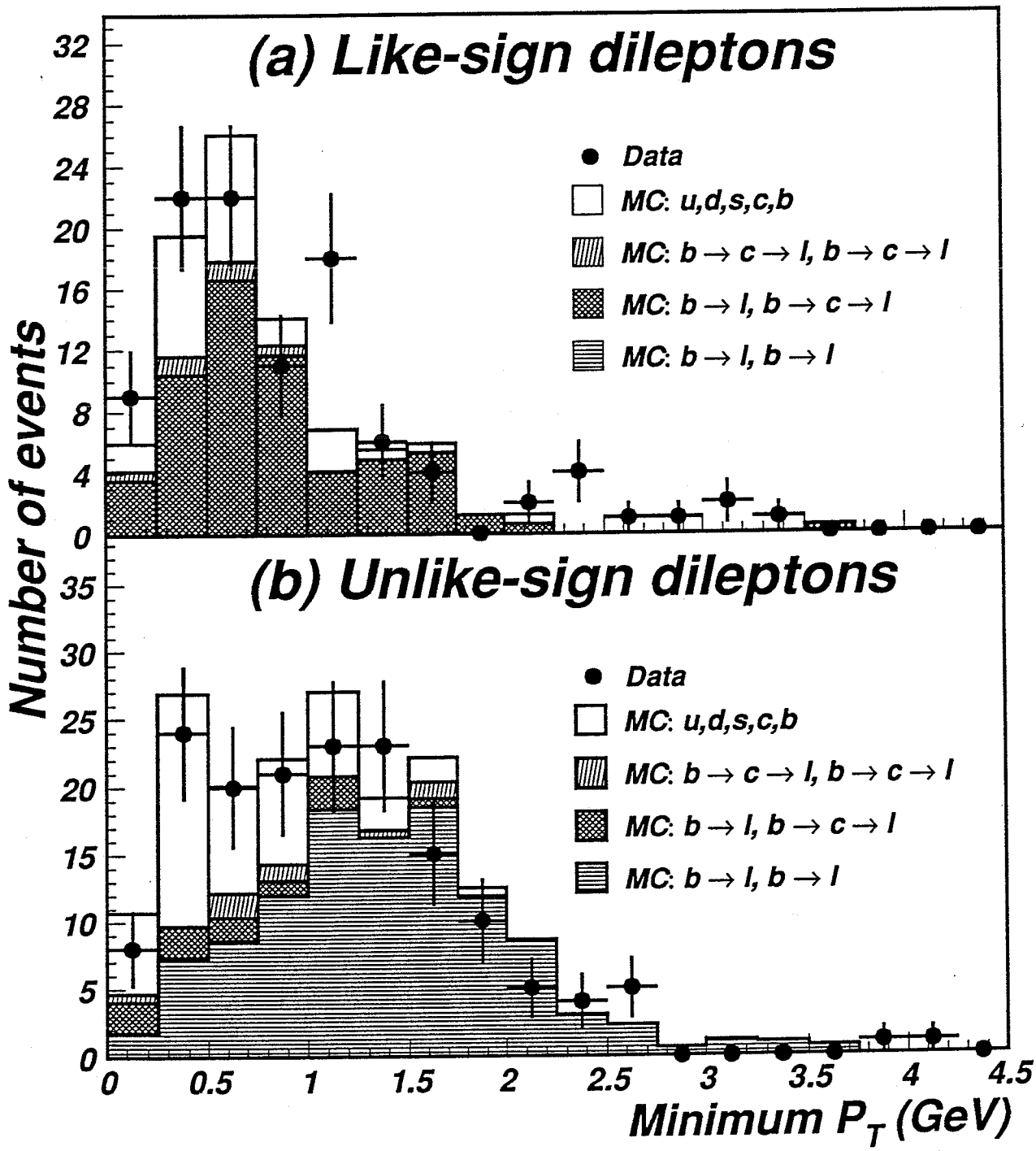

Figure 9-2: The minimum of transverse momentum of the two leptons in the opposite hemisphere, (a) like-sign dileptons; (b) unlike-sign dileptons.

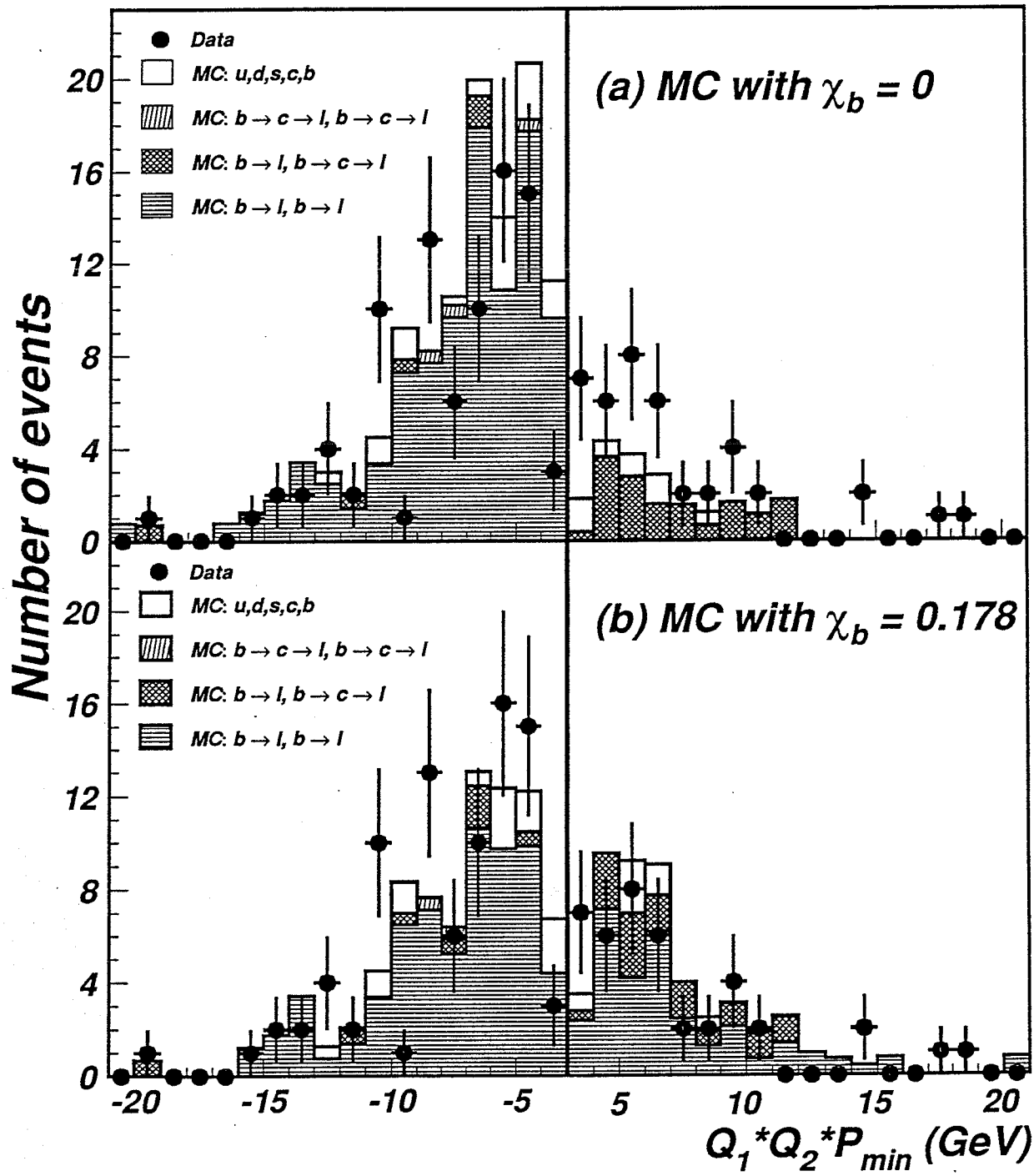

Figure 9-3: The distributions of the minimum momenta of the two leptons in the opposite hemisphere are compared with Monte Carlo predictions (a) with $\chi_B = 0$; (b) with $\chi_B = 0.178$.

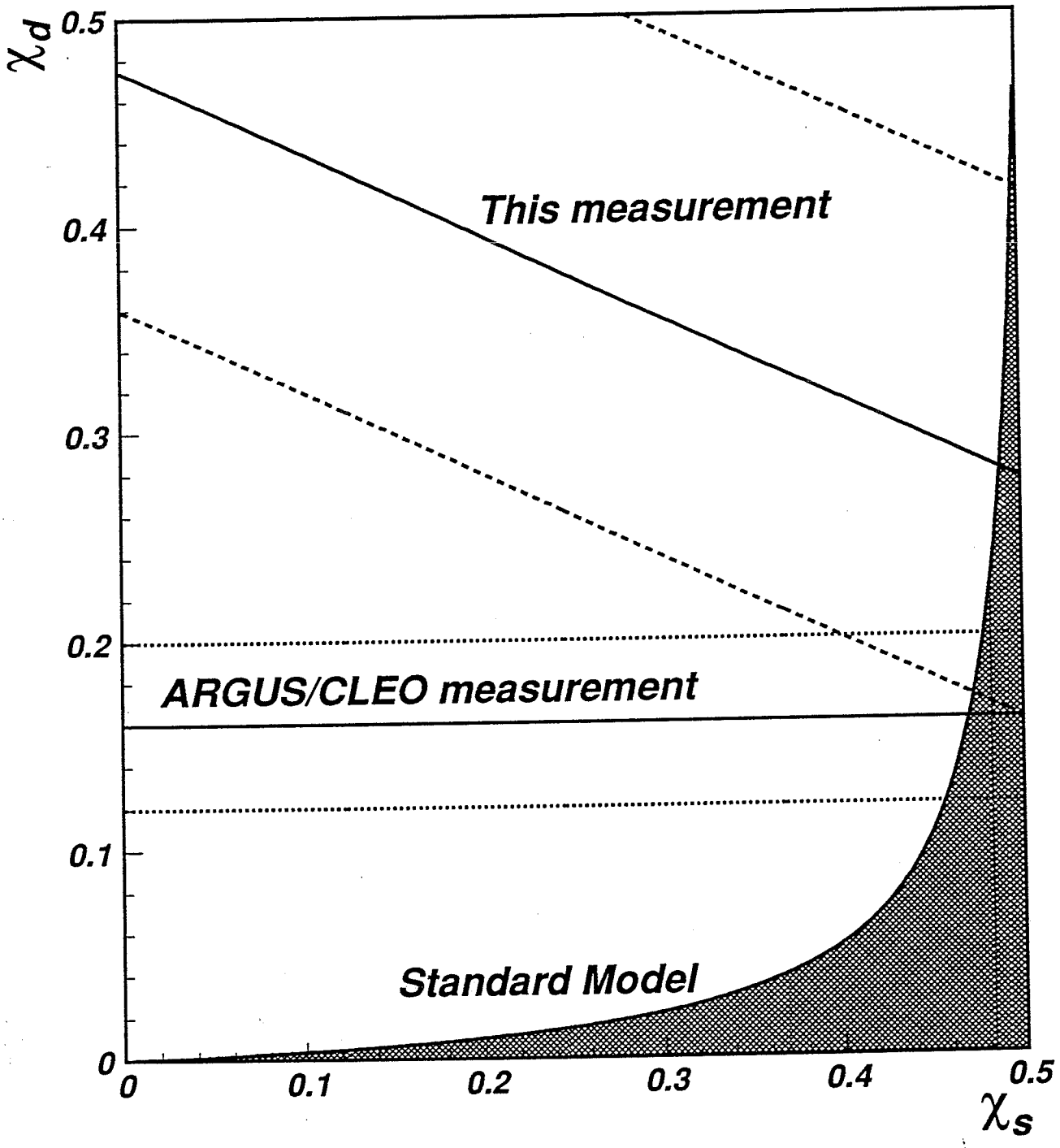

Figure 9-4: The plot of χ_d versus χ_s for the measured χ_B. Also shown are the results from ARGUS/CLEO and the Standard Model allowed region (the hatched region).